

Dissertation

Benchmarking the Particle Background in the LHC Experiments

ausgeführt zum Zwecke der Erlangung des akademischen Grades
Doktorin der technischen Wissenschaften
unter der Leitung von

Ao. Univ. Prof. Dr. Christian W. Fabjan
Institut für Kernphysik der TU Wien

eingereicht an der Technischen Universität Wien
Technisch-Naturwissenschaftliche Fakultät

von

Dipl.-Ing. Edda Gschwendtner

Matrikelnummer e9026965
Heiligenstädterstr. 137/34
A-1190 Wien

Genf, am 17. September 2000

Kurzfassung

Die Experimente für den geplanten Large Hadron Collider (LHC) am CERN müssen für 15 Jahre in Anwesenheit eines sehr hohen Untergrundes an Photonen im Energiebereich von 100 keV bis 10 MeV und an Neutronen im Bereich zwischen thermischen Energien (≈ 0.025 eV) und 20 MeV funktionieren.

Aufgrund der hohen Raten ist dieser Untergrund ein wichtiges Designkriterium für ATLAS, ein Universalexperiment am LHC, der im Jahre 2005 in Betrieb genommen wird.

Bisher wurde der Teilchenuntergrund nur durch umfangreiche Monte Carlo Simulationen mit dem Teilchentransportcode FLUKA abgeschätzt. Für die Ergebnisse dieser Simulationen wird ein Unsicherheitsfaktor von 5 in Betracht gezogen. Ein Beitrag, der auf einen Faktor 2.5 abgeschätzt wird, kommt von den Unsicherheiten in den Schauerprozessen in den Abschirmungsmaterialien sowie von den nachfolgenden Photon- und Neutronenproduktionen, da relevante Messungen in diesem Regime bisher nicht durchgeführt wurden.

Um den Beitrag durch diese Unsicherheiten in den Schauerprozessen zu reduzieren, ist es daher sehr wichtig, durch Messungen die Untergrundvorhersagen zu überprüfen.

Diese Dissertation beschreibt die Messung und die Analyse des Teilchenuntergrundes in einer experimentellen Anordnung, die der Abschirmungssituation in ATLAS sehr ähnlich ist. Sowohl die Energie als auch die absolute Rate der Teilchen, die am Ende des hadronischen Schauerprozesses das Abschirmungsmaterial verlassen, werden mit einem $\text{Bi}_4\text{Ge}_3\text{O}_{12}$ Detektor (BGO) gemessen.

In dieser Studie wurde sehr genau darauf geachtet, überlagernde Effekte, welche die Photonenmessungen verfälschen würden, zu vermeiden. Typischerweise erwartet man ein Photon für jedes 10^4 -te Hadron, das in die Abschirmung einfällt. Das entspricht einem Energieabschwächungsfaktor von $\approx 10^8$.

Zuerst wurden Kalibrationsmessungen mit bekannten radioaktiven Quellen durchgeführt um die Sensitivität des BGO Detektors auf Photonen und Neutronen zu evaluieren.

Die Ergebnisse der Photonenmessungen zeigen ausgezeichnete Übereinstimmung mit den Simulationen, während die Neutronenresultate FLUKA spezifische Diskrepanzen aufweisen, die aber sehr gut abgeschätzt werden können.

Für die Überprüfungen der Untergrundvorhersagen für ATLAS wurde ein umfangreiches Meßprogramm ausgearbeitet. Messungen mit unterschiedlichen Abschirmungsmaterialdicken, verschiedener Strahlenergie und -intensität sowie an verschiedenen Meßposi-

tionen wurden durchgeführt, um systematische Effekt zu reduzieren sowie restliche Untergrundquellen abzuschätzen.

Eine sorgfältige Analyse der Messungen einschließlich einer detaillierten Auswertung der systematischen Fehler ergeben ein genaues Verständnis aller restlichen Untergrundquellen, Totzeitkorrekturen und anderer Rateneffekte.

Der Vergleich der Messungen mit detaillierten FLUKA Simulationen zeigt, daß die Untergrundraten für alle verschiedene Messanordnungen auf 20 % übereinstimmen. Diese Studien geben auch Antwort auf die Natur der Teilchen, die das Abschirmungsmaterial verlassen.

Zusätzlich wurde eine Methode entwickelt, die die gemessenen Photonenraten und -energien aus den simulierten und gemessenen Gesamtergebnissen bestimmt.

Mit diesen Messungen können folglich die Unsicherheiten in den Schauerprozessen in den Abschirmungsmaterialien reduziert werden und somit können die Untergrundberechnungen mit einer höheren Zuverlässigkeit für die ATLAS Untergrundbestimmungen verwendet werden.

Abstract

The experiments for the Large Hadron Collider LHC at CERN have to work for 15 years in the presence of a very high particle background of photons in the energy range from 100 keV to 10 MeV and neutrons in the range from thermal energies (≈ 0.025 eV) to 20 MeV. The background is so high that it becomes a major design criterion for the ATLAS experiment, a general purpose experiment at LHC that will be operational in the year 2005.

The exact level of this background is poorly known. At present an uncertainty factor of five has to be assumed to which the limited knowledge of the shower processes in the absorber material and the ensuing neutron and photon production is estimated to contribute with a factor 2.5.

So far, the background has been assessed only through extensive Monte Carlo evaluation with the particle transport code FLUKA. The lack of relevant measurements, which were not done up to now, are to a large extent responsible for this uncertainty. Hence it is essential to benchmark the background predictions with measurements in order to reduce the uncertainties resulting from the shower processes.

This work describes in detail the benchmarking measurements and analysis of these backgrounds in an experimental arrangement that approaches rather closely the layout and shielding in the ATLAS detector. The absolute yield and energy of the particles emanating from the final stages of the hadronic shower were measured using a $\text{Bi}_4\text{Ge}_3\text{O}_{12}$ detector.

In this study particular care was taken to guard against spurious effects, which could mask the measurements of the photon background. Typically we expect to measure a photon per 10^4 incident hadrons which is equivalent to a reduction factor in energy of $\approx 10^8$.

At first, calibration measurements with well known radioactive sources were carried out in order to evaluate the response to photons and neutrons of the used detector. The photon results show excellent agreement with the simulations, while the neutrons show some FLUKA specific discrepancies that are however well understood.

The actual benchmarking task comprised measurements with different beam intensities and momenta, different positions and absorber thicknesses in order to reduce systematic effects and assess residual activities from other sources.

The careful analysis of the measurements including a detailed evaluation of the systematic uncertainties provides a good understanding of all effects due to residual activities, dead-

time corrections and other rate effects of the set-up.

Comparing the measurements with detailed FLUKA simulations shows that under all different measurement conditions the agreement is on the 20 % level. These studies also give answer to the nature of the particles emanating from the absorber.

Finally a method to obtain the measured photon rates and energies from the total measured and simulated numbers was developed.

The comparison of the measurements with the FLUKA calculations can hence be used to reduce the uncertainties resulting from the shower processes, so that the background simulations can predict the ATLAS background with higher reliability.

Contents

Kurzfassung	iii
Abstract	v
1 The Large Hadron Collider	1
1.1 The Accelerator	1
1.2 Physics at LHC and Detector Requirements	1
1.3 Detectors for the LHC	4
1.4 The ATLAS Detector	5
1.4.1 Detector Subsystems	5
1.4.2 Muon Precision Drift Chambers	9
2 Rate Environment in the ATLAS Muon Spectrometer	11
2.1 Primary Collision Products	11
2.2 Radiation Background	12
2.3 Uncertainties of the Background Evaluation	15
2.4 Impact of the Background on the Muon Spectrometer Performance	17
3 Motivation for Background Benchmarking	20
4 The Experimental Set-Up H6	22
4.1 Introduction	22
4.2 H6 Area	22
4.3 Set-Up	24
4.4 Data Acquisition	26
4.4.1 Readout Chain	26
4.4.2 Timing	27
4.4.3 Trigger Conditions	28
5 Detector Response Calibration	30
5.1 Introduction	30
5.2 Photon Response	30
5.2.1 Experimental Set-Up	30
5.2.2 Measurements and Analysis	32
5.2.3 Results	33
5.2.4 Comparison of Measurements and Simulations	36

5.3	Neutron Response	39
5.3.1	Neutron/Photon Ratio of the Am-Be-Source	39
5.3.2	BGO Response Measurements for Neutrons	40
5.3.3	Comparison of Am-Be Measurements with Simulations	42
5.4	Summary	45
6	Scope of the Benchmarking Measurements in H6	46
6.1	Overview of the Measurements	46
6.2	Auxiliary Measurements	49
6.2.1	BGO Energy Calibration	49
6.2.2	Beam Flux Calibration	51
7	Analysis Procedure of the Measurements	54
7.1	Overview	54
7.2	Signal Rate	55
7.2.1	Emanating Particles	56
7.2.2	Beam Flux	57
7.2.3	Summary	58
7.3	Spectral Distribution	58
8	Discussion of Representative Measurements	60
8.1	Introduction	60
8.2	On Beam-Axis	60
8.2.1	Raw Data	60
8.2.2	Spectra	62
8.3	Off Beam-Axis	64
8.3.1	Raw Data	64
8.3.2	Spectra	65
8.4	Summary	67
9	Results of the Measurements	68
9.1	Summary of the Measured Signal Rates	68
9.1.1	Contributions to the Uncertainty of the Measurements	70
9.2	Summary of the Measured Spectra	73
10	Simulation of the Background Benchmarking	76
10.1	Overview of the Simulation Procedure	76
10.2	Characterisation of the Experimental Set-Up	79
10.3	Results	81
11	Comparison of the Measurements with the Simulations	83
11.1	Introduction	83
11.2	Measured and Simulated Signal Rates	84
11.3	Measured and Simulated Spectra	85
11.3.1	On Beam-Axis	86
11.3.2	Off Beam-Axis	88

11.4 Evaluation of the Measured Photon Rates and Spectra	90
11.4.1 Photon Rates	91
11.4.2 Photon Spectra	92
11.5 Summary	94
12 Relating the H6 Experimental Set-Up to the ATLAS Shielding	95
12.1 ATLAS Photon Background Predicted with the H6 Results	95
12.2 Comparison with ATLAS Calculations	97
Conclusion and Outlook	99
Appendix A	101
A.1 Photon Detection with the BGO	101
A.1.1 Photon Interaction in Matter	101
A.1.2 Predicted Response Function for Photon Detectors	104
A.2 BGO Characteristics	106
A.3 FLUKA	107
Appendix B	109
Glossary	109
Acknowledgements	111
Bibliography	113
Curriculum Vitae	117
List of Publications	118
Lebenslauf	119

Chapter 1

The Large Hadron Collider

1.1 The Accelerator

In 2005, the Large Hadron Collider (LHC) will be operational as a new instrument of discovery in particle physics. The LHC will be a proton-proton collider with a centre-of-mass energy of 14 TeV. It will be installed at the 27 km tunnel at CERN/Geneva that currently houses LEP (Large Electron Positron Collider).

The bunch spacing will be 25 ns. At the interaction points the transverse bunch radius will be $15 \mu\text{m}$ and the bunch length will be 30 cm. This means that the position of the vertex will have a rather large spread along the beam direction, the effective distribution of the vertex position is expected to be 5.5 cm (r.m.s.) along the beam direction.

At a luminosity of $10^{34} \text{ cm}^{-2} \text{ s}^{-1}$ beam crossing points will provide experiments with collision rates at the 10^9 Hz level, producing more than 10^{11} particles per second, i.e. $\approx 10^{18}$ particles per LHC year. Due to the substantial rate of p-p collisions the level of the background is so high that it becomes a major design criterion for the detectors.

Figure 1.1 shows the total proton-proton cross-section together with the production cross-sections for the principal physics channels as a function of the p-p centre-of-mass energy. The total cross-section is estimated to be between 90 and 130 mb. This will result in ≈ 20 p-p interactions per bunch crossing at the nominal luminosity. The total integrated rate is expected to be $\approx 10^{16}$ events/year.

1.2 Physics at LHC and Detector Requirements

The actual mechanism for symmetry breaking in the electroweak sector ($\text{SU}(2) \times \text{U}(1)$) of the Standard Model is associated with the Higgs particle. Hence one of the main goals

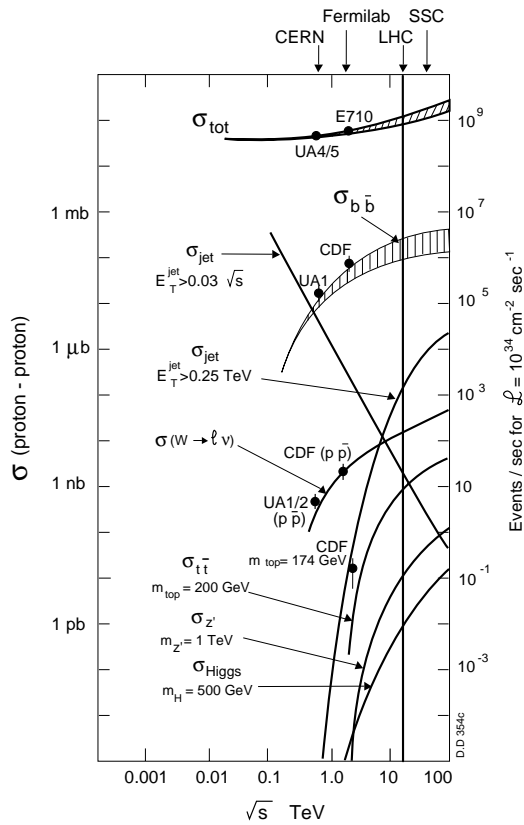


Figure 1.1: The cross-section of some characteristic processes at LHC [Den90].

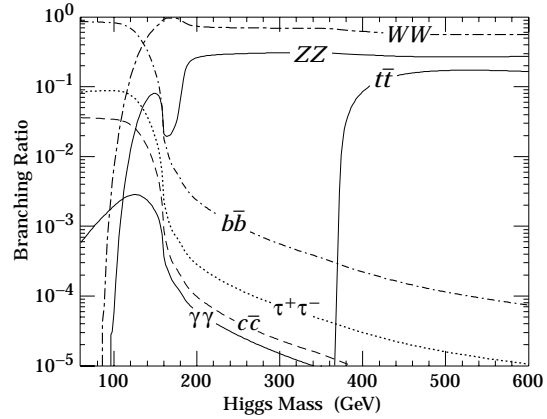


Figure 1.2: Branching ratios of the Higgs.

for the LHC is the search for the Standard Model (SM) Higgs boson [Hig64] or a family of Higgs bosons when considering the Minimal Supersymmetric extension of the Standard model (MSSM).

There is only a limited number of production mechanism which give cross-sections large enough to be relevant for detection at the LHC (see Figure 1.2). Each makes use of the Higgs' preference to couple to heavy particles [Jar90].

Only a few decay channels of the Higgs boson are accessible to experimental observation because either the decay channels have small branching ratios, or the decays are obscured by a large background of events that carry the signature of the Higgs mass. Hence the different Higgs decay channels for the Higgs-mass ranging from 80 GeV/c² to 1 TeV/c² are the most prominent benchmark processes for the detector design at LHC.

The LEP experiments were able to set the Higgs mass limit to 108 GeV/c² in 1999 and will be sensitive up to 114 GeV/c² at the end of the LEP run in December 2000 [Lep00].

- Below the WW or ZZ threshold ($M_H < 2M_Z$) the largest Higgs decay branching ratio

will be $H \rightarrow b\bar{b}$. Since this decay channel is overwhelmed by QCD background, the reconstruction and tagging of b-jets with high efficiency is a crucial element in the detector performance.

The most prominent detection channel is $WH \rightarrow \gamma\gamma$. Nevertheless, this signature suffers from very large backgrounds from continuum QCD $\gamma\gamma$ production and jet-jet and γ -jet production. Hence an electromagnetic calorimeter with excellent photon/jet and photon/electron discrimination is required.

- In the mass region between $120 \text{ GeV}/c^2 < M_H < 180 \text{ GeV}/c^2$ the decay $H \rightarrow ZZ^{(*)} \rightarrow 4l^\pm$ provides a very clean signature for the Higgs boson. For a Higgs mass of $150 \text{ GeV}/c^2$ one expects ≈ 550 such events per year. The background processes are the $ZZ^{(*)}$, $Z\gamma^{(*)} \rightarrow 4l$ continuum, $t\bar{t} \rightarrow 4l$ and $Zb\bar{b} \rightarrow 4l$. The geometrical and kinematic acceptance for leptons is important in this decay channel and the significance of the Higgs signal will depend on the four-lepton mass resolution. Hence good lepton energy/momentum resolution ($\approx 1\%$) is required.
- For the mass range of $180 \text{ GeV}/c^2 < M_H < 800 \text{ GeV}/c^2$ the $H \rightarrow ZZ \rightarrow 4l$ decay mode is considered to be the most reliable discovery channel since the expected signal rates are large and the background small.
- For heavy Higgs boson masses the Higgs width increases rapidly and the signal will be rate limited. In this mass range, the $H \rightarrow ZZ \rightarrow l^+l^-\nu\nu$ can be considered which is six times more frequent than the $H \rightarrow 4l$ channel. It can be detected with the measurements of two high- p_T and a high missing E_T due to the escaping neutrinos.

There are many other examples of LHC physics which have been used as benchmark processes for detector design.

For the search of the MSSM Higgs bosons H^\pm and A , efficient secondary vertex detection for τ leptons and b -quarks as well as high resolution calorimetry for jets and missing transverse energy are essential.

Also the search for stable supersymmetric particles sets stringent requirements for the hermeticity and missing E_T capability of the detectors.

New heavy gauge bosons W' and Z' could be accessible to the LHC for masses up to $5\text{-}6 \text{ TeV}/c^2$. Therefore high resolution lepton measurement and charge identification are needed even in a p_T range up to a few TeV/c .

An important chapter of the LHC physics will be the study of heavy quark systems since also at lower luminosity the LHC will be a high rate beauty and top factory. A particularly rich field will be the precise measurement of CP-violation in the B_d^0 system and the determination of the angles in the Cabibbo-Kobayashi-Maskawa unitary triangle [Eer92]. The investigations of $B\bar{B}$ mixing in the B_s^0 system, rare b decays and general spectroscopy of states with b -quarks will be of great interest. Precise secondary vertex determination, full reconstruction of final states with relatively low- p_T particles and low- p_T lepton first level trigger thresholds as well as second-level track triggering capability are necessary requirements for the experiment.

1.3 Detectors for the LHC

To exploit the full discovery potential of the LHC two general-purpose pp detectors will be installed at the beam crossings (ATLAS and CMS). In addition two specialised experiments (LHC-B and ALICE) will be built.

ATLAS

'A T(oroïdal) L(HC) A(pparatu)S' is characterised by two different magnetic field systems: A super-conducting solenoid will be installed around the Inner Detector cavity and large super-conducting air-core toroids consisting of independent coils will be arranged outside the calorimetry. This concept offers almost no constraints on calorimetry and inner detector allowing non-compromised technological solutions and a high-resolution, large acceptance and robust muon spectrometer with excellent stand-alone capabilities. The next section is dedicated to the description of this experiment.

CMS

The 'C(ompact) M(uon) S(olenoid)' has been optimised for the search of the standard model Higgs boson, but allows detection of a wide range of possible signatures from alternative electro-weak symmetry breaking mechanisms and is well adapted for the study of top, beauty, and tau physics at low luminosities. At the core of the CMS detector sits a large super-conduction solenoid generating a uniform magnetic field of 4 T. The choice of a strong field leads to a compact design for the muon spectrometer without compromising the momentum resolution up to rapidities of $\eta = 2.5$.

LHC-B

This dedicated B-physics experiment at the LHC is an optimised open-geometry forward collider detector which is designed to fully exploit the B-physics potential of the LHC. The large Lorentz boost of accepted B-mesons allows precise decay time measurements, which are complemented by excellent particle identification and efficient muon triggers.

ALICE

'A L(arge) I(on) C(ollider) E(xperiment)' is a general purpose heavy ion experiment designed to measure the flavour content and phase space distribution, event by event, for a large number of particles whose momenta and masses are of the order of the typical energy scale involved ($\Lambda_{\text{QCD}} \approx 200$ MeV). In addition to addressing particular signals which look most promising today, ALICE will search for qualitative and quantitative differences between proton-proton and nucleus-nucleus collisions. An open geometry will facilitate future modifications and upgrades, if first physics results suggest focusing on specific signals, selective triggers or large acceptance.

The detailed descriptions of the experimental set-up of these detectors and their design considerations can be found in the respective detector technical proposals [Atl94],[Cms94],[Lhc98], [Ali95].

1.4 The ATLAS Detector

The ATLAS Collaboration proposes to build a general-purpose p-p detector which is designed to exploit the full discovery potential of the LHC. The detector concept and its physics potential have been presented in the Technical Proposal [Atl94] in 1994. Between 1996 and 1999 various Technical Design Reports (TDR) ([Atb97] - [Att96]) have been issued where a detailed description of the detector systems and their performance is presented. The ATLAS experiment has now entered the construction phase for many of its detector components, with a strict schedule to meet the first collisions at LHC in summer 2005.

The observable cross-sections for most of the processes are small over a large part of mass range, hence it is an important design consideration to operate at high luminosity and to maximise the detectable rates above backgrounds by high-resolution measurements.

The basic design criteria of the detector include the following:

- Very good electromagnetic calorimetry for electron and photon identification and measurements, complemented by full-coverage hadronic calorimetry for accurate jet and missing transverse energy (E_T^{miss}) measurements.
- High-precision muon momentum measurements, with the capability to guarantee accurate measurements at the highest luminosity using the external muon spectrometer alone.
- Efficient tracking at high luminosity for high- p_T lepton-momentum measurements, electron and photon identification, τ -lepton and heavy-flavour identification, and full event reconstruction capability at lower luminosity.
- Large acceptance in pseudorapidity (η) with almost full azimuthal angle (ϕ) coverage everywhere. The azimuthal angle is measured around the beam-axis, whereas pseudorapidity relates to the polar angle (θ) with $\eta = -\ln(\tan \theta)$ where θ is the angle from the z -direction (along the beam line).
- Triggering and measurements of particles at low- p_T thresholds, providing high efficiencies for most physics processes of interest at LHC.

1.4.1 Detector Subsystems

Magnet System

The magnet configuration is based on an inner thin super-conducting solenoid surrounding the inner detector cavity with a radius of 1.2 m and a length of 5.3 m. It provides an axial magnetic field of 2 T in the centre of the tracking volume.

Three super-conducting air-core toroids consisting of independent coils arranged with an eight-fold symmetry outside the calorimeters will provide an average toroidal field of 0.5 T

in the muon system. The muon spectrometer defines the overall dimensions of the ATLAS detector (see Figure 1.3). The barrel toroid extends over a length of 26 m with an inner diameter of 9.4 m and an outer diameter of 19.5 m. Two end-cap toroids with a length of 5.6 m and an inner diameter of 1.26 m are inserted in the barrel at each end. The toroidal magnet configuration provides a field that is mostly orthogonal to the muon trajectories in the muon spectrometer, while minimising the degradation of resolution due to multiple scattering.

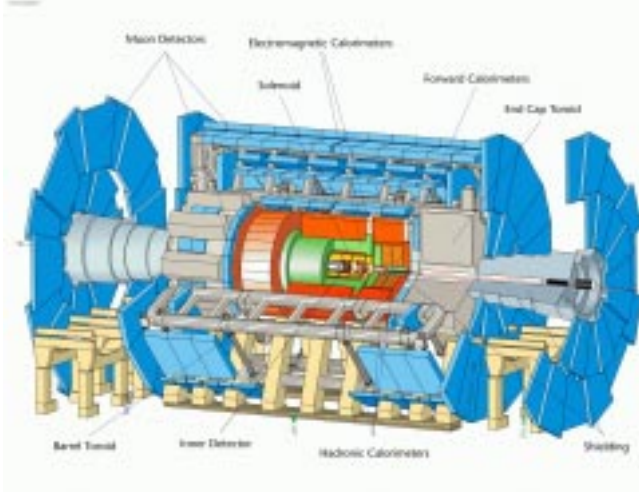


Figure 1.3: 3D view of the ATLAS detector.

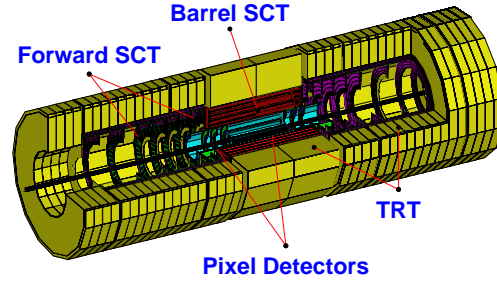


Figure 1.4: ATLAS Inner Detector consisting of a pixel detector system, a Semi Conductor Tracker (SCT) and a Transition Radiation Tracker (TRT).

Inner Detector

Figure 1.4 shows the layout. The Inner Detector is contained in the solenoid within a cylinder of 7 m length and a radius of 1.15 m. Pattern recognition, electron identification, momentum and vertex measurements are achieved with a combination of discrete high-resolution semiconductor pixel and strip detectors in the inner part of the tracking volume, and continuous straw-tube tracking detectors with transition radiation capability in its outer part.

The pixel detector consists of three barrel layers of 140 million pixels where each has a resolution of $50 \mu\text{m}$ in $R-\phi$ and $300 \mu\text{m}$ in the z -direction (along the beam line). Four disks are mounted on each side between radii of 11 cm and 14 cm aiming for a point resolution of $\sigma_{r-\phi} = 12 \mu\text{m}$ and $\sigma_z = 60 \mu\text{m}$. The readout chips must withstand over 300 kGy of ionising radiation and over $5 \cdot 10^{14}$ neutrons per cm^2 in ten years of operation.

The Semi Conductor Tracker (SCT) is based on silicon strip detectors with a pitch of $80 \mu\text{m}$ mounted in four barrel layers at radii of 30, 37.3, 44.7 and 52 cm using small

angle stereo to obtain the z measurements. The forward modules are mounted in up to three rings onto nine wheels. The detector contains 61 m^2 of silicon detectors, with 6.2 million readout channels. The spatial resolution is $16\ \mu\text{m}$ in $R\phi$ and $580\ \mu\text{m}$ in z . The Transition Radiation Tracker (TRT) consists of 420000 proportional drift tubes (4 mm diameter) divided into a barrel part and several forward parts. Each channel provides a drift-time measurement, giving a spatial resolution of $170\ \mu\text{m}$ per straw and two independent thresholds. The detector is operated with a $\text{Xe}/\text{CF}_4/\text{CO}_2$ gas mixture optimised for the detection of X-rays created as transition radiation in stacks of thin radiators between the tubes.

Calorimetry

The ATLAS calorimetry system is shown in Figure 1.5. A barrel cryostat around the Inner Detector cavity contains the electromagnetic (EM) Liquid Argon (LAr) calorimeter and the solenoidal coil. Two end-cap cryostats enclose the electromagnetic and hadronic end-cap calorimeters as well as the integrated forward calorimeter.

The EM calorimeter consists of accordion shaped Kapton electrodes and lead absorbers over its full coverage with a segmentation of $\Delta\eta \times \Delta\phi \approx 0.025 \times 0.025$ aiming for an energy resolution of $\Delta E/E = 10\%/\sqrt{E} \oplus 1\%$ (E in GeV). The total thickness of the EM calorimeter is above $24\ \mathcal{X}_0$ in the barrel region and above $26\ \mathcal{X}_0$ in the end-caps [Atl96] and covers the pseudorapidity range $|\eta| < 3.2$.

The barrel hadronic calorimeter with an inner (outer) radius of 2.28 m (4.25 m) and a half-length of 6.10 m is based on a sampling technique using iron as absorber material and scintillating tiles as active material (TILE Calorimeter). The resulting segmentation of the hadronic calorimeter is $\Delta\eta \times \Delta\phi \approx 0.1 \times 0.1$. The total thickness of the tile-instrumented region is 9.2 interaction lengths λ at $|\eta| = 0$. In the range of $1.5 < |\eta| < 3.2$ the end-cap hadronic calorimeter consists of a copper-LAr detector with parallel plate geometry. The high density forward calorimeter covers the region $3.2 < |\eta| < 4.9$ with a front face at about 4.7 m from the interaction point which results in high level of radiation. It is based on rods filled with LAr in a copper and tungsten matrix. The expected energy resolution for the hadronic calorimeter is $\Delta E/E = 50\%/\sqrt{E} \oplus 3\%$ for $|\eta| < 3$ and $\Delta E/E = 100\%/\sqrt{E} \oplus 10\%$ for $3 < |\eta| < 4.9$ (E in GeV).

Muon Spectrometer

The muon spectrometer (see Figure 1.6) must identify and reconstruct muon tracks, measure their momenta, and provide matching information for association with inner-detector data. It also has to trigger on single- or multi-muon event topologies and associate unambiguously the muon with its parent bunch crossing [Atm97a].

Achieving a resolution $\Delta p_T/p_T \approx 10\%$ for $p_T = 1\ \text{TeV}/c$ dictates the combination of the bending power of the the large super-conducting air-core toroid magnets and of the precision with which the muon instrumentation can measure the sagitta of the particles. A

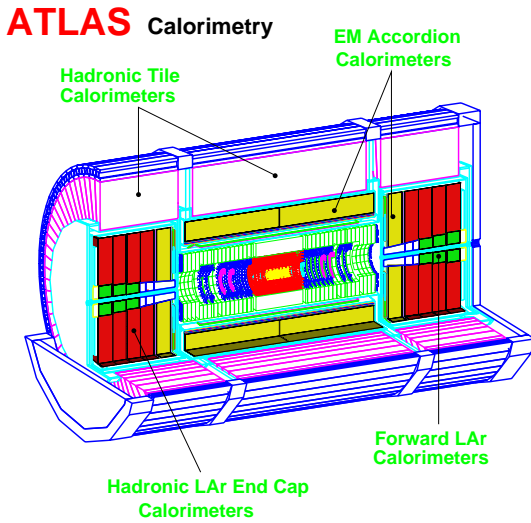


Figure 1.5: *Layout of the ATLAS calorimetry system.*

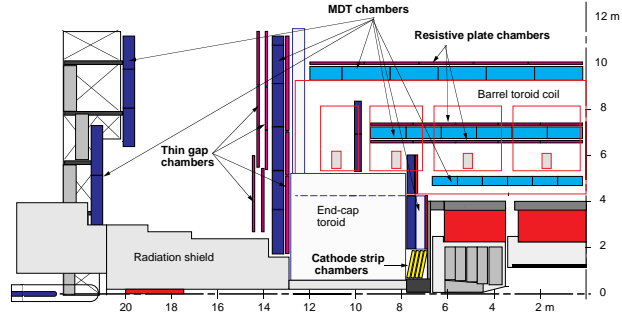


Figure 1.6: *Side view of one quadrant of the ATLAS experiment.*

muon with $p_T = 1 \text{ TeV}/c$ shows a sagitta of $\approx 500 \mu\text{m}$ in an average magnetic field of 0.5 T . Thus a momentum resolution of 10% requires a sagitta-measurement accuracy of $50 \mu\text{m}$. The precision chambers will be Monitored Drift Tube chambers (MDTs) over most of the rapidity range. In the region where the radiation level is highest ($2 < |\eta| < 2.7$) Cathode Strip Chambers (CSCs) are employed. In the barrel region, tracks are measured in the MDTs arranged in three cylindrical layers around the beam-axis at radii $5, 7.5$ and 10 m . The end-cap chambers are arranged in four disks at distances of $7, 10, 14$ and $21\text{--}23 \text{ m}$ from the interaction point and cover the range of $1 < |\eta| < 2.7$. Optical alignment systems have been designed to meet the stringent requirements on the mechanical accuracy and the survey of the precision chambers.

Resistive Plate Chambers (RPCs) are used for bunch crossing identification, measurement of the 'second coordinate' (coordinate along the magnetic field lines) and for triggering the experiment. The RPCs are gas-filled parallel plate chambers with a typical space-time resolution of $1 \text{ cm} \times 1 \text{ ns}$. Four layers of RPCs with two coordinate readout are located near the middle muon station arranged in two groups of two chambers separated by about 40 cm . Three additional chamber layers are located in the outer muon station. Low and high p_T muon triggers are realised by requiring coincidences between groups of chambers in defined roads.

The forward region will use Thin Gap Chambers (TGCs) for triggering and second coordinate measurements.

Trigger Scheme

The ATLAS trigger is organised in three levels (LVL1, LVL2, LVL3). The LVL1 trigger uses reduced-granularity data from a subset of detector and accepts data at the full bunch crossing rate of 40 MHz . LVL1 must select not more than one interaction in 10^4 to reach a

trigger rate below 100 kHz. The LVL2 and LVL3 trigger reduce the event rate to 10-100 Hz. The LVL2 trigger uses full-granularity, full-precision data from most of the detectors, but examines only regions of the detector flagged at LVL1 as containing interesting information. The LVL3 trigger uses the full event data for the final selection of events for off-line analysis.

1.4.2 Muon Precision Drift Chambers

The basic elements of muon precision drift chambers are Aluminium drift tubes (MDTs) with an outer diameter of 3 cm (wall thickness of $400\ \mu\text{m}$) and a $50\ \mu\text{m}$ central wire (W/Re 97/3, gold-plated 3% by weight) that is connected to positive high voltage.

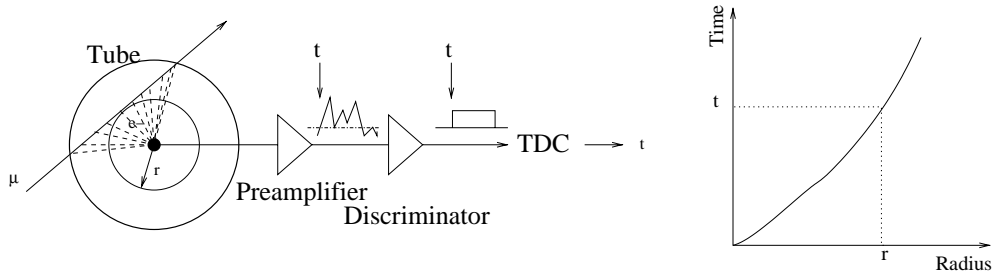


Figure 1.7: Principle of the MDT operation. The electron drift time is measured and converted to distance via a space-drift time relation (rt -relation).

The principle of operation is shown in Figure 1.7. A muon crossing the MDT ionises the detector gas along its track, the electrons are drifting towards the wire in the electric field and are multiplied in an avalanche process close to the wire due to the high field. The movement of the electrons and ions induces a current on the wire that is read out at one end of the tube by a current sensitive pre-amplifier. After discriminating the signal, a Time to Digital Converter (TDC) stores the arrival time of the pulse, such measuring the drift time of the ionisation electrons. The drift time is then converted to a distance using the space-time relationship, which is often referred to as ‘ rt -relation’ and which is obtained by a so-called auto-calibration procedure [Vie96]. The detailed analysis of the contributions to the spatial resolution that can be obtained with such a drift tube is discussed in [Rie97]. To guarantee good performance of the MDT in a high-rate environment the level of the background has to be understood very well. The evaluation of the background environment is subject of this thesis.

The MDT chamber consists of two multilayers separated by a support structure. Each multilayer combines three¹ or four² layers of tubes (see Figure 1.8). The support structures provide accurate positioning of the two multilayers with respect to each other and

¹In the middle and outer station.

²In the inner station.

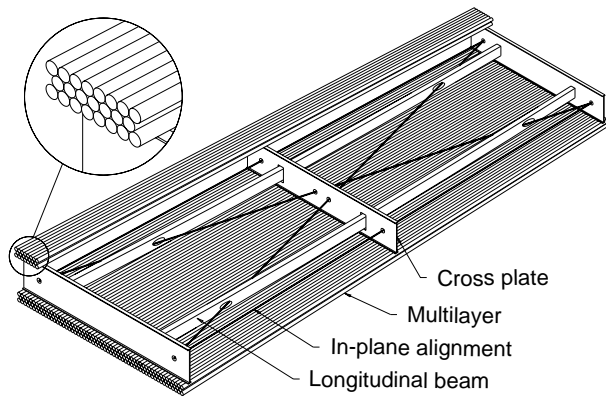


Figure 1.8: *Two multilayers of MDT tubes each consisting of three or four layers are glued to a support frame ('spacer structure') to form a chamber.*

mechanical integrity under effect of gravity and temperature.

The MDT in-plane alignment system will monitor the wire displacement in the experiment with an accuracy of $10\ \mu\text{m}$ or better (see Figure 1.8).

The wires of the chamber must be placed with respect to alignment fiducials with an accuracy of $20\ \mu\text{m}$. An X-ray Tomograph is used to check the wire-position accuracy before the chambers are installed [Gsc97, Gsc98].

The relative position of the muon chambers in the inner, middle and outer station will be monitored by an optical alignment system with an accuracy of $<30\ \mu\text{m}$.

The 1194 MDT chambers will cover an area of $5500\ \text{m}^2$. The total number of readout channels is 370000.

Chapter 2

Rate Environment in the ATLAS Muon Spectrometer

While the particles in the Inner Detector come mainly from the primary proton interaction, the particle flux in the muon spectrometer results from a chain of complex interactions in the calorimetry and shielding and is therefore affected by much larger uncertainties.

The high level of particle fluxes in the muon spectrometer has a major impact on the design considerations of the whole system but also on the optimisation of the single tube response. The background sources can be classified into two categories [Atm97a]: The primary collision products and the radiation background.

2.1 Primary Collision Products

- **Prompt muons and meson decays in flight**

Sources of this background are semileptonic decays of heavy ($c, b, t \rightarrow \mu X$) flavours and gauge Boson decays ($W, Z, \gamma^{(*)} \rightarrow \mu X$). At moderate $p_t > 10 \text{ GeV}/c$, the cross-section is dominated by charm and beauty decays. At larger $p_t > 10 \text{ GeV}/c$, top and Z decays also give a sizeable contribution.

- **Hadronic debris**

Light hadrons emerging from p-p collisions contribute to the charged-particle background through three mechanisms:

First, there are decays in flight ($h \rightarrow \mu X$) in the inner tracker cavity. Second, hadronic debris produced in calorimeter showers can decay into muons which may reach the muon chambers ('shower muons'). Third, one finds the 'hadron punch-through' where a small fraction of the hadrons interact late or not at all in the calorimeters and penetrate into the muon spectrometer.

The hadron decays in flight were calculated using the DTUJET package for the description of the primary p-p collision. The subsequent interactions of other particles in the tracker and the calorimeters were modelled using FLUKA [Fas97]. Detailed account was taken of the current ATLAS layout [Ati97, Atl96, Att96] and of the corresponding absorptive thickness (see Figure 2.3). The transverse momentum dependence of the inclusive muon

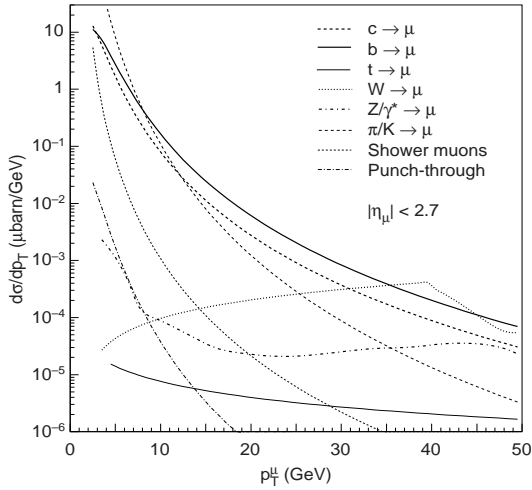


Figure 2.1: *Transverse momentum dependence of inclusive muon cross-sections.*

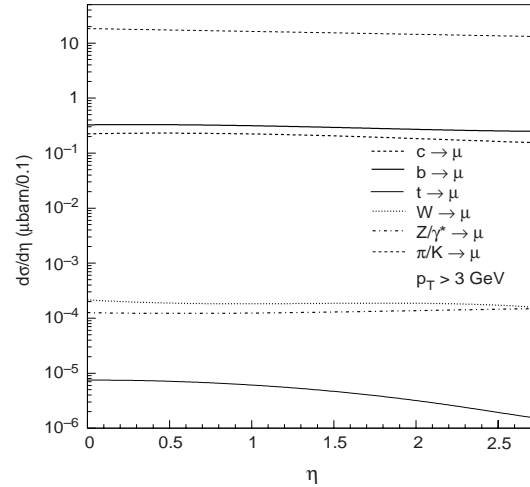


Figure 2.2: *Rapidity-dependence of the inclusive muon cross-sections, integrated over $3 < p_t < 50$ GeV/c.*

cross-section is displayed in Figure 2.1. Comparison of the prompt-muon and hadronic components confirms that the calorimeter system has enough absorptive power to suppress hadronic debris well below the irreducible level of prompt and decay muons. The total counting rate from primary collision products is dominated by low- p_t pion and kaon decays in the inner tracker cavity (see Figure 2.2). At nominal luminosity, this rate is estimated for the innermost layer of precision chambers to a few Hz/cm² at $\eta \approx 0$, and several ten Hz/cm² at $\eta \approx 2$, albeit with substantial uncertainties.

For the MDT performance this background is however negligible compared to the neutron and photon background.

2.2 Radiation Background

The most important backgrounds are low-energy neutrons, photons, electrons, muons and hadrons originating from primary hadrons interacting with the forward calorimeter, shielding material, the beam pipe and other machine elements. If the material is thick enough, the shower development will continue until most of the charged particles have been absorbed. The remnants are mostly neutrons and associated photons.

Electromagnetic showers are absorbed very rapidly, while neutrons will travel long distances losing their energy gradually. Nuclear capture, in particular of thermal neutrons,

frequently results in the production of photons via (n,γ) reactions. Photons also result from excited-state decay via evaporation from spallation products. The typical γ energies from these processes range from 100 keV up to several MeV. Photons produced deep inside the material are quickly absorbed. Those observed in the muon detectors are usually produced in the outermost centimetres of the material.

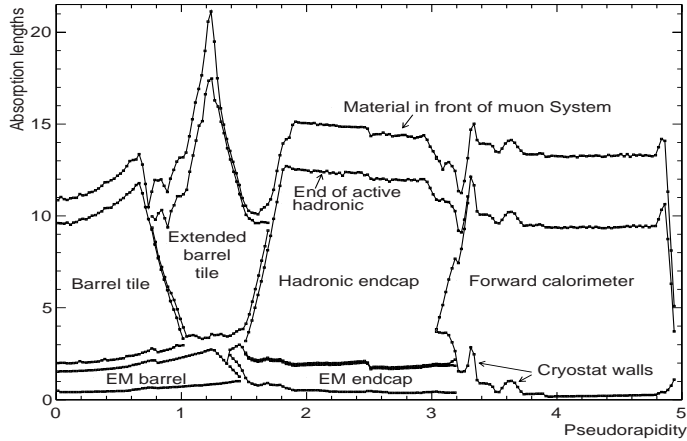


Figure 2.3: Contribution of the various ATLAS detectors to the absorptive thickness, shielding the muon system from primary collision products.

These particles enter the muon spectrometer from all directions. They form a background with essentially no time structure and can not be any longer correlated to the primary p-p interaction.

Neutron and photon fluences have been computed [Bat94a, Fer95, Fer97] taking into account the material distribution (see Figure 2.3) as well as the magnetic field in the ATLAS detector and in the experimental hall. The expected photon and neutron fluxes in the different regions of the muon spectrometer are shown in Figures 2.4 and 2.5.

Interaction of Photons and Neutrons with the Muon Detectors

Using the MDTs as an example, typical detection efficiencies for photons are at the level of 1%, and those for neutrons about one order of magnitude smaller. Notwithstanding these low sensitivities, the low-energy neutral particle background will dominate the counting rates in most areas of the spectrometer.

Thermal neutrons create signals in gas-filled detectors via (n,γ) reactions with a subsequent interaction of the photons. Neutrons with energies between several eV and several tens of keV have a very low detection efficiency because the capture cross-section is small and elastic scattering results in energy losses below the detection threshold. At higher energies, neutrons give signals mostly through elastic scattering, producing either a recoil proton or a heavier recoil nucleus. The sensitivity to neutrons is more uncertain in the energy range

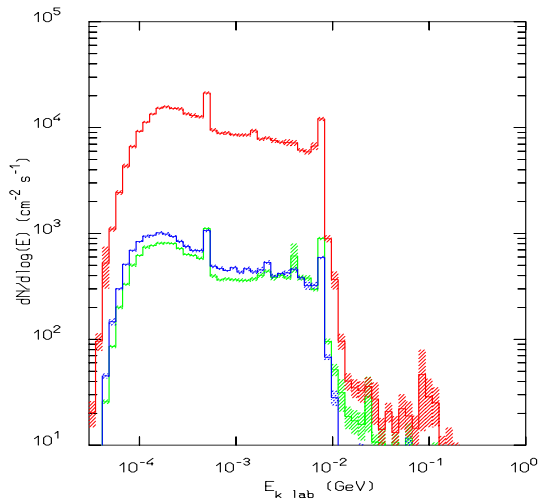


Figure 2.4: The expected photon flux as a function of photon energy in different regions of the muon spectrometer (top curve: $2.3 < |\eta| < 2.7$, middle curve: $1.4 < |\eta| < 2.3$ and bottom curve: $|\eta| < 1.3$).

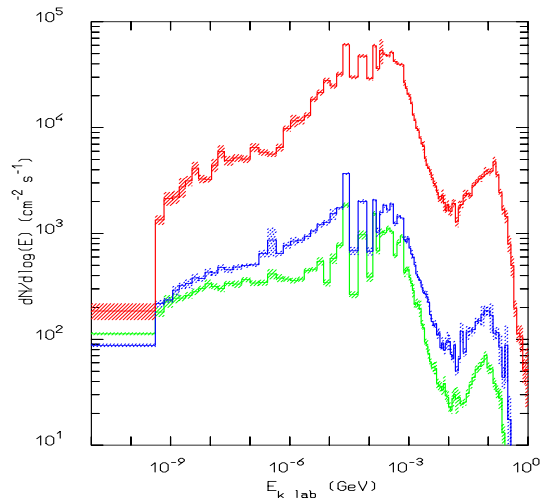


Figure 2.5: Expected neutron flux in different rapidity regions (top curve: $2.3 < |\eta| < 2.7$, middle curve: $1.4 < |\eta| < 2.3$ and bottom curve: $|\eta| < 1.3$).

from several keV up to 1 MeV owing to the uncertainty in the threshold behaviour of the detectors.

Photons cause signals through photo-effect, pair-production or Compton scattering. Photons with energies above a few MeV can produce electrons of sufficient energies to give correlated signals in neighbouring detector elements.

To obtain actual detection efficiencies, two approaches were used [Che93, Bar94, Bat94b, Den94]. Small prototypes of the various chamber types were exposed to neutron and photon sources, and the detection efficiency measured at several known particle energies. These measurements were supplemented with Monte Carlo simulations, reproducing the detailed chamber structures and the calculated neutron and photon energy spectra. The agreement between calculated and measured efficiencies is in general better than 30%. Table 2.1 shows the typical efficiencies for the various chamber types, integrated over the relevant energy region.

Table 2.1: Average sensitivity of muon chambers to neutron and photon background in the ATLAS hall [Atm97a].

chamber type	neutron sensitivity	photon sensitivity
MDT	$\approx 10^{-3}$	$\approx 8 \times 10^{-3}$
CSC	$\approx 10^{-4}$	$\approx 5 \times 10^{-3}$
RPC, TGC	$\approx 10^{-4}$	$\approx 5 \times 10^{-3}$

Combining the different contributions of the processes discussed in sections 2.1 and 2.2

yields the rapidity-dependence of the expected counting rate in the various MDT chambers.

Figure 2.6 shows the counting rate for the innermost MDT station at nominal luminosity. We see that at rapidity $|\eta|=2$ ($\theta = 15^\circ$) the interacting photon background rate is about 100 Hz/cm^2 , whereas the muon rate is about 10^{-3} Hz/cm^2 . In Figure 2.7 we find the total counting rate in the three precision chamber stations. The calculated fluences in the entire ATLAS hall are shown in Figures 2.8 and 2.9.

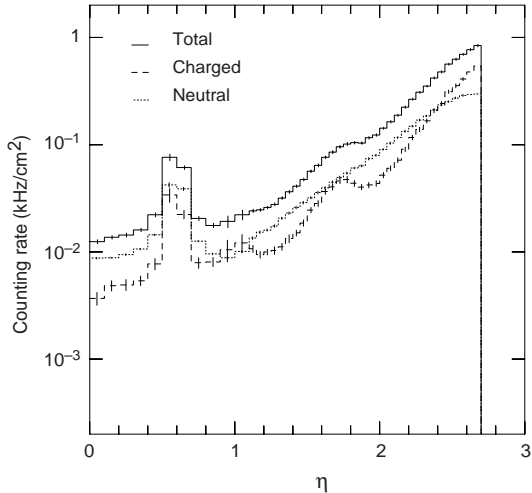


Figure 2.6: Pseudorapidity dependence of the counting rate in the innermost MDT station at nominal luminosity.

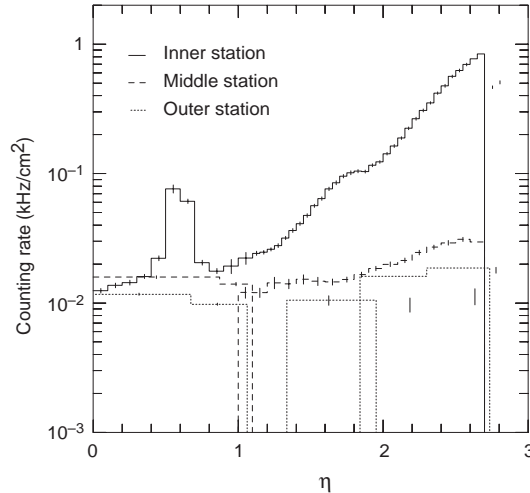


Figure 2.7: Pseudorapidity dependence of the total counting rate in the three precision-chamber stations.

2.3 Uncertainties of the Background Evaluation

The following components contribute to the uncertainties of the above background rates:

- **p-p cross-section**

The combination of the uncertainties attached to the total p-p cross-section and to the multiplicity produced in the primary collisions, is estimated at $\pm 30\%$.

- **Chamber sensitivities**

The comparison of simulation results and laboratory measurements on chamber sensitivities conservatively suggests the numbers assumed could be in error by a factor of up to 1.5.

- **Showering processes in the absorber**

Limited knowledge of the showering processes in the absorber, and of the (n, γ) cross-sections is estimated to modify the fluences by a factor of up to 2.5.

A conservative superposition of these uncertainties yields a factor of five. The ATLAS muon instrumentation is therefore designed to operate at a nominal luminosity of $10^{34} \text{ cm}^{-2}\text{s}^{-1}$, allowing for an uncertainty factor of five on the background rate.

With the tube diameter of 3 cm and the uncertainty factor of five one consequently gets a photon background rate of 1500 Hz per cm wire at e.g. $|\eta| = 2$ (see Figure 2.6). Since the length of the tubes at the 'hottest' spot is ≈ 2 m background rates of 300 kHz per tube have to be expected.

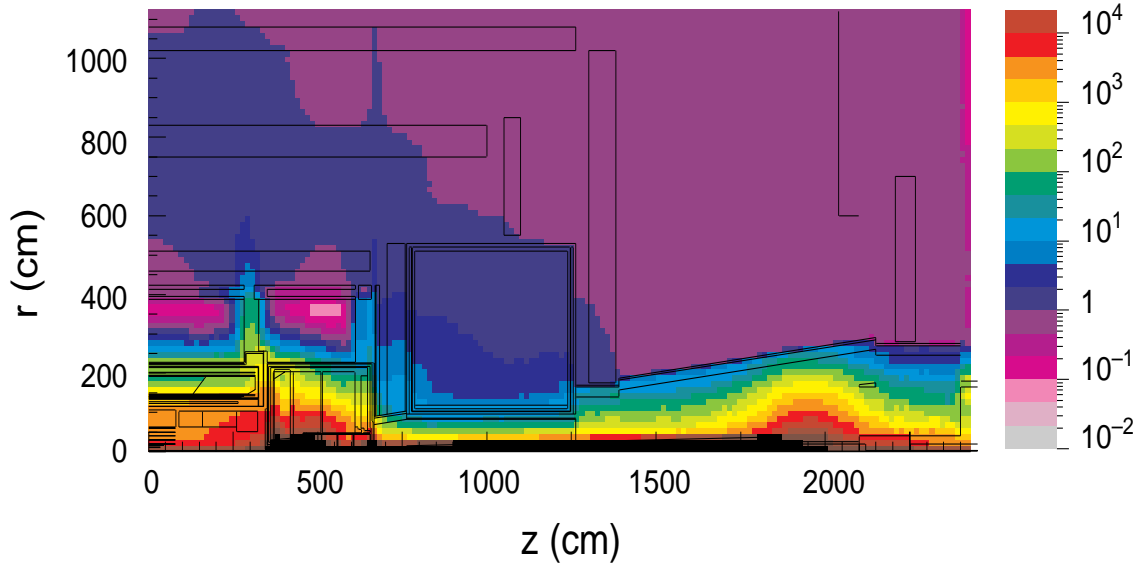


Figure 2.8: Photon fluence in the ATLAS hall (kHz/cm^2) at nominal luminosity.

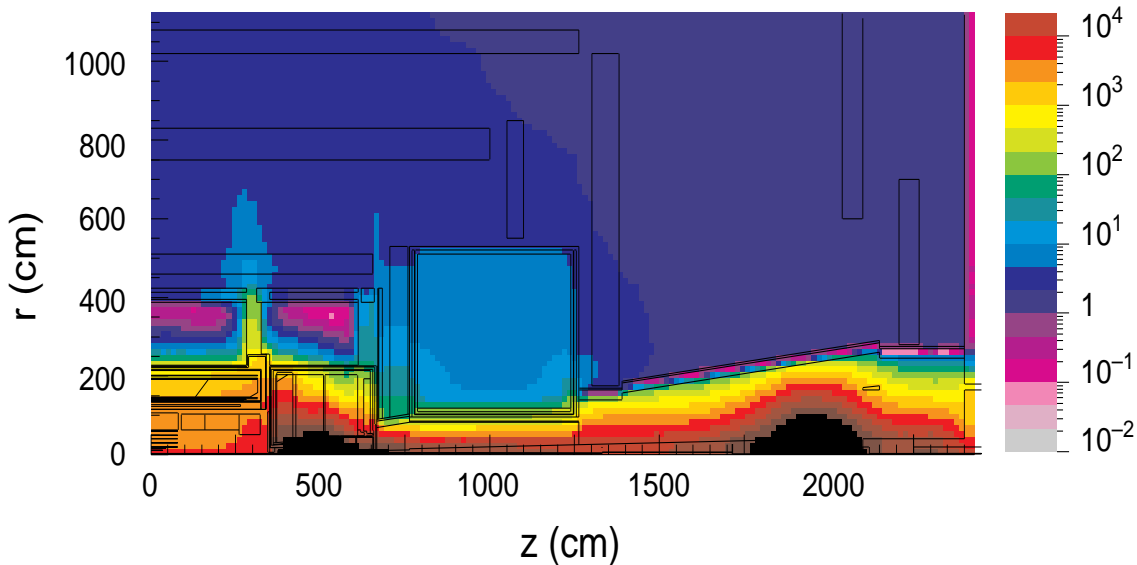


Figure 2.9: Neutron fluence in the ATLAS hall (kHz/cm^2) at nominal luminosity.

2.4 Impact of the Background on the Muon Spectrometer Performance

The main performance numbers of the muon spectrometer are pattern recognition efficiency and momentum resolution in the given background environment. The requirements on the performance will then define the specifications for the precision chambers.

Momentum Resolution

The goal is a momentum resolution of about 10 % for the most energetic muons that are expected at LHC (i.e. about 1 TeV muons). Figure 2.10 shows the individual contributions to the momentum resolution in the barrel region of the spectrometer. We see that for low energy muons the momentum resolution is limited by multiple scattering of the muons in the spectrometer material. For high energy muons the momentum resolution is limited by alignment errors and the MDT resolution which was assumed to be $80 \mu\text{m}$ for this simulation.

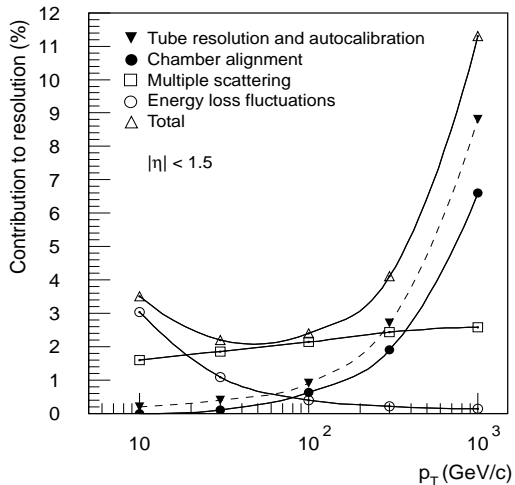


Figure 2.10: Individual contributions to the momentum resolution as a function of p_T . The average single wire resolution is assumed to be $80 \mu\text{m}$.

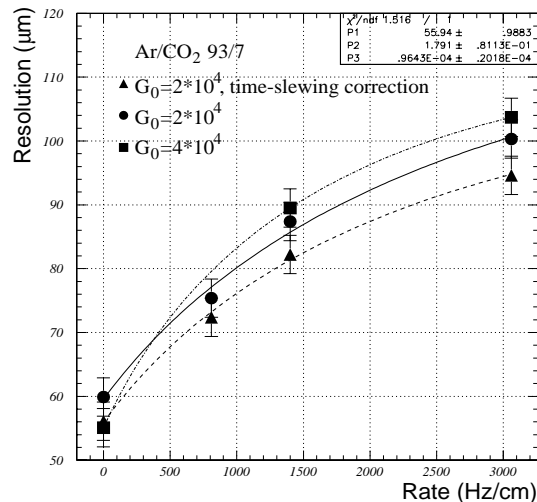


Figure 2.11: Resolution of Ar/CO₂/93/7 as a function of the rate [Ale99].

At high background rates the MDT resolution is degraded significantly by space-charge effects. For the tube geometry and working point the ions created in the avalanche at the wire take about $t_{max}^{ion} \approx 4 \text{ ms}$ to drift to the tube wall (cathode). The presence of ions in the drift region creates a space charge which modifies the electric field for subsequent events. As the electric field changes, the electron drift velocity changes, the rt -relation is shifted and therefore the single wire resolution is deteriorated. This effect puts severe requirements

on the choice of the drift gas and the gas gain. In order to minimise this additional bias in resolution one would prefer to use a gas for which the electron drift velocity depends only weakly on the electric field.

Figure 2.11 shows the MDT resolution as a function of rate for Ar/CO₂/93/7. Without background rate the average resolution is $\approx 50 \mu\text{m}$ (with time slewing correction¹). For the highest expected background rates (1500 Hz/cm including an uncertainty factor of five) the $80 \mu\text{m}$ resolution limit is already reached.

Reconstruction Efficiency

Another important performance criterion of the muon chambers is the pattern recognition efficiency, i.e. the efficiency to reconstruct muon tracks correctly. The high background levels resulting in large chamber occupancies (up to 20% for a maximum drift time of 700 ns) and hit rates (up to 300 kHz per tube) put severe requirements on the single-tube efficiency and rate capability. The occupancy is defined as the fraction of time where the MDT is occupied by an event i.e. the MDT is not able to measure a muon track. This number, which directly influences the pattern-recognition efficiency is the main argument for a fast drift gas. At high chamber occupancies the frequency of wrongly reconstructed tracks becomes also significant. This is a further important design criterion in the search for rare signals, such as a new vector boson Z' decays into muons ($Z' \rightarrow \mu\mu$).

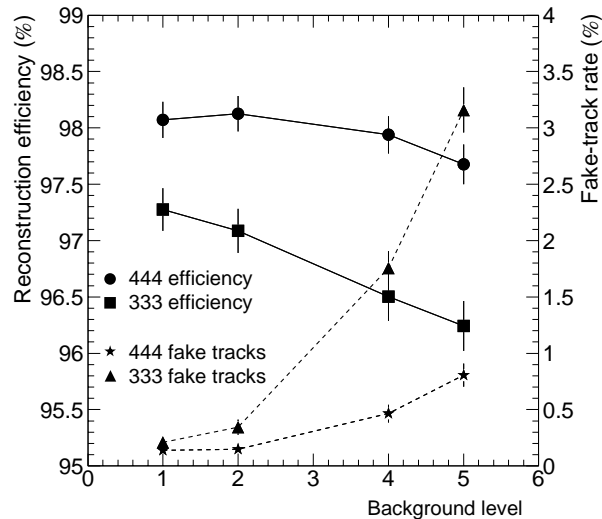


Figure 2.12: Pattern-recognition efficiency as a function of the background level [Atm97a]. A background level of five refers to a safety factor of five on top of the nominal background rate derived from simulation. '444' indicates a chamber configuration with four layers of tubes per multilayer in the inner, middle and outer muon station, '333' indicates three layers.

¹A detailed description of the time slewing correction is in [Rie97].

Figure 2.12 shows the pattern recognition efficiency and the fake-track rate (number of wrongly reconstructed tracks) for different background levels and layout schemes.

Radiation Damage

The high background rates and the need for good momentum resolution are the driving considerations for the MDT operation requirements. One of the biggest concerns is the possible degradation of the drift chamber performance due to large amount of charge deposit on the sense wire. Assuming the background rates given above together with a gas gain of 2×10^4 a charge deposit of 0.6 C per cm of wire for ten years of high luminosity LHC running is expected (including an uncertainty factor of five).

Such a high amount of charge can cause aging effects resulting from deposits of various kinds on the wire and the cathode. These deposits can either reduce the MDT performance or even completely destroy a tube. To minimise these effects we want to operate the chamber at the lowest possible gas gain that is still compatible with the requirements on resolution. The aging problem also puts severe constraints on the choice of gas and construction materials.

It has been found in extensive aging studies that gas mixtures containing hydrocarbons (e.g. CH_4) produce thin deposits on the wire and on the cathode which affect the performance (aging). The current baseline gas (Ar/ CO_2 /93/7) shows no aging but is rather non-linear in the rt -relation [Spe97].

Trigger Rate Capability

A potentially dangerous background for the LVL1 low- p_T muon trigger are muons from K_L decay. This rate is also affected by a large uncertainty, it is however not considered in this thesis.

Chapter 3

Motivation for Background Benchmarking

In section 2.3 we have shown that the background calculations are assumed to have an uncertainty factor of five due to the superposition of different contributions. One contribution is the limited knowledge of the showering process in the absorber and of the ensuing neutron and photon production which is assumed to have an uncertainty of a factor 2.5.

While this figure represents an 'educated guess' it was considered very important to obtain experimental information on this uncertainty, as the level of background influences in a critical way many features of the muon spectrometer.

We have emphasised that the background radiation emanating from the calorimeter and the shielding material is one of the main constraints on the muon spectrometer layout and operation. It influences parameters such as the momentum resolution, the pattern recognition, radiation damage of detector components and the rate capability of the muon and trigger detectors (see section 2.4).

In particular the following issues will be influenced by the precise knowledge of the background:

- The detailed rate performance of the readout electronics.
While the front-end electronics has been designed to function up to ≈ 600 kHz rates, the bandwidth of the readout drivers has not yet been defined. This is a major cost issue.
- The required radiation hardness of the instrumentation.
A large number of commercial items (low and high voltage power supplies, CCD's, hall probes, etc.) will be used. Precise knowledge of the radiation levels will allow the correct choice of this instrumentation, which will have considerable importance on the organisation and cost of this instrumentation.

- Performance of the trigger system.
The muon trigger rate will contribute the dominant fraction of triggers which may be determined by accidental trigger rates. Knowledge of the background will allow the optimal choice of trigger electronics, cost algorithms and will permit a better evaluation of the physics potential with low- p_T muons (B-physics).
- Performance of the spectrometer.
The knowledge of the background will allow optimisation of the pattern recognition programs and hence a better evaluation of the physics potential, particular at high luminosities and beyond design luminosities.

The background has been estimated only through extensive Monte Carlo evaluation with the particle transport code FLUKA [Fas97], but relevant measurements have not been done up to now. In order to reduce the contribution from the showering processes it is hence important to perform background benchmarking measurements in an experimental set-up comparable to the ATLAS shielding. The topic of this thesis is about these benchmarking measurements.

In addition to the experimental set-up the entire set-up is simulated in details with FLUKA. Comparison of the measurements with the simulations places the estimates of the ATLAS hall background on a firm experimental basis and the uncertainties of the ATLAS background simulation can be reduced.

Chapter 4

The Experimental Set-Up H6

4.1 Introduction

For the ATLAS background benchmarking measurements we reproduced an experimental arrangement that approaches rather closely the shielding situation in the ATLAS detector. A mixed pion, proton and kaon beam at the relevant momenta of 40 to 120 GeV/c was directed to an iron absorber of different absorption lengths λ (11λ - 14λ). This set-up is close to the forward part (rapidity $\eta \geq 2$) of the ATLAS experiment where the beam approximates the minimum bias events and where the iron absorber corresponds to the shielding (i.e. calorimetry, beam-pipe, etc.) before the muon spectrometer.

Behind the iron absorber a BGO detector was used for the absolute yield and energy measurements of the particles emanating from the final stages of the hadronic shower. Plastic scintillators were used for counting the beam particles.

This chapter describes in detail the experimental area, the set-up and the data acquisition.

4.2 H6 Area

The ATLAS background benchmarking experiments were performed in the H6 beam line in the North Area of the SPS at CERN. The beam is derived from the T4 target station served by a primary proton beam of 450 GeV/c with typical intensities of several 10^{12} protons per burst. The target is made of a 2 mm \times 160 mm beryllium plate with 300 mm length. The beam line can be operated to transport secondary particles in the rigidity range $5 \text{ GeV}/c \leq p/z \leq 200 \text{ GeV}/c$ (z being the particle charge) [Amb99]. Figure 4.1 shows the layout¹ of the beam line. The experimental set-up for the benchmarking measurements is situated ≈ 430 m upstream the Be-target.

¹All 3-dimensional geometry figures of the experimental set-up are produced with [Vin00c].

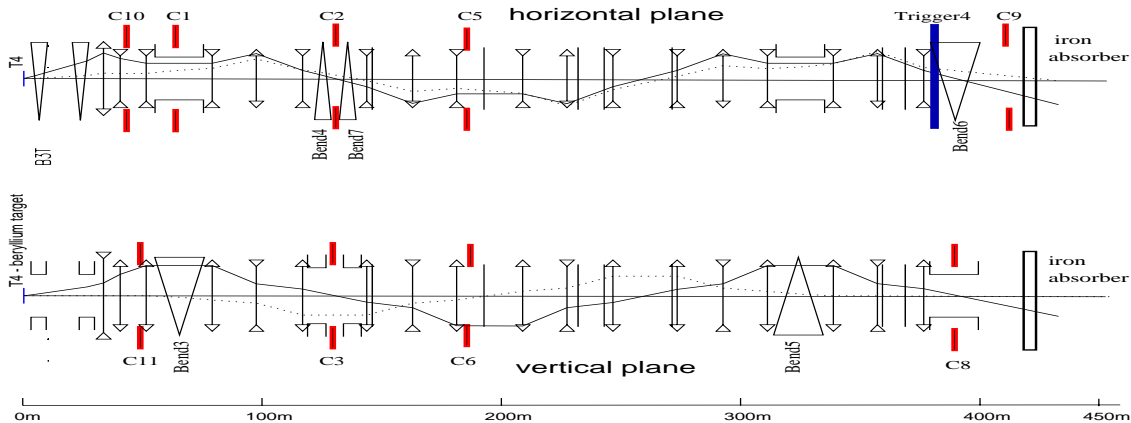


Figure 4.1: Elements of the beam optics in the horizontal and vertical planes. Not to scale, the solid line indicates the excursion of a particle with an angular offset at T4 (1 mrad) and the dotted line shows the trajectories of on-axis particles with a momentum different from the nominal one ($\Delta p/p \sim 1\%$) [Amb99].

The momentum analysis is performed in the vertical plane, while the selection of the production angle is performed in the horizontal plane by means of bending magnets. The direction of incidence of the primary proton beam onto the target is governed by two magnets. Another two magnets behind the target then serve to direct secondary particles of wanted charge-sign, momentum and production angle into the H6 line, whilst deviating the remaining beam onto the dump. Production angles up to 15 mrad are attainable with protons impinging on the target along the beam-axis [Amb99]. Larger production angles (up to 30 mrad) can be obtained by changing the angle of incidence of the primary beam on the target, by means of the first two magnets.

Table 4.1: Used collimators for guiding the H6 beam.

collimator	acceptance	distance from T4
C3	dp/p	127 m
C5	dp/p	191 m
C8	vertical	383 m
C10	horizontal	42 m
C11	vertical	48 m

Three kinds of collimators serve to define respectively the horizontal and vertical angular acceptance and the transmitted momentum interval. They can be opened up to ± 45 mm. Table 4.1 gives a summary of the collimators that were used for the benchmarking measurements.

Several scintillators and Multi Wire Proportional Chambers (MWPC) located along the beam line are used to monitor the steering of the beam and to record the spot size and the

position of the beam. During the background measurements we recorded the data of the scintillator Trigger4 (so called Tr4) that is right in front of the collimator C8 and ≈ 377 m downstream the Be-target.

4.3 Set-Up

A mixed positive charged hadron beam (π^+ , protons, K^+) with a momentum of $p = 40$ GeV/c or $p = 120$ GeV/c, respectively, was used hitting a $200\text{ cm} \times 200\text{ cm}$ cast iron wall with a thickness of 200 cm ($\approx 11\lambda$) and 240 cm ($\approx 14\lambda$). The beam energies are close although higher to the typical secondary particle energies in the forward region of ATLAS (see chapter 12). The set-up is shown in Figure 4.2.

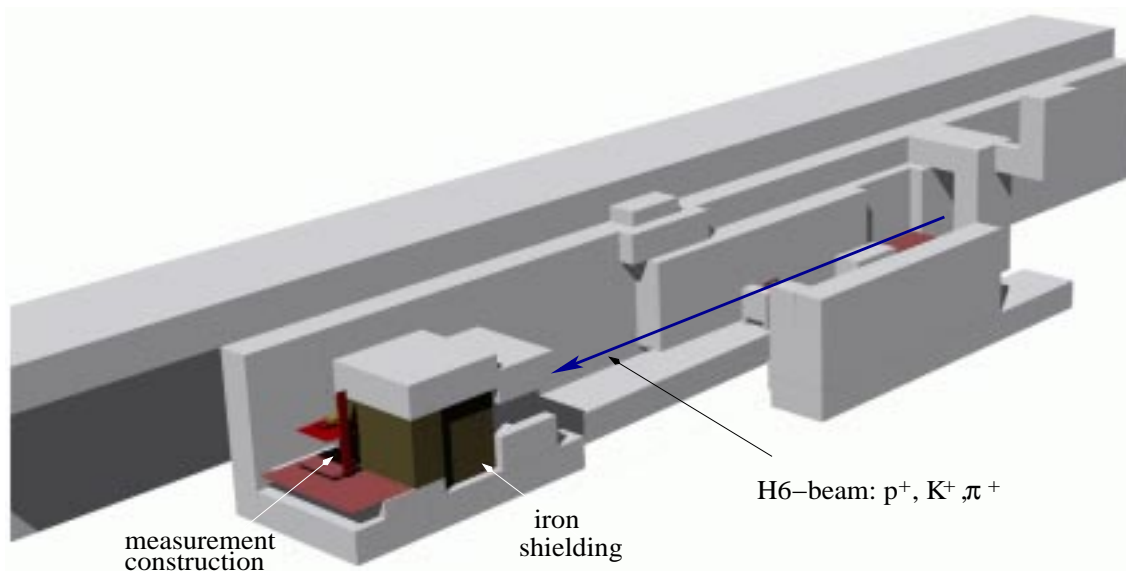


Figure 4.2: Set-up for the ATLAS background benchmarking measurements. The outer shielding of the H6 area is partly removed to show the internal structure of the experimental set-up.

Since we are mainly interested in the photon background prediction we have chosen a detector with a high photon interaction efficiency. For this purpose a BGO ($\text{Bi}_3\text{Ge}_3\text{O}_{12}$) detector is very well suited since it is a high Z ($Z=83$ for Bi), high density ($\rho = 7.13\text{ g/cm}^3$) detector².

The cylindrical BGO detector was placed behind the iron block for the absolute yield and energy measurements of particles, mainly photons and neutrons, emanating from the final stages of the hadronic showers and induced from the beam hitting the absorber. In addition we aligned a $18.5\text{ cm} \times 18\text{ cm} \times 0.5\text{ cm}$ plastic scintillator (so called *ch*) between the iron wall

²More details about the BGO detector and its properties can be found in Appendix A.2.

and the BGO detector. Behind the BGO detector we positioned two $17.8\text{ cm} \times 15\text{ cm} \times 2\text{ cm}$ scintillators (so called $\mu 1$ and $\mu 2$). The aim was to use them possibly as vetoes for charged particles and muons (see Figure 4.3).



Figure 4.3: Photo of the measurement set-up.

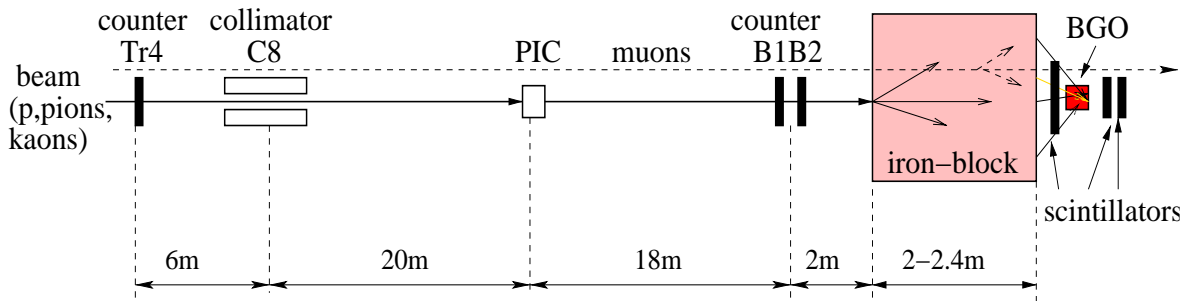


Figure 4.4: Sketch of the H6 area. Tr4, PIC and B1B2 are the beam counters. The collimator C8 can be closed in order to measure only the muon induced signals. The distances are only approximate.

Due to decaying pions in the H6 beam line and due to other beam lines close to H6 there are halo muons inducing signals in the BGO detector. These muons can produce electrons in the absorber. The electrons create a shower and the resulting photons can be measured in the BGO.

In order to yield only the beam induced signals in the BGO, the events induced by halo muons have to be subtracted. By closing the beam collimator C8 the beam is already dumped before the iron block and only the muons reach the absorber. With this method the signals induced only by the muons can be measured. Figure 4.4 shows a sketch of the set-up.

In order to measure the rate per beam particle the number of particles in the beam have to be measured. For that purpose we positioned two $30\text{ cm} \times 10\text{ cm} \times 1\text{ cm}$ scintillators B1 and B2 $\approx 2\text{ m}$ in front of the iron absorber. In order to get the number of particles in the beam when the collimator C8 is closed we recorded also the counts of the scintillator Tr4 upstream C8.

In addition we measured the beam flux with a Precision Ionisation Chamber (PIC) positioned close to the collimator C8 (405 m downstream the target T4). This detector is used for normalising all experimental data of the CERN-EU High Energy Reference Facility CERF [Bir98] to the beam flux. We carried out careful calibration measurements and performance tests of the PIC counter. Since it turned out that the scintillators Tr4 and B1B2 are more precise for the benchmarking measurements, we did not use the PIC counter for further analysis. However, a detailed description of the measurements can be found in [Gsc00a] and [Gsc00b].

4.4 Data Acquisition

4.4.1 Readout Chain

The readout chain used for the BGO is illustrated in Figure 4.5. The photo-multiplier is supplied with a high voltage of -750 V . The original signal from the BGO is about $1.2\ \mu\text{s}$ long. In order to shorten the signal (typically 480 ns) we use a well-timed cable reflection to destructively interfere with the pulse³. To smoothen and amplify the signal a shaping amplifier was used. The signal is then attenuated in three different ways. This allows us to measure the energy spectra in three different energy ranges with three different channels of the ADC. In general the first energy spectrum ranges from $0\text{--}2\text{ MeV}$, the second from $0\text{--}10\text{ MeV}$ and the third from $0\text{--}40\text{ MeV}$. As cross-check for the dead-time corrections we also add a generated pulser-signal of known frequency (68.4 Hz) to the BGO signal.

In order to suppress noise signals, a threshold for the BGO-signal was set in the discriminator. From the measured spectra we see that this threshold is equivalent to $\approx 250\text{ keV}$.

In order to make up for pile-up effects and overshoots of the BGO signals, each signal was extended to $1.5\ \mu\text{s}$ before being counted by the scaler. This allows us to perform a clean and well-known dead-time correction of the BGO counts. In addition the number of events

³A well-chosen length of shorted cable is connected in parallel to the output. After splitting at the junction, one-half the pulse travels down this length of cable where it is reflected back in an inverted state. If T ($T = 240\text{ ns}$) is the delay of this cable, this reflection rejoins the other half at a time $2T$ later, where it interferes with the pulse tail. This leaves a pulse of width $\approx 2T$ ($2T = 480\text{ ns}$) [Leo87].

processed by the computer are counted in a CAMAC scaler.

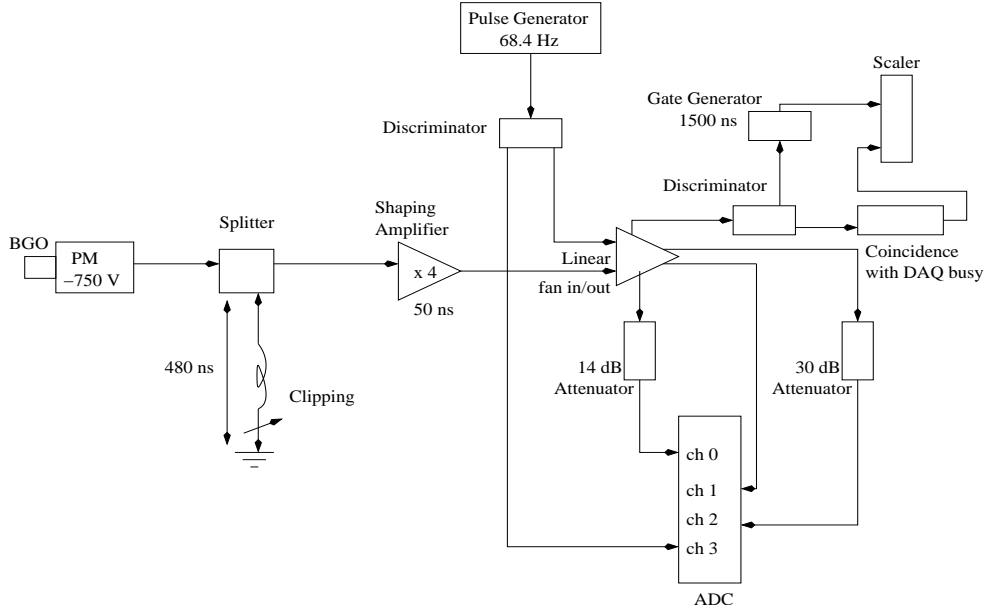


Figure 4.5: Readout chain for the BGO detector.

The three scintillators ch , $\mu 1$ and $\mu 2$ are also driven to an ADC channel, respectively, in order to eventually perform offline different trigger conditions as described in the next section.

The Tr4 beam counter signals go through a discriminator with an output signal of $\tau_{Tr4} = 65$ ns duration. The beam counter signals B1 and B2 are connected with a logical AND. In the following they are called B1B2. These signals are corrected for dead-time with $\tau_{B1B2} = 75$ ns. All beam counter signals B1B2, Tr4 and PIC are counted in the scaler during *inspill* and *outspill*.

4.4.2 Timing

The total SPS cycle lasts 14.4s with a burst length ('spill') of 2.58s. The measurement time during each spill for the benchmarking measurements was not the total spill length but 2s in order to avoid any 'edge effects' (so called *inspill* measurements).

In addition the noise signals originating from the environment were measured for 7s in the time between the spills. In the following these measurements are called *outspill*.

The trigger for the measurements during a SPS cycle was taken from the 'warning early' WE signal directly from SPS. The remaining starts and stops came from a sophisticated arrangement of time generators. Figure 4.6 shows the time-flow during one SPS cycle.

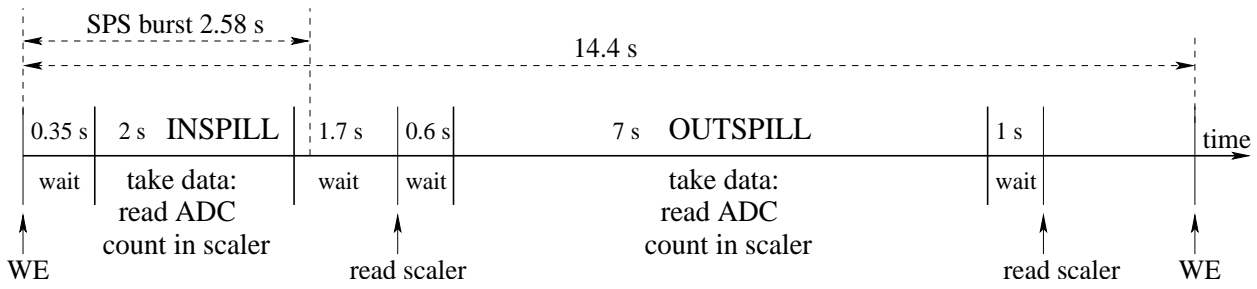


Figure 4.6: Time-flow during one SPS cycle. Data are only taking during *inspill* and *outspill*.

4.4.3 Trigger Conditions

In order to get a good understanding of the different particle natures behind the iron absorber we performed measurements with different trigger conditions. Figures 4.7 to 4.10 show the different trigger-logic schemes to distinguish between the particles.

All BGO signals were read out when the trigger was only provided by the BGO (see Figure 4.7). In the following this is the *inclusive trigger*.

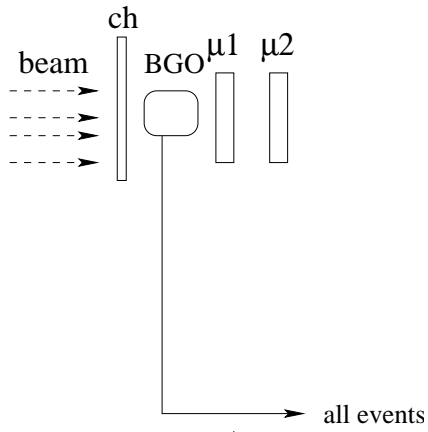
The probability that photons or neutrons interact in the plastic scintillators is very low. We therefore call this trigger *neutral trigger*, when only the BGO-detector gives a signal and none of the scintillators (Figure 4.8).

When the energy of charged particles is high enough, they can pass all three scintillators as well as the BGO. Hence a coincidence signal between all detectors gives us a muon or high energy particle (Figure 4.9). We call this trigger *high-charged trigger*.

Low energy charged particles that pass the scintillator *ch* to the BGO detector but not the muon scintillators $\mu 1$ and $\mu 2$ fulfil the trigger-logic shown in Figure 4.10 and are called *low-charged trigger*.

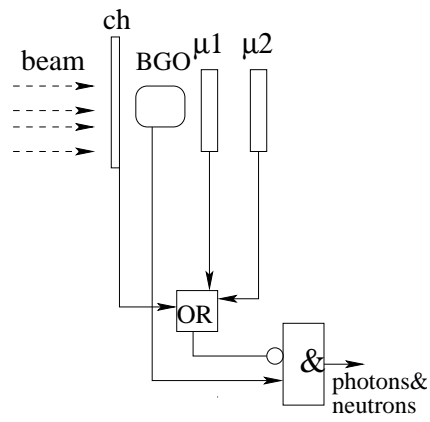
The veto-scintillators (*ch*, $\mu 1$, $\mu 2$) were extended to 350 ns to superimpose well with the BGO signal that was shortened to 50 ns for all trigger-logic applications.

All possibilities were implemented in the DAQ so that all different conditions were counted during a run. However, the spectrum of only one applied trigger condition could be taken. Since the rate of the muons and charged particles was anyway very low we measured the two spectra: with the *inclusive trigger* and with the *neutral trigger*, respectively.



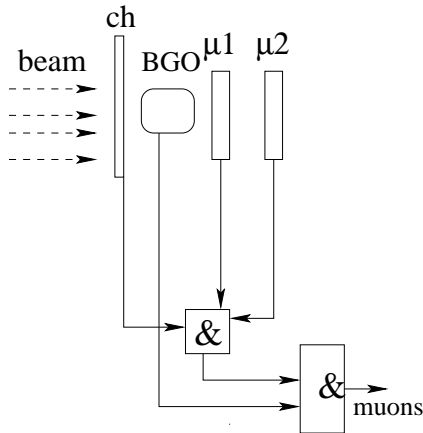
1.)
BGO

Figure 4.7: *Inclusive trigger.*
All BGO signals are read out.



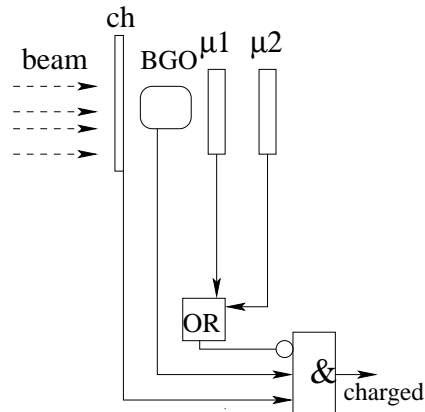
2.)
 $BGO \& \!(ch \text{ OR } \mu 1 \text{ OR } \mu 2)$

Figure 4.8: *Neutral trigger.*
The trigger is provided when only the BGO detector gets a signal.



3.)
 $BGO \& ch \& \mu 1 \& \mu 2$

Figure 4.9: *High-charged trigger.*
A coincidence of all detector signals fulfil this trigger-logic.



4.)
 $BGO \& ch \& \!(\mu 1 \text{ OR } \mu 2)$

Figure 4.10: *Low-charged trigger.*
This trigger is provided when only the BGO and the ch scintillator have a signal and none of the muon scintillators.

Chapter 5

Detector Response Calibration

5.1 Introduction

Before performing complex measurements where all shower processes are included we carried out measurements with simple geometries and well known radioactive sources.

The measurements show us the response of different particles (photons, neutrons) with different energies. Comparing the measurements with the simulations done with FLUKA gives already a first benchmark.

5.2 Photon Response

The photon response of the BGO detector was measured with three different γ -sources in an experimental set-up easily reproducible for the simulations.

5.2.1 Experimental Set-Up

5.2.1.1 Radioactive Sources

For the measurements three different γ -sources in the energy range between 662 keV and 1333 keV were used. The sources consist of thin mylar foils held by a plastic ring of 1.5 cm inner diameter. A small amount of a radioactive isotope had been applied to the mylar foil constituting a point-like γ -ray source. Table 5.1 shows the characteristics of the sources.

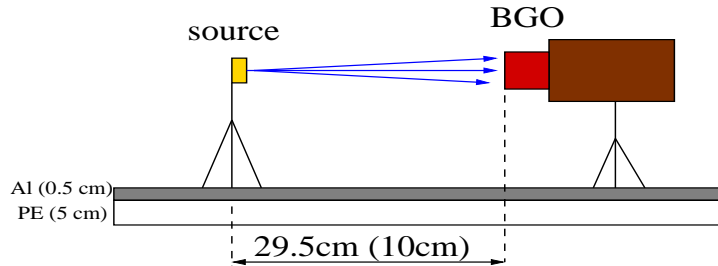
Table 5.1: Sources used for calibration.

element	energy [keV]	activity A_0 29.06.95 in kBq	$T_{\frac{1}{2}}$ in years
^{137}Cs	662	43.1 ± 0.29	30.2
^{54}Mn	835	37.6 ± 0.25	0.855
^{60}Co	1173, 1333	45.9 ± 0.31	5.271

5.2.1.2 Measurement Set-Up

In order to perform a proper simulation of the measurement set-up, the geometry and the materials have to be well defined. Therefore the cylindrical BGO detector (3.8 cm height and 3.8 cm diameter) together with the photo-multiplier was held by an iron support on a 0.5 mm aluminium layer and a 5 cm Polyethylene layer, both with the dimensions 40 cm \times 60 cm. The sources were mounted on an iron pillar. The Cs- and Co-sources were placed with a distance of 29.5 cm to the BGO. Since the Mn-source is quite weak, measurements with this source were done at a distance of 10 cm.

The entire measurement set-up was placed far from any walls and about 1.5 m from the floor in order to minimise the influence of scattered photons. Figure 5.1 shows the set-up.

**Figure 5.1:** Set-up for the calibration measurements.

5.2.1.3 Readout Chain

With some differences the readout chain for the BGO was the same as described in section 4.4.1: The first ADC-channel measures the energy spectrum up to ≈ 2 MeV, the second up to ≈ 7 MeV and the third up to ≈ 15 MeV. The discriminator threshold was set to ≈ 150 keV.

The veto and beam scintillator signals were not of interest in these measurements and therefore not included. The trigger was provided by the BGO itself.

5.2.2 Measurements and Analysis

5.2.2.1 Measurements

The spectra and rates of the Co- and Mn-sources were measured under three different angles to the BGO-detector: 0° , 45° and 90° . The Cs-source was measured only under 0° and 45° . In general one measurement lasted ≈ 24 hours in order to accumulate sufficient statistics.

Additional measurements without sources were performed to subtract the background, mainly from natural radioactivity and parasitic radiation from shielded sources, from the source measurements.

5.2.2.2 Analysis

- *Energy Calibration Curve*

We need an energy calibration function to convert the ADC-bin per ADC-channel to its energy. Due to temperature effects in the BGO and the electronics the ADC-positions of the peaks of the same sources varied within 5 % between the different runs. To avoid bin-to-energy function calculations for all the different measurements all measured spectra were normalised to the ^{40}K (Potassium)¹ photo peak in the background measurement, since this peak can be found in all spectra. After subtracting the pedestal we fit a second-order polynomial

$$\text{Energy} = b \text{Bin} + c \text{Bin}^2 \quad (5.1)$$

to all measured source peaks. This allows us to use for every measurement the same calibration curve. The calibration curve is shown in Figure 5.2.

- *Normalisation*

In order to know the rate in a certain energy range and to evaluate the efficiency we integrate the spectrum within this range. Since the DAQ does not process each BGO event we have to normalise the spectrum with the factor

$$f = \frac{\text{all BGO events}}{\text{DAQ processed events}}. \quad (5.2)$$

The *BGO events* do not need to be dead-time corrected since their rate is about 100 Hz. As a cross-check for the computer dead-time normalisation we add to the BGO signal a generated pulser-signal of known frequency (68.4 Hz). The factor with which the spectrum can also be multiplied is then

$$f = \frac{68.4}{\text{DAQ processed pulser events/s}}. \quad (5.3)$$

¹The ^{40}K (Potassium) photo peak at 1460 keV is a commonly occurring nuclide in the environment.

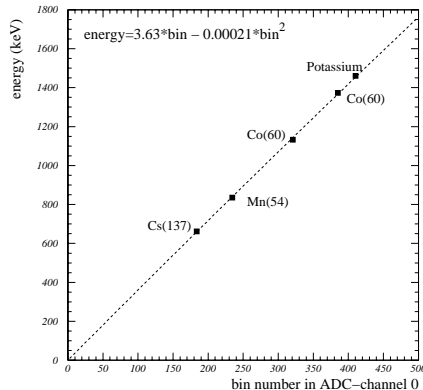


Figure 5.2: Calibration curve for the ADC channel used in the analysis.

We get the *DAQ processed pulser events/s* from counting the entries in an ADC-channel (*ADC 3*) that only gets the pulser-signals. The two different normalisations agree within less than 0.5 %.

5.2.3 Results

5.2.3.1 Measured Source Spectra

Figure 5.3 shows the measurements with the Cs-source under 0° degree to the BGO. Overlaid is the measured background. We see clearly the photo peak of the Cs-source (662 keV) and also the Potassium (1460 keV) and Thorium (2616 keV) photo peaks, both commonly occurring nuclides in the environment (Actually, ^{40}K comes from the bodies of the physicists surrounding the experiment). Subtracting the background from the source measurements yields the pure source spectra as shown in Figure 5.4. One can identify very easily the photo peak, the Compton edge and the backscatter peak².

5.2.3.2 Measured Rates and Uncertainty Contributions

Summing up the entries in the measured spectra within a certain energy interval yields the rate. The statistical uncertainty for all measurements is less than 0.3 %.

The systematic uncertainty contributing to the measured rates are the following:

²A detailed description of photon interactions in matter as well as the signatures in the detector are given in Appendix A.1.

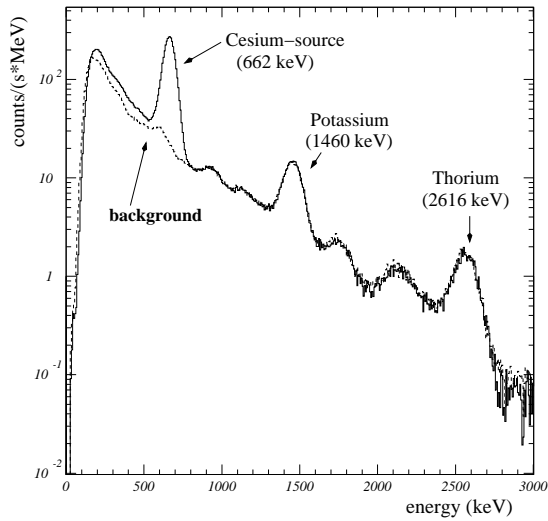


Figure 5.3: Measured spectrum of the ^{137}Cs -source and background spectrum.

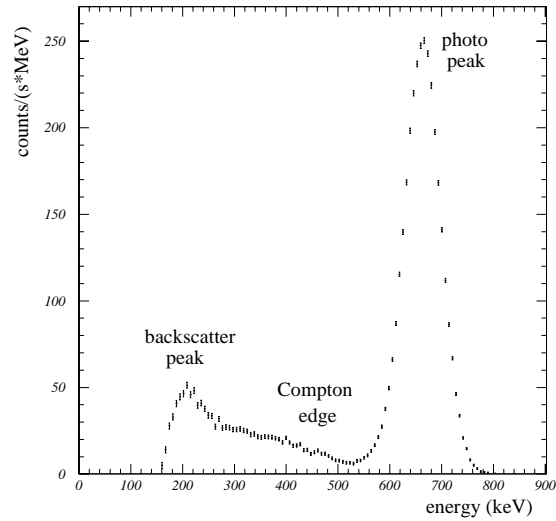


Figure 5.4: Spectrum of the ^{137}Cs -source under 0° degree to the BGO.

- *Radioactive sources*

The activity of the sources is known with an uncertainty of $\sigma=0.67\%$.

- *Geometry*

The distance of the sources to the BGO is known within 1 mm. This yields an error of $\sigma = 0.69\%$ for the Cs- and Co-source rate and $\sigma = 1.96\%$ for the Mn-source rate.

- *Normalising factor*

In section 5.2.2.2 we have shown that the factor to normalise the spectrum to the actual BGO counting rate has an uncertainty of $\sigma = 0.5\%$.

The contribution to the uncertainty of the rate from the energy-calibration is less than 0.01% and hence negligible.

Table 5.2 shows the measured photon rate/s above an energy of 400 keV. The uncertainties are $\approx 1\%$ for the Cs- and Co-source results and $\approx 2\%$ for the Mn-source.

5.2.3.3 Measured Photon Efficiency

The intrinsic detection efficiency of the BGO is defined as

$$\epsilon = \frac{\text{events registered}}{\text{current}} \quad (5.4)$$

where *events registered* are the counts/s of the photons in the BGO and *current*³ is the number of particles/s entering the BGO crystal.

In order to avoid a contribution of the back scattered photons (see Figure 5.4) to the efficiency, the threshold for the *registered events* is 400 keV. Only the particles hitting the BGO crystal and not the detector cover are considered for the *current*. They can be calculated with geometrical considerations.

Table 5.2: Current, rate and efficiency for the different sources measured under different angles to the BGO detector.

angle to BGO	current in BGO/s	rate/s ($E \geq 400$ keV)	efficiency %
¹³⁷ Cs-source			
0°	34.3	24.61 ± 0.26	71.7 ± 0.8
45°	50.5	27.10 ± 0.28	53.6 ± 0.6
⁵⁴ Mn-source			
0°	18.7	10.52 ± 0.21	56.3 ± 1.1
45°	23.5	11.53 ± 0.23	49.2 ± 1.0
90°	28.7	15.43 ± 0.30	53.7 ± 1.0
⁶⁰ Co-source			
0°	58.8	36.46 ± 0.39	62.0 ± 0.7
45°	86.6	39.52 ± 0.41	45.6 ± 0.5
90°	81.4	45.56 ± 0.48	56.0 ± 0.6

In order to define the photon efficiency of the BGO we can only use the 0° results of the Cs- and Co-sources. The reason is that in this situation all particles can be supposed to enter the detector parallel and hence interact during the same track length in the detector. The results for the Mn-source can not be used since the source is too close to the detector, the particles do not enter the detector parallel anymore and therefore the particle track length varies depending on the direction the particles enter the BGO.

Due to the higher geometrical cross-section of a cylinder from the side the counting rate as well as the current entering the BGO crystal is higher for the measurements under 45° and 90°. Nevertheless, the efficiency decreases since the average particle track length through the crystal is smaller in these situations.

³A detailed definition of the quantity *current* can be found in Appendix B.

5.2.4 Comparison of Measurements and Simulations

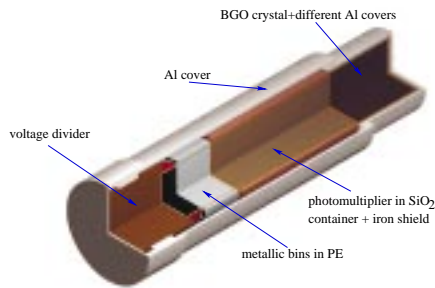


Figure 5.5: *Simulated BGO detector.*

5.2.4.1 Simulation Procedure

For the simulation the entire geometry set-up shown in Figure 5.1 was implemented. In addition, the BGO detector was simulated very accurately with all its materials. Figure 5.5 shows the simulated BGO detector. The simulation is done in two steps:

1. The energy deposition in the BGO detector of photons coming from a 4π point source is simulated with FLUKA. The result is a spectrum produced in the BGO with an energy resolution that is independent of the deposited energy. The resolution is only determined by the energy bin width of the 1024 channels in the spectrum.
2. In order to adapt this spectrum to a real spectrum measured with the BGO detector the energy deposition spectrum has to be convoluted with the BGO resolution function.

The BGO energy resolution depends on the detector and the electronic instrumentation. Since we know that the measured spectrum of a mono-energetic γ -source shows a Poisson distribution around the mean-value, we can assess the standard deviation (in other words the energy resolution) by performing measurements with mono-energetic sources.

For a Cs-source (662 keV) we found out that the standard variation is $\sigma = 36.15$ keV. In order to yield the energy resolution for all energies this measurement result has to be extrapolated. Ref. [Vin00a] shows that the energy dependent standard variation σ for the energy E is

$$\sigma(E) = 1.405\sqrt{E(\text{keV})}. \quad (5.5)$$

The events in each channel of the simulated energy deposition spectrum is then Gaussian smeared with its corresponding σ to yield the final spectrum. Figure 5.6 shows the simulated energy deposition spectrum of the Cs-source. Figure 5.7 displays the spectrum already convoluted with the BGO response.

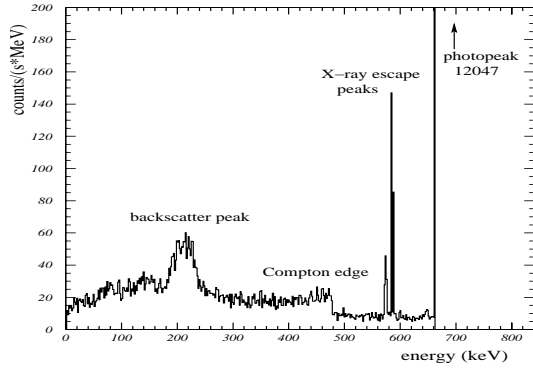


Figure 5.6: Simulated energy deposition spectrum of ^{137}Cs .

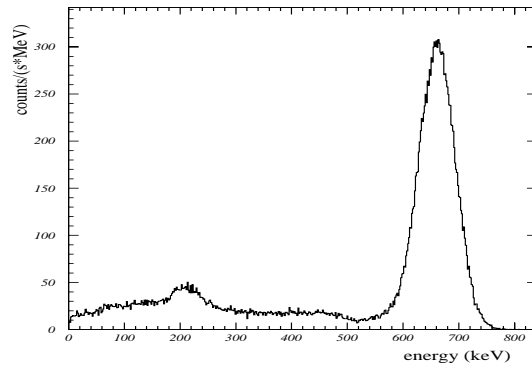


Figure 5.7: Simulated Cs-spectrum convoluted with the BGO response.

5.2.4.2 Comparison

Table 5.3 gives a summary of the measured and simulated rates for all different set-ups. The error of the simulated is the statistical one. We see that apart from the 90° Mn-result they all agree to better than 3%. The average gives an agreement of better than 2%. In Figures 5.8, 5.9 and 5.10 we see the comparison of the measured and simulated spectra of the three different sources for different angles, respectively.

Table 5.3: Measured and simulated rates for all different set-ups.

	Rate/sec with $E \geq 400\text{keV}$		ratio
	meas.	sim.	meas./sim.
^{137}Cs -source			
0°	24.61 ± 0.26	24.3 ± 0.07	1.01 ± 0.01
45°	27.10 ± 0.28	27.1 ± 0.08	1.00 ± 0.01
^{54}Mn -source			
0°	10.52 ± 0.21	10.84 ± 0.01	0.97 ± 0.02
45°	11.53 ± 0.23	11.83 ± 0.01	0.97 ± 0.02
90°	15.43 ± 0.30	16.20 ± 0.02	0.95 ± 0.02
^{60}Co -source			
0°	36.46 ± 0.39	36.5 ± 0.15	1.00 ± 0.01
45°	39.52 ± 0.41	40.0 ± 0.12	0.99 ± 0.01
90°	45.56 ± 0.48	45.2 ± 0.14	1.01 ± 0.01

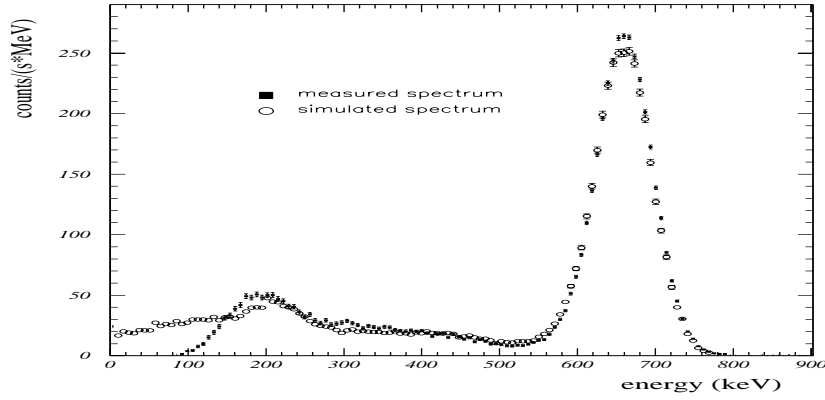


Figure 5.8: Measured and simulated spectra of the ^{137}Cs -source under 45° .

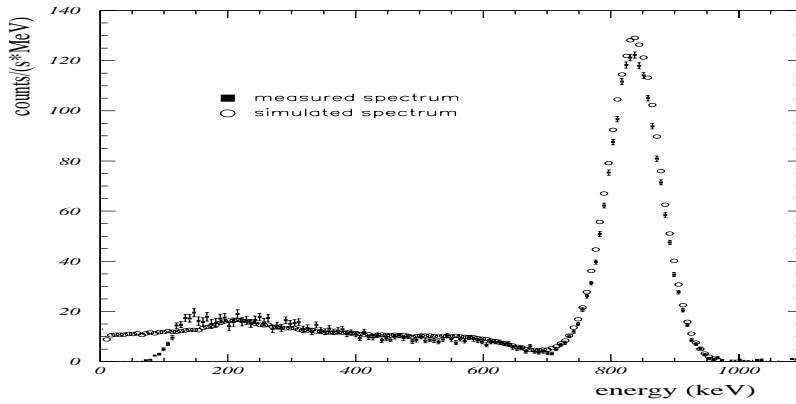


Figure 5.9: Measured and simulated spectra of the ^{54}Mn -source under 90° .

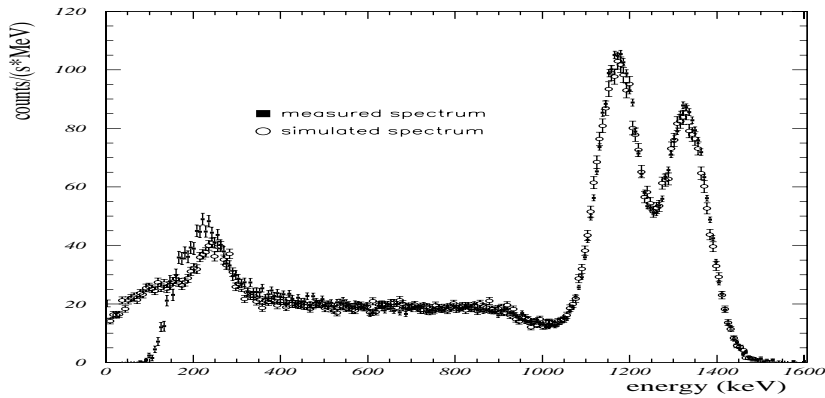


Figure 5.10: Measured and simulated spectra of the ^{60}Co -source under 0° .

5.3 Neutron Response

For our measurements it is also necessary to understand the BGO response to neutrons. Therefore measurements with an ^{241}Am -Be-source of known neutron emission and spectrum were performed. This section describes first the measurements of the neutron/photon ratio of the Am-Be-source. Subsequently, the measurements of the source with the BGO detector are shown.

5.3.1 Neutron/Photon Ratio of the Am-Be-Source

5.3.1.1 Am-Be-Source

The Am-Be-source contains ^{241}Am emitting α particles. They are captured by ^9Be , producing an excited $^{13}\text{C}^*$ that decays into ^{12}C by emitting neutrons and 4.4 MeV photons. The cylindrical source has a diameter of 15.8 mm, a height of 10.7 mm and is surrounded by a steel cylinder in order to absorb low energy photons (≈ 60 keV) originating from the ^{241}Am decay process.

The neutron emission of the Am-Be-source was measured with a Rem-counter[EGG95] calibrated at the PTB [Ott98]. The emission was characterised with an uncertainty of 7%. The results are shown in table 5.4.

Table 5.4: *Characteristics of the ^{241}Am -Be-source.*

Neutron emission A_0	$T_{\frac{1}{2}}$ in years
15.04.1977	
$(2.3 \pm 0.16) \cdot 10^3$	432

Figure 5.11 shows the neutron spectrum of the Am-Be-source.

5.3.1.2 Measurements and Results

The photon emission of the Am-Be-source was measured with a Ge-detector by counting the number of photons in the photo peak and multiplying this number with the efficiency of the detector at this energy. In addition measurements of the background were performed in order to subtract these counts from the source signals. The statistical uncertainty of the measurements is 2%.

The Ge-detector efficiency for photons emitted under 4π per second was calibrated with a ^{288}Th -source. The efficiency calibration uncertainty is 5%.

With this method we measured a photon rate of $763 \pm 41 \text{ s}^{-1}$. The neutron rate at this date was $2220 \pm 155 \text{ s}^{-1}$. Hence for the ^{241}Am -Be-source the ratio of neutrons/photons is 2.91 ± 0.26 .

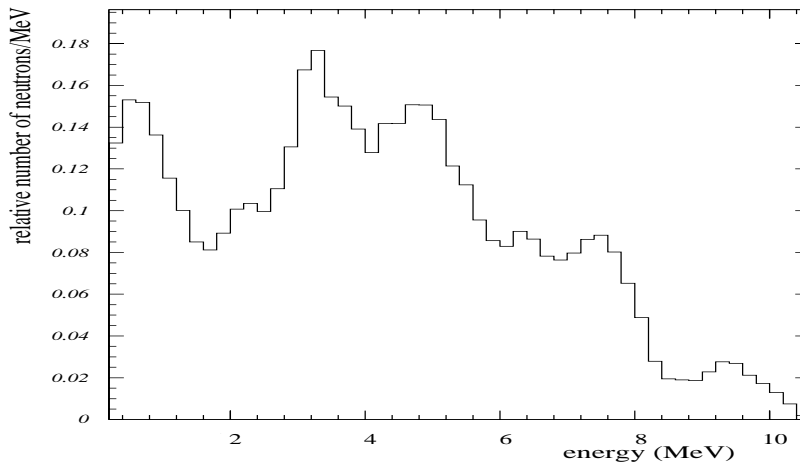


Figure 5.11: Spectral distribution of the neutrons emitted by the ^{241}Am -Be-source [Int00].

5.3.2 BGO Response Measurements for Neutrons

5.3.2.1 Measurements and Analysis

The Am-Be-source was placed 8.5 mm in front of the BGO detector. Measurements of the source and of the background were performed.

For the measurements the same readout chain as described in 4.4.1 was used. The high voltage of the photo-multiplier was increased to -810 V and the signal threshold to ≈ 330 keV in order to suppress additional noise signals from the shaping amplifier.

For the Am-Be-source measurements the bin-to-energy function was calculated by fitting a 2^{nd} -order polynomial $Energy = a + b Bin + c Bin^2$ through five points: Am-Be photo peak (4439 keV), Am-Be single escape peak (3928 keV), Thorium (2616 keV) and Potassium (1460 keV) photo peak as well as the pedestal (0 keV). Another function was calculated for the background measurements with the following peaks: Thorium (2616 keV) and Potassium (1460 keV) photo peak, Thorium single escape peak (2105 keV) and the pedestal (0 keV).

As already shown in section 5.2.2.2 the events processed by the computer had to be normalised to the real number of BGO counts. Dead-time corrections of the BGO counts can be neglected since the measured rate is only ≈ 150 Hz.

5.3.2.2 Measurement Results

Measured Spectrum

The left plot in figure 5.12 shows the source measurement and the background measurement. In the right plot we see the Am-Be spectrum with the background already subtracted.

The spectrum shows very well the photo peak of 4.44 MeV, its single escape peak

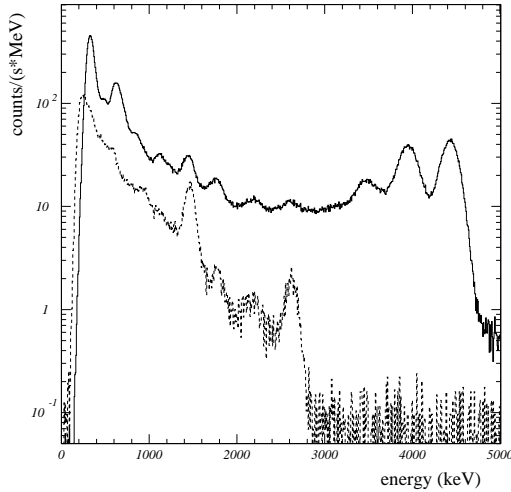


Figure 5.12: *Measured spectra of the ^{241}Am -Be-source and the background.*

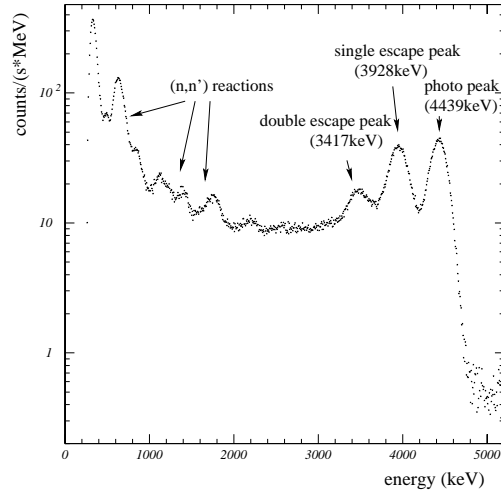


Figure 5.13: *^{241}Am -Be-spectrum with the background subtracted.*

(3.93 MeV) and its double escape peak (3.42 MeV) (see Appendix A.1).

At low neutron energies several discrete states are strongly excited by the (n,n') reaction, giving raise to identifiable gamma rays. In the BGO spectrum the strong, broad group near 0.6 MeV can be attributed to several transitions in Ge isotopes [Chu70] (0.596 MeV and 0.609 MeV in ^{74}Ge , 0.630 MeV in ^{72}Ge , 0.668 MeV in ^{70}Ge , 0.563 MeV in ^{76}Ge). The peaks between 0.9 MeV and 1.6 MeV arise mainly from the decay of the first and second excited states in ^{209}Bi [Hae83].

Measured Rate

The statistical uncertainty of the source measurement is only 0.07%. Of the background measurement it is 0.2%. The uncertainties contributing to the rate are

- *neutron-activity*

The emission is known with an uncertainty of $\sigma = 7\%$.

- *γ -emission*

The photons of the Am-Be-source were measured with an uncertainty of $\sigma = 5.4\%$ (see section 5.3.1.2).

- *geometry*

Since we normalise the simulated photo peak to the measured one, we make up for any geometrical uncertainties and can hence neglect these. Nevertheless this method adds the uncertainty of 2 % derived from the photon agreement between measurements and simulations in section 5.2.4.

The uncertainty of the energy-calibration can be neglected.
The neutron-efficiency will be derived in the next section.

5.3.3 Comparison of Am-Be Measurements with Simulations

5.3.3.1 Simulation Procedure

The simulation was done in the two steps already described in section 5.2.4.1. Photons and neutrons were simulated separately. The geometry and materials of the Am-Be-source were taken into account thoroughly.

5.3.3.2 Spectra

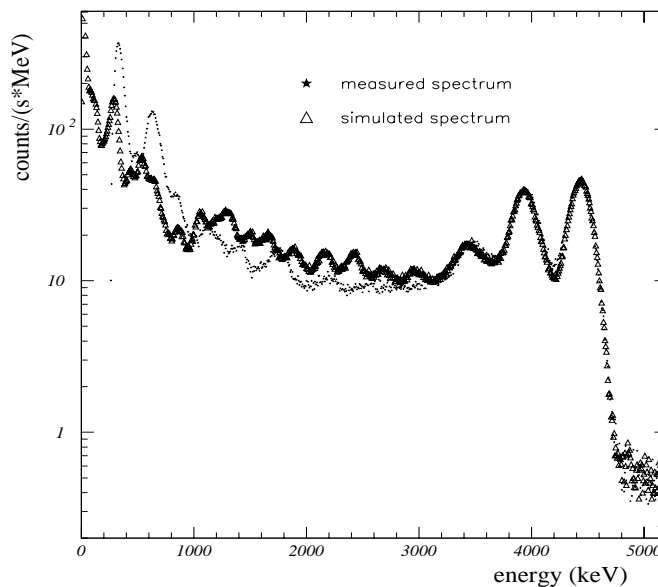


Figure 5.14: Comparison of the measured and simulated ^{241}Am -Be-spectra.

Figure 5.14 shows the comparison between the measured and simulated Am-Be spectra. Since we have shown in section 5.2.4 that the response of photons in the BGO is simulated

very well we normalised the simulated photo peak in the Am-Be-spectrum to the measured one. We see that apart from the γ -contribution the shape of the Am-Be-spectra does not agree well. Especially the peaks originating from $(n,n'\gamma)$ reactions are not reproduced by the simulation. On the other hand additional peaks appear in the simulations which can not be seen in the measurements.

The main reason is that FLUKA uses cross-sections, which give a correct neutron induced energy deposition only on average if a high number of neutrons is applied. The peaks in the simulation show average energy deposition values which can be found in the used FLUKA neutron cross-sections. In the simulation a down-scattered neutron starting from a given energy group [Fas97] induces always a fixed energy deposition. This amount of energy is an average value of all possible energy depositions caused by neutrons of this energy group. However, the total counting rate should not be distorted due to this procedure. In addition the total average energy deposition of the spectra should not be influenced by these FLUKA specific neutron peaks.

More details about this effect can be found in Ref. [Vin00b].

5.3.3.3 Rate

In order to determine the measured neutron rate the simulated photon rate was subtracted from the total measured one. Table 5.5 gives a summary for different energy-cuts. The uncertainty of the measurements is only the statistical one. The uncertainty of the neutron- (photon-) activity as well as the normalisation is included in the uncertainty of the simulated neutron (photon) emission.

We find out that the measured and simulated neutron rates agree within less than 30 %.

Table 5.5: Measured and simulated rates for different energy-cuts.

type of rate	0.4 < E < 6.5 MeV	1 < E < 6.5 MeV	2 < E < 6.5 MeV
	counts/s		
all_{meas}	96.47 ± 0.1	58.85 ± 0.06	43.37 ± 0.04
$\gamma_{sim} + n_{sim}$	85.1 ± 3.9	64.5 ± 2.9	44.5 ± 2.2
γ_{sim}	44.1 ± 2.5	40.6 ± 2.3	35.6 ± 2.1
n_{sim}	40.9 ± 3.0	23.9 ± 1.7	9.0 ± 0.7
$n_{meas} = all_{meas} - \gamma_{sim}$	52.3 ± 2.5	18.2 ± 2.3	7.8 ± 2.1
n_{meas}/n_{sim}	1.28 ± 0.11	0.76 ± 0.11	0.87 ± 0.24

5.3.3.4 Measured Efficiency for Neutrons

The neutron measurement efficiency ϵ_n is

$$\epsilon_n = \frac{n_{meas}}{N_n} \quad (5.6)$$

where n_{meas} is the measured neutron rate shown in Table 5.5 and the number of neutrons entering the BGO crystal is $N_n = 340.5 \pm 24.8$ neutrons/s. The uncertainty of N_n consists of the the neutron-activity uncertainty and the uncertainty derived from the normalisation of the photo peaks.

Table 5.6 shows the results for different energy intervals. We see that the neutrons deposit their energy mostly in the lower energy range.

Table 5.6: *Measured neutron efficiencies.*

	$0.4 < E < 6.5 \text{ MeV}$	$1 < E < 6.5 \text{ MeV}$	$2 < E < 6.5 \text{ MeV}$
ϵ_n	$(15.4 \pm 1.4) \%$	$(5.4 \pm 0.8) \%$	$(2.3 \pm 0.6) \%$

5.3.3.5 Error Estimates of the Simulated Neutron Energy-Deposition

Subtracting the simulated photon spectrum from the measured Am-Be results yields the measured neutron spectrum. Figure 5.15 shows the comparison of the simulated and the measured neutron spectra. We see that there is poor agreement in the range between $0.4 < E < 1 \text{ MeV}$. The agreement is better for $E > 1 \text{ MeV}$.

We therefore determine a global uncertainty of the simulation of the energy-deposition in

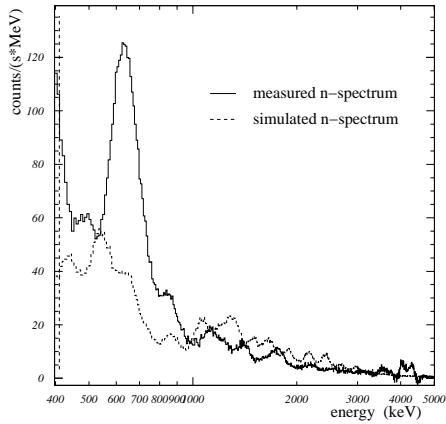


Figure 5.15: *Measured and simulated neutron spectra.*

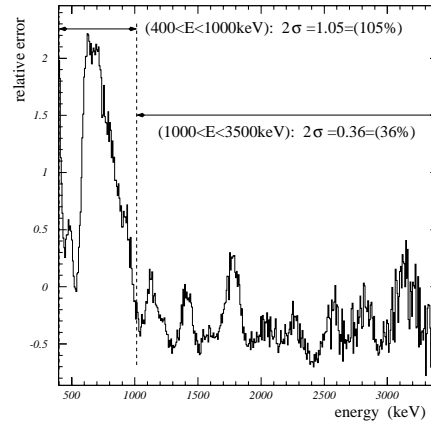


Figure 5.16: *Relative error $\frac{meas_i - sim_i}{sim_i}$ of the neutron simulation.*

the BGO-detector by calculating for each energy-bin $i = Ebin$ the ratio

$$r_i = \frac{meas_i - sim_i}{sim_i}. \quad (5.7)$$

Figure 5.16 shows the ratio. Averaging the ratio r_i between a certain energy interval

$$2\sigma = \frac{\sum_{i=Ebin_{min}}^{Ebin_{max}} |r_i|}{Ebin_{max} - Ebin_{min}}. \quad (5.8)$$

yields the averaged simulation uncertainty.

The uncertainty for two different energy regions is calculated. Between $Ebin_{min}=400$ keV and $Ebin_{max}=1000$ keV we find the uncertainty $2\sigma = 105\%$. Between $Ebin_{min}=1000$ keV and $Ebin_{max}=3500$ keV we obtain $2\sigma = 36\%$.

5.4 Summary

In section 5.2 measurements of three different γ -sources (^{137}Cs (662 keV), ^{54}Mn (835 keV), ^{60}Co (1173, 1333 keV)) were compared with the simulations.

The rates agree at the 2% level. We have also shown that the shape of the spectra is simulated very well.

Section 5.3 shows the neutron response calibration of the BGO detector with an ^{241}Am -Be-source.

The photon emission of the Am-Be-source was measured with a Ge-detector. We found that the ratio of the emitted neutrons/photons is 2.91 ± 0.26 .

The measured spectrum of the Am-Be-source with the BGO shows the typical 4.4 MeV photo peak as well as its single escape and double scape peaks. The neutrons induce signals mainly via $(n,n'\gamma)$ reactions resulting into strong broad peaks around 0.6 MeV and between 0.9 MeV and 1.6 MeV.

The neutron rate and efficiency was determined by subtracting the simulated photon rates from the total measured one. The measured neutron efficiency for $0.4 < E < 6.5$ MeV is $\epsilon_n = 15.4\%$.

The comparison with the simulations show that the neutron rates agree within 30%.

The spectra do not agree very well, since FLUKA uses cross-sections that give a correct neutron induced energy deposition only on average.

We therefore find averaged uncertainties in the simulated neutron spectra of $\sigma = 52.5\%$ for $0.4 < E < 1$ MeV and $\sigma = 18\%$ for $E > 1$ MeV.

Chapter 6

Scope of the Benchmarking Measurements in H6

6.1 Overview of the Measurements

For the background benchmarking measurements in H6 we performed measurements with different settings in order to get a good understanding of the experimental area, to reduce systematic effects and assess residual gamma activities from other sources. In the following the different data taking conditions are explained. The results will be shown in chapter 9.

1. **Beam momenta** $p_{beam} = 40 \text{ GeV}/c$ and $p_{beam} = 120 \text{ GeV}/c$

As described in section 4.2 the H6 beam line can be operated to transport secondary particles in the momentum range $5 \text{ GeV}/c \leq p/z \leq 200 \text{ GeV}/c$ (z being the particle charge). The default momentum is $120 \text{ GeV}/c$ to meet best the different requirements of the other two beam lines extracted from target T4. Since we want to measure closest to the ATLAS requirements, where the typical secondary particle momenta in the forward region of ATLAS are between $5 \text{ GeV}/c$ and $35 \text{ GeV}/c$ we performed also measurements with $40 \text{ GeV}/c$ beam momentum. With this value there can still be enough intensity of the beam achieved, which would not be possible with a lower momentum. Depending on the momentum the H6 beam consists of different percentages of

Table 6.1: H6 beam composition for $p_{beam} = 40 \text{ GeV}/c$ and $p_{beam} = 120 \text{ GeV}/c$ at the iron absorber.

beam momentum	pions (π^+)	protons	kaons (K^+)
40 GeV/c	85%	12%	3%
120 GeV/c	61%	35%	4%

protons, pions and kaons. Table 1 shows the composition of the beam at the position

of the iron block.

2. Measurement positions *on beam-axis* and *off beam-axis*

Measurements were performed at two different positions behind the iron block. Figure 6.1 shows a sketch of the set-up. The first position was nearly on the beam-axis where the BGO was only ≈ 8 cm off the beam. In the following we call that position *on beam-axis*. The second measurement position was ≈ 58 cm off the beam-axis (so called *off beam-axis*).

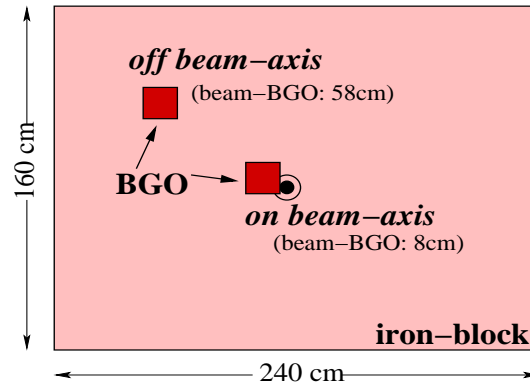


Figure 6.1: Two different BGO measurements positions behind the iron absorber.

3. 200 cm iron absorber and 240 cm iron absorber

In order to understand better systematic effects we performed measurements behind 200 cm and 240 cm iron absorber.

4. High and low intensities

For each setting we carried out measurements with two different beam intensities (typically factor 2-3 difference). For that purpose we changed the widths of the beam collimators in Table 4.1. This allows us to get a good understanding of all residual gamma activities.

5. Collimator C8 setting

From previous test-beam measurements we learned that the signals measured with the BGO detector are not only induced by the beam-particles, but also by the halo muons.

In order to assess only the beam induced signals, we have to subtract the muon induced signals. By closing the collimator C8 the beam is already dumped before the iron block and only the muons can reach the iron. We therefore need to perform two measurements: one run where the collimator C8 is open (in the following this is called *C8* \uparrow) and hence the beam-particle and muon induced signals are taken. the second measurement is with C8 closed (*C8* \downarrow) where only signals from muons are induced.

6. Different trigger conditions

In order to get a good understanding of the experimental set-up we performed measurements with the different trigger conditions shown in Figures 4.7 to 4.10.

Table 6.1 gives a summary of all different measurement conditions for the benchmarking measurements. For example at the position behind 200 cm iron, *on beam-axis* and with $p_{beam} = 40 \text{ GeV}/c$ we performed measurements both for low and high beam intensity with the *inclusive trigger* or *neutral trigger*, respectively, with the collimator C8 open (C8 \uparrow) and C8 closed (C8 \downarrow). The different C8 collimator setting measurements are anyway linked together since we always have to subtract the C8 closed measurements from the C8 opened measurements in order to obtain the only beam induced signals.

In addition we counted during all of these measurements the signals fulfilling the remaining trigger conditions (i.e. *low-charged trigger* and *high-charged trigger*).

Table 6.2: Summary of different benchmarking measurements .

iron absorber	measurement position	intensity	<i>inclusive trigger</i> <i>neutral trigger</i>			
			collimator C8 setting			
$p_{beam} = 40 \text{ GeV}/c$						
200 cm	<i>on beam-axis</i>	low high	C8 \uparrow	C8 \downarrow	C8 \uparrow	C8 \downarrow
200 cm	<i>off beam-axis</i>	low high	C8 \uparrow	C8 \downarrow	C8 \uparrow	C8 \downarrow
240 cm	<i>on beam-axis</i>	low high	C8 \uparrow	C8 \downarrow	C8 \uparrow	C8 \downarrow
240 cm	<i>off beam-axis</i>	low high	C8 \uparrow	C8 \downarrow	C8 \uparrow	C8 \downarrow
$p_{beam} = 120 \text{ GeV}/c$						
200 cm	<i>off beam-axis</i>	low high	C8 \uparrow	C8 \downarrow	C8 \uparrow	C8 \downarrow
240 cm	<i>on beam-axis</i>	low high	C8 \uparrow	C8 \downarrow	C8 \uparrow	C8 \downarrow
240 cm	<i>off beam-axis</i>	low high	C8 \uparrow	C8 \downarrow	C8 \uparrow	C8 \downarrow

6.2 Auxiliary Measurements

Several auxiliary measurements have to be carried out in order to perform reliable benchmarking measurements. The following sections describe the measurements and results for the BGO energy calibration as well as the beam flux calibration.

6.2.1 BGO Energy Calibration

Calibration measurements with different sources were done whenever either the iron thickness, the beam momentum, the measurement position or the intensity were changed. Whereas in section 5.2.2.2 we calculated for all measurements only one bin-to-energy calibration curve

$$Energy = b Bin + c Bin^2 \quad (6.1)$$

by normalising all spectra to the ^{40}K photo peak in the background measurements, we now calculate for each different set-up its energy calibration curve. For that purpose we used the ^{137}Cs , ^{54}Mn , ^{60}Co described in section 5.2 and the 4.4 MeV photo peak of the $^{241}\text{Am-Be}$ source described in section 5.3 as well as its single and double escape peaks.

In addition we utilised the fact that in the benchmarking measurements there is a dom-

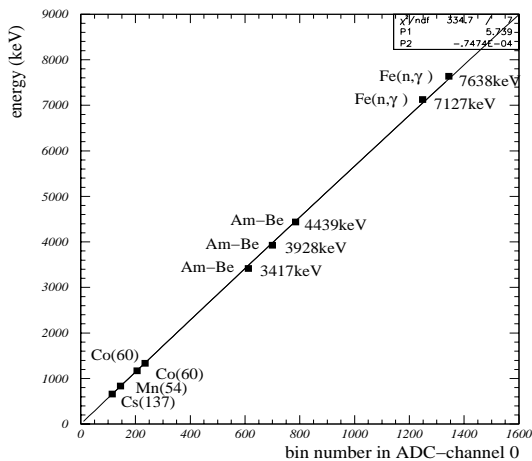


Figure 6.2: Energy calibration curve for the ADC channel that measures the spectra up to ≈ 10 MeV.

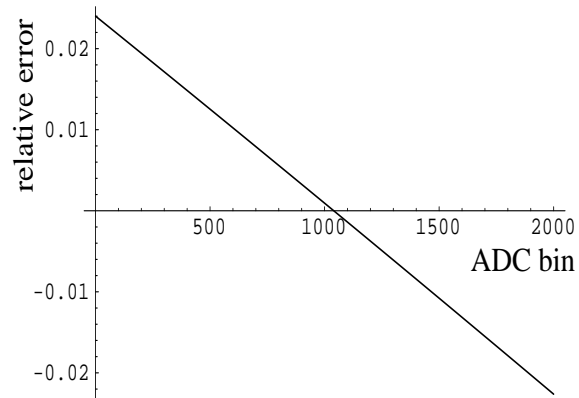


Figure 6.3: Relative error of the two calibration curves showing the largest differences.

inant photo peak around 7.64 MeV, originating from two typical (n,γ) reactions in iron. The resulting photon energies are 7.631 MeV and 7.646 MeV. The energy resolution of the BGO detector is not good enough to distinguish between these two photo peaks resulting in an averaged peak around 7.64 MeV. This photon peak as well as its single escape peak

at 7.13 MeV allow us to obtain an energy calibration curve with points up to the relevant energies in the measured spectra.

Figure 6.2 shows a typical calibration curve for the ADC channel that measures the spectra up to ≈ 10 MeV.

Since these measurements were always done shortly before the benchmarking measurements, the only possibilities of error contributions are from the drift of the ADC or BGO temperature-effects during the measurements.

In order to assess these errors we compared the calibration curves that differ most. Figure 6.3 shows the relative error of these calibration curves. One can see that it is less than 3%. Applying these functions for the same run and calculating the rate shows that the difference in the rate is less than 0.01%. We can therefore neglect the error contribution of the energy calibration.

Non-linearity of the Energy Response

We have seen that the energy response of the set-up is linear up to ≈ 9 MeV. In section 8.2.2 we will see that the energy response becomes non-linear above ≈ 12 MeV, as seen by the apparent energy loss of muons traversing the BGO.

The signal processing chain after the BGO was checked to be linear up to energies much larger than the muon signal. Since the energy deposit of the muons in the BGO is also a well known number we suspect the photo-multiplier to be the source of the non-linearity. In order to check this hypothesis we increased the operating voltage which should lower the energy where the response becomes non-linear.

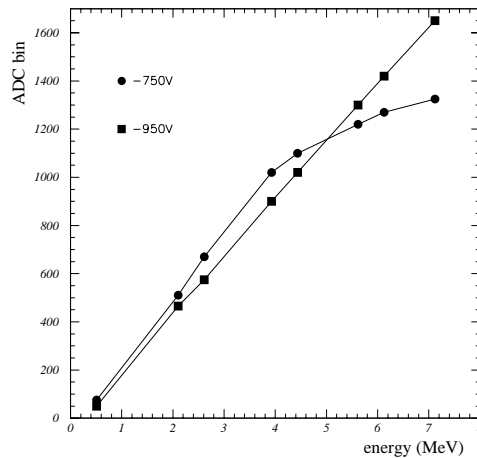


Figure 6.4: *Non-linearity measurements for different photo-multiplier voltages.*

Figure 6.4 shows the ADC bins versus the energy of a high energy gamma ray calibration

source [Kin84] with energies up to 7.1 MeV for photo-multiplier voltages of -750 V and -950 V. For -950 V we clearly see the non-linearity. For the operating voltage of -750 V we find a linear response in the energy range of interest for these measurements.

6.2.2 Beam Flux Calibration

During each measurement run the number of particles in the beam are measured with the scintillator Tr4 as well as with the coincidence signal B1B2 of the two scintillators B1 and B2 right in front of the iron block.

6.2.2.1 Beam Alignment

In principle the beam is aligned with beam monitors along the H6 beam line. However, we found out that the beam can be misaligned right in front of the iron absorber which results in the fact that the beam is partly absorbed in the collimator C9 which is ≈ 3 m upstream the iron block.

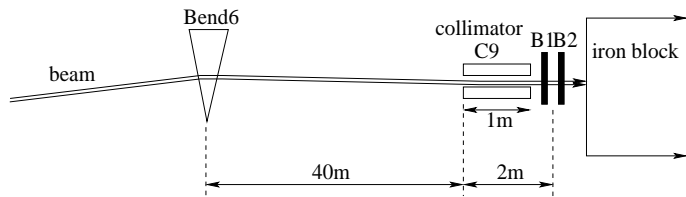


Figure 6.5: Sketch of the beam alignment measurements.



Figure 6.6: Photo of the beam. The horizontal beam-dimensions are $6\sigma=22$ mm. The vertical one is $6\sigma=17$ mm.

We therefore realigned the beam after each beam momentum change ($p_{beam} = 40$ GeV/c, $p_{beam} = 120$ GeV/c). Figure 6.5 shows the set-up for these measurements.

We closed the collimator C9 up to a point where the slit was only 3 mm. Directly behind C9 there are the scintillators B1B2 measuring the beam intensity. Scanning the bending magnet current of Bend 6 versus the beam intensity yields the magnet strength where the beam passes directly through the C9 slit. For the beam with $p_{beam} = 40$ GeV/c a change

of 6 A bends the beam for 37 mm at C9. The final setting for Bend6 was -200.6 A for $p_{beam} = 40$ GeV/c and -597.5 A for $p_{beam} = 120$ GeV/c.

In addition we regularly took photos of the beam by putting a Polaroid exactly in front of C9 and exposing it to $\approx 4 \times 10^6$ beam particles. Figure 6.6 shows a photo where the beam is well aligned. We measured a vertical beam distribution of $\sigma=2.83$ mm and a horizontal distribution of $\sigma=3.67$ mm.

These values are used to characterise the beam-distribution in the simulations.

6.2.2.2 Offset Measurements

When the magnets of the H6 beam line are switched off, the beam coming from the Be-target T4 can not reach the iron absorber. However, the scintillators Tr4 and B1B2 measure a certain amount of counts during *inspill*. This is due to remanent radioactivity and caused by other beam lines with a big halo that are close to the H6 beam line or some particles from the target T4 that can still reach the counters.

Since we have to subtract these offsets from the beam flux during a measurement, we have to know the level of the offsets. Therefore, before each new set-up we measured the scintillator offsets by switching off the magnets of the H6 beam line.

Table 6.3 shows the offsets $\langle B1B2offset \rangle$ and $\langle Tr4offset \rangle$ averaged over more than 100 SPS cycles and obtained for all different measurement settings. The errors are the standard deviations of the histograms.

Table 6.3: Measured offsets $\langle B1B2offset \rangle$ and $\langle Tr4offset \rangle$ for all different settings when the H6 beam is switched off.

iron	beam-axis	counts/s	
		$\langle B1B2offset \rangle \pm r.m.s$	$\langle Tr4offset \rangle \pm r.m.s$
40 GeV/c			
200 cm	<i>on</i>	3400±108	32153±695
200 cm	<i>off</i>	2940±178	30861±526
240 cm	<i>on</i>	2716±113	29589±456
240 cm	<i>off</i>	2718±113	29612±501
120 GeV/c			
200 cm	<i>off</i>	2803±226	18569±388
240 cm	<i>on</i>	2579±129	20822±567
240 cm	<i>off</i>	2655±204	20627±964

6.2.2.3 Normalising the Beam Counters

Since the scintillators B1B2 are only 2 m in front of the iron block, these detectors measure best the number of particles impinging on the iron block.

However, when we perform the measurements with the collimator C8 closed, B1B2 can not count the beam particles since they are already absorbed. Hence we have to use the data of Tr4 and normalise them to B1B2.

The normalisation factor $f_{Tr4toB1B2}$ is calculated from the corresponding measurements with C8 open. For each SPS cycle we histogram the ratio

$$f_{spill} = \frac{B1B2 - \langle B1B2offset \rangle}{Tr4 - \langle Tr4offset \rangle}. \quad (6.2)$$

B1B2 and Tr4 are corrected for dead-time with $\tau_{B1B2} = 75$ ns and $\tau_{Tr4} = 65$ ns, respectively. $\langle B1B2offset \rangle$ and $\langle Tr4offset \rangle$ are the averaged offset values from Table 6.3 for each corresponding measurement run.

The mean value of equation (6.2) is then the normalisation factor $f_{Tr4toB1B2}$.

The uncertainty of the normalisation factor is dominated by dead-time corrections. We assume that the inaccuracy of τ_{B1B2} is 15 ns and of τ_{Tr4} it is 5 ns. Error propagation of the mean values in equation (6.2) gives us the uncertainty of the normalisation factor $f_{Tr4toB1B2}$. The uncertainty of the mean value in the histograms can be neglected compared to the uncertainty calculated with the error propagation.

Table 6.4 shows the normalisation factors $f_{Tr4toB1B2}$ and its uncertainties for all different settings.

Table 6.4: Normalisation factor $f_{Tr4toB1B2}$ for all different measurement settings.

iron	beam-axis	$f_{Tr4toB1B2} \pm \Delta f$ low intensity	$f_{Tr4toB1B2} \pm \Delta f$ high intensity
40 GeV/c			
200 cm	<i>on</i>	0.972±0.007	0.974±0.009
200 cm	<i>off</i>	0.954±0.010	0.955±0.0430
240 cm	<i>on</i>	0.941±0.004	0.947±0.007
240 cm	<i>off</i>	0.949±0.024	-
120 GeV/c			
200 cm	<i>off</i>	0.950±0.005	0.961±0.018
240 cm	<i>on</i>	0.886±0.010	0.906±0.005
240 cm	<i>off</i>	0.900±0.006	0.941±0.022

Chapter 7

Analysis Procedure of the Measurements

7.1 Overview

For all different measurements summarised in Table 6.1 we want to derive the signal rate of the particles that emanate the absorber and are induced by the beam particles impinging the iron absorber.

The signal rate R_{BP} can be described as

$$R_{BP} = \frac{EV_{BP}}{BP} = \frac{\text{Events induced by the beam particles}}{\text{beam particles}} \quad (7.1)$$

where BP is the number of beam particles/s and EV_{BP} are the emanating particles/s induced by the beam particles and measured behind the absorber.

However, it is not possible to obtain these quantities in a single measurement. Several corrections have to be considered:

- As already explained in section 6.1 it is not possible to directly measure EV_{BP} during a run, since the events that are measured by the BGO are not only induced by the beam particles, but also by the halo muons. We hence have to subtract the muon induced signals. This is the reason why to each C8 open measurement a C8 closed measurement is linked. The signal rate can be written in general as

$$R_{BP} = R_{C8\uparrow} - R_{C8\downarrow} = \frac{EV_{C8\uparrow}}{BP_{C8\uparrow}} - \frac{EV_{C8\downarrow}}{BP_{C8\downarrow}} \quad (7.2)$$

with $R_{C8\uparrow}$ is the signal rate measured during the C8 opened runs and $R_{C8\downarrow}$ when C8 is closed. The different contributions to equation (7.2) will be described in details in section 7.2.

- The events/s for both C8 collimator settings in equation (7.2) can not be taken directly from the scaler readout. They have to be dead-time corrected in consideration of the different trigger conditions. Section 7.2.1 will show in details this method.
- The beam particles/s BP are measured with the scintillators Tr4 and B1B2, respectively. When C8 is open B1B2 gives the number of particles in the beam $BP_{C8\uparrow}$. However, the counts have to be dead-time corrected and the offsets from Table 6.3 have to be subtracted.

In order to obtain the number of beam particles/s $BP_{C8\downarrow}$ when C8 is closed we have to take the Tr4 reading and normalise it with the normalisation factors in Table 6.4. Section 7.2.2 will describe these methods.

In addition we measure the spectral distribution (i.e. the absolute yield and energy) of the emanating particles. Section 7.3 will show the procedure to obtain these spectra.

7.2 Signal Rate

When the beam hits the iron absorber i.e. when the beam is switched on and the collimator C8 is open (C8 \uparrow) the BGO detector counts a certain number of events $EV_{C8\uparrow}^{in}$ during *inspill*. These events consist of

- the particles emanating from the final stages of the hadronic showers and induced from the beam hitting the absorber EV_{BP}
- the events induced by the halo muons $EV_{\mu_{ind}}$
- the residual background from activations in the surrounding EV_{rbg} .

Writing

$$EV_{C8\uparrow}^{in} = EV_{BP} + EV_{rbg} + EV_{\mu_{ind}} \quad (7.3)$$

we can calculate the signal rate R_{BP} induced by the beam particles with

$$R_{BP} = \frac{EV_{BP}}{BP} = \frac{EV_{C8\uparrow}^{in} - EV_{rbg}}{BP} - \frac{EV_{\mu_{ind}}}{BP} = R_{C8\uparrow} - R_{C8\downarrow}. \quad (7.4)$$

As shown in section 4.4.2 we measure for each run also the events/s during *outspill*. These events/s EV^{out} correspond to the natural background signals EV_{rbg} . So with $EV_{rbg} = EV^{out}$ we can measure the rate contribution $R_{C8\uparrow}$

$$R_{C8\uparrow} = \frac{EV_{C8\uparrow}^{in} - EV^{out}}{BP_{C8\uparrow}} = \frac{EV_{C8\uparrow}}{BP_{C8\uparrow}} \quad (7.5)$$

during the runs where C8 is open.

The contribution of $EV\mu_{ind}$ can only be assessed by closing the collimator C8 (C8↓). Hence performing another measurement gives us with

$$EV_{C8\downarrow}^{in} = EV\mu_{ind} + EV_{rbg} \quad \text{and} \quad EV_{rbg} = EV^{out} \quad (7.6)$$

the signal rate

$$R_{C8\downarrow} = \frac{EV_{C8\downarrow}^{in} - EV^{out}}{BP_{C8\downarrow}} = \frac{EV_{C8\downarrow}}{BP_{C8\downarrow}}. \quad (7.7)$$

Combining the two results yields then the signal rate

$$R_{BP} = R_{C8\uparrow} - R_{C8\downarrow}. \quad (7.8)$$

We see from equations (7.5) and (7.7) that for each of these measurements we have to calculate the signal rate

$$R = \frac{EV^{in} - EV^{out}}{BP}. \quad (7.9)$$

In the following sections the parameters in equation (7.9) are described in more details.

7.2.1 Emanating Particles

During each SPS cycle the BGO detector counts the emanating particles that meet the respective trigger conditions described in section 4.4.3. During *inspill* we call them $TRIG_{raw}^{in}$, during *outspill* they are called $TRIG_{raw}^{out}$.

In order to get the true number of BGO events EV^{in} (EV^{out}) we have to correct $TRIG_{raw}^1$ with its dead-time $\tau = 1500$ ns.

This can be applied in this simple way when we trigger on all BGO signals BGO_{tot} (*inclusive trigger*).

If we take the *neutral trigger* (see Figure 4.8) we also have to correct for additional dead-times:

- First there is the probability that a veto signal overlaps a *neutral trigger*. The probability for that is

$$p_1 = 1 - e^{-\tau_{veto} \cdot VETO} \quad (7.10)$$

with $\tau_{veto} = 350$ ns and $VETO$ is the veto rate of all scintillators.

- In addition it can happen that a particle that should be vetoed (charged particle or muon) passes through the BGO and induces a signal with the length $\tau_{BGO} = 1500$ ns. These signals can also overlap with a photon/neutron induced signal in the BGO.

¹The following formulas are valid for *inspill* and *outspill*, hence the suffix *in* (*out*) can be skipped.

Since we always count the total number of BGO detector events/s BGO_{tot} , too, we can write for this overlapping probability

$$p_2 = 1 - e^{-\tau_{bgo} \cdot (BGO_{tot} - TRIG_{raw})} \quad (7.11)$$

with $\tau_{bgo} = 1500$ ns, BGO_{tot} is the total BGO rate and $TRIG_{raw}$ the *neutral trigger*.

Summarising, the probability to measure photons and neutrons (i.e. *neutral trigger*) is $1 - (p_1 + p_2)$, therefore we have to divide the *neutral trigger* rate by $1 - (p_1 + p_2)$ in order to obtain the true number of *neutral trigger*. Hence the real number of photons and neutrons/s $TRIG_{corr}$ is now

$$TRIG_{corr} = \frac{TRIG_{raw}}{1 - p_1 - p_2}. \quad (7.12)$$

Then the dead-time correction by $\tau_{BGO} = 1500$ ns can be applied. Since the measured rates are very low, we get the true number of events EV^{in} (EV^{out}) with the simplified formula

$$EV = TRIG_{corr} (1 + \tau_{BGO} TRIG_{corr}). \quad (7.13)$$

For the runs where the *inclusive trigger* is used we do not need to apply the corrections in equations (7.10) and (7.11). We therefore simply have

$$BGO_{tot} = TRIG_{raw} = TRIG_{corr} \quad (7.14)$$

and directly apply equation (7.13).

Events EV_{Ecut}^{in} (EV_{Ecut}^{out}) in Certain Energy Intervals

The computer is not fast enough to process all BGO signals during a measurement. Therefore the total number of events/s processed by the computer *inspill* (*outspill*) is $CompEV_{all}$. Energy thresholds can be set so that the number of events/s having passed these thresholds is $CompEV_{Ecut}$.

In order to get the BGO counts/s EV_{Ecut}^{in} (EV_{Ecut}^{out}) within a certain energy interval the corrected BGO counts/s EV^{in} (EV^{out}) have to be multiplied with the factor

$$EV_{Ecut} = \frac{CompEV_{Ecut}}{CompEV_{all}} EV. \quad (7.15)$$

7.2.2 Beam Flux

For the measurements with the collimator C8 opened the beam counts $BP_{C8\uparrow}$ are

$$BP_{C8\uparrow} = B1B2 - \langle B1B2offset \rangle \quad (7.16)$$

with $B1B2$ the counts of the scintillators B1B2 and $\langle B1B2offset \rangle$ the averaged offset values from Table 6.3 for each corresponding measurement run. $B1B2$ is corrected for dead time with $\tau_{B1B2} = 75$ ns.

During the measurements where C8 is closed the scintillators B1B2 can not count the beam flux, since the beam is already absorbed upstream in C8. However, from equation (7.4) we see that the contribution of the muon induced signals in the BGO also has to be normalised to the number of particles in the beam when C8 is open.

So for the C8 closed measurements we take the counts $Tr4$ of Tr4 and normalise these scintillator values to B1B2 with the factor $f_{Tr4toB1B2}$ from Table 6.4. $Tr4$ is dead-time corrected with $\tau_{Tr4} = 65$ ns. With this method we get for the beam flux $BP_{C8\downarrow}$

$$BP_{C8\downarrow} = (Tr4 - \langle T4offset \rangle) * f_{Tr4toB1B2}. \quad (7.17)$$

7.2.3 Summary

Summarising sections 7.2.1 and 7.2.2 allows us to describe equations (7.5) and (7.7) more precisely. We can write for the measured background rate R_{BP}^{Ecut} in a certain energy interval

$$R_{BP}^{Ecut} = R_{C8\uparrow}^{Ecut} - R_{C8\downarrow}^{Ecut} \quad (7.18)$$

with the signal rate measured when the collimator C8 open

$$R_{C8\uparrow}^{Ecut} = \frac{1}{\langle B1B2 - \langle T4offset \rangle \rangle} \left[\langle EV_{C8\uparrow}^{in} \rangle \frac{\langle CompEV_{Ecut}^{in} \rangle}{\langle CompEV_{all}^{in} \rangle} - \langle EV^{out} \rangle \frac{\langle CompEV_{Ecut}^{out} \rangle}{\langle CompEV_{all}^{out} \rangle} \right] \quad (7.19)$$

and with the signal rate measured with C8 closed

$$R_{C8\downarrow}^{Ecut} = \frac{1}{\langle T4 - \langle T4offset \rangle \rangle * f_{Tr4toB1}} \left[\langle EV_{C8\downarrow}^{in} \rangle \frac{\langle CompEV_{Ecut}^{in} \rangle}{\langle CompEV_{all}^{in} \rangle} - \langle EV^{out} \rangle \frac{\langle CompEV_{Ecut}^{out} \rangle}{\langle CompEV_{all}^{out} \rangle} \right]. \quad (7.20)$$

A measurement always lasts more than 100 SPS cycles. The dead time corrections and veto overlapping corrections are performed for each *inspill* (*outspill*) readout. The rate is then calculated with the averaged values per run.

7.3 Spectral Distribution

For each recorded event the energy is calculated based on the ADC information; The spectral distribution of the *inspill* and *outspill* measurements are obtained, respectively. In total $N \cdot \langle CompEV_{all}^{in} \rangle$ events/s are in the *inspill* histogram and *outspill* there are $N \cdot \langle CompEV_{all}^{out} \rangle$ events/s. N is the number of SPS cycles.

Independent of the measurement set-up we always obtain the absolute yield and energy for each run by weighting the *inspill* spectrum with the factor

$$w_{in} = \frac{1}{N \langle \text{Comp}EV_{all}^{in} \rangle} \frac{\langle EV^{in} \rangle}{\langle BP \rangle} \quad (7.21)$$

and the *outspill* spectrum with the factor

$$w_{out} = \frac{1}{N \langle \text{Comp}EV_{all}^{out} \rangle} \frac{\langle EV^{out} \rangle}{\langle BP \rangle}. \quad (7.22)$$

For the measurements with the collimator C8 opened $\langle BP \rangle$ is the average value calculated according to equation (7.16). For the runs with C8 closed $\langle BP \rangle$ is taken from equation (7.17). EV^{in} (EV^{out}) is calculated according to equation (7.13).

Subtracting the *outspill* histogram from the *inspill* yields the spectral distribution for a given measurement run.

Similar to equation (7.18) the final spectrum of the particle background is then the result of the subtraction of the C8 closed measurements from the C8 opened measurements.

Chapter 8

Discussion of Representative Measurements

8.1 Introduction

In order to get a better understanding of the various measurements some representative data are discussed in this chapter.

Especially the measurements *on beam-axis* and *off beam-axis* (see Figure 6.1) will be pointed out, since the characteristics of these measurements differ significantly.

The discrepancies between $p_{beam} = 40 \text{ GeV}/c$ and $p_{beam} = 120 \text{ GeV}/c$ and between 200 cm and 240 cm iron absorber lie mainly in the different rates but not in the origin of particles entering the BGO detector.

In the following discussions we will refer to the measurements with 240 cm iron, because this set-up approximates the ATLAS shielding most closely. In addition the most extreme situations are chosen: $p_{beam} = 120 \text{ GeV}/c$, *on beam-axis*, where we expect a high rate and $p_{beam} = 40 \text{ GeV}/c$, *off beam-axis*, where the rate is very low.

8.2 On Beam-Axis

8.2.1 Raw Data

Table 8.1 shows the data behind 240 cm iron, with $p_{beam} = 120 \text{ GeV}/c$ and the set-up *on beam-axis*. The results of the measurements with two different beam intensities as well as their corresponding C8 closed measurements are displayed.

The column *B1B2* shows the count rate of the beam scintillators B1B2 (Figure 4.4), *inclusive trigger* are the total counts in the BGO detector. The energy-cut is given by the discriminator threshold which is ≈ 250 keV.

In order to get the photon and neutron counts (*neutral trigger*) we applied the trigger-logic shown in Figure 4.8. For the muon and high energetic charged particle counts (*high-charged trigger*) we triggered according to Figure 4.9. A low energy charged particle (*low-charged trigger*) fulfils the trigger-logic shown in Figure 4.10.

The noise background counts (*outspill*) are already subtracted.

Table 8.1: Typical rates for measurements behind 240 cm iron, on beam-axis and $p_{beam} = 120$ GeV/c.

240 cm iron, 120 GeV/c beam, on beam-axis					
collimator C8	counts/s				
	<i>B1B2</i>	<i>inclusive trigger</i>	<i>neutral trigger</i>	<i>high-charged trigger</i>	<i>low-charged trigger</i>
low beam intensity					
open \uparrow	52500	1485	389	884	57
closed \downarrow	3032	741	262	393	20
high beam intensity					
open \uparrow	111500	2549	599	1466	116
closed \downarrow	3788	775	262	416	25

Table 8.1 gives the following information:

- We see that in this position the count rate of the *neutral trigger* is very low compared to the *high-charged trigger*. The explanation is as follows:

The high energy particle collisions occur close to the beam axis. In these interactions π^0 's are produced which decay into two γ 's that are the beginning of an electromagnetic shower. We therefore find many γ 's, electrons and positrons at later stages in the shower. In case such a shower process happens close to the BGO detector, very often more than one particle enter the BGO at the same time. This means we have a very high multi-event¹ rate *on beam-axis*. From the simulation we will learn that the average number of particles entering the BGO per beam particle is 2.6.

A photon is not counted when it is accompanied by a charged particle that induces a veto in one of the scintillators *ch*, $\mu 1$ or $\mu 2$. This results in measuring less photons than there actually are. Therefore the numbers in Table 8.1 underestimate the real photon and neutron rate. From the simulations we know that the true rates are approximately a factor 9 higher [Vin99].

The scintillators are very large compared to the BGO detector. Hence due to the high multi-event rate the probability is very high that all three scintillators together with

¹The multi-events are characterised in details in section 10.2.

the BGO detector get a signal induced by any of the multi-events. This condition fulfils the trigger-logic for muons and high energy particles and therefore the *high-charged trigger* rate is very high. In such a situation it is also obvious that this counting rate increases with higher beam intensity.

- The *low-charged trigger* rate is very low compared to the *neutral trigger* rate and the *high-charged trigger* rate.
- When C8 is closed, the counting rates of the different trigger-applications are approximately the same for the two different intensity runs. This shows that we only measure halo muon induced signals and not the signals induced by the shower particles reaching the iron absorber from the beam-dump in the collimator C8. (see error estimations in section 9.1.1).
- Since we never trigger on a coincidence between the BGO and only one of the muon scintillators, it is reasonable that the sum of *neutral trigger*, *high-charged trigger* and *low-charged trigger* is not equal the *inclusive trigger*.

8.2.2 Spectra

Figures 8.1 to 8.4 show the spectra of the low intensity measurements *on beam-axis*, behind 240 cm iron and with a beam momentum of $p_{beam} = 120 \text{ GeV}/c$ (The high intensity results show no difference).

Figure 8.1 displays the results of the *inclusive trigger*.

With C8 closed only halo muons are recorded. They either enter the BGO detector directly (muon peak) or induce showers in the iron where the photons hit the BGO.

The energy deposition of muons with momenta between $70 \text{ GeV}/c$ and $120 \text{ GeV}/c$ in the BGO detector is $\approx 70\text{-}90 \text{ MeV}$ [Loh85]. In Figure 8.1 we see the muon peak at $\approx 25 \text{ MeV}$ which shows that the energy response is not linear up to these energies. However, from section 6.2.1 we know that the calibration is linear up to the relevant energies of $\approx 9 \text{ MeV}$. The reason for the non-linearity lies in the photo-multiplier of the BGO-detector.

Naively one would expect that the muon peak is independent of the C8 setting. The difference in Figure 8.1 between the C8 open and C8 closed measurements can be explained by a pile-up of multi-events from showers at the end of the absorber.

The peak at 511 keV originates from $e^+ e^-$ -annihilation close to the BGO into two γ 's with one of them entering the BGO detector.

Figure 8.2 shows the final spectrum (C8 \uparrow -C8 \downarrow) up to the relevant energies. Several kinds of particles have contributed to this spectrum: First there are photons from (n, γ) and $(n, n' \gamma)$ reactions. Second we have photons originating from the electromagnetic shower processes, third there are neutrons from the hadronic shower processes and finally there are neutrals piled-up with other neutral or charged particles. The low energy charged particles rate is very low.

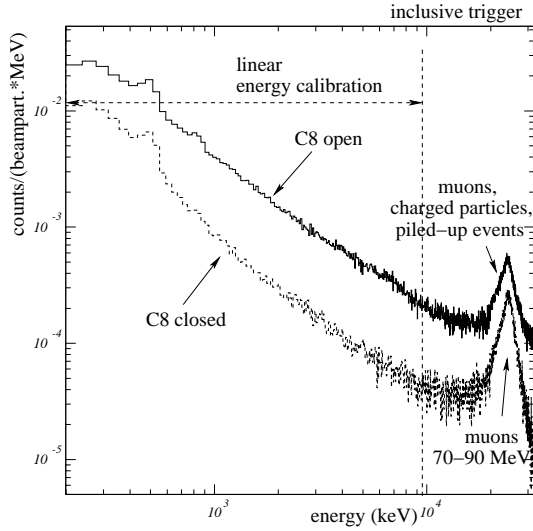


Figure 8.1: Spectra for C8 open and C8 closed behind 240 cm iron, on beam-axis, $p_{beam} = 120 \text{ GeV}/c$. Inclusive trigger is used.

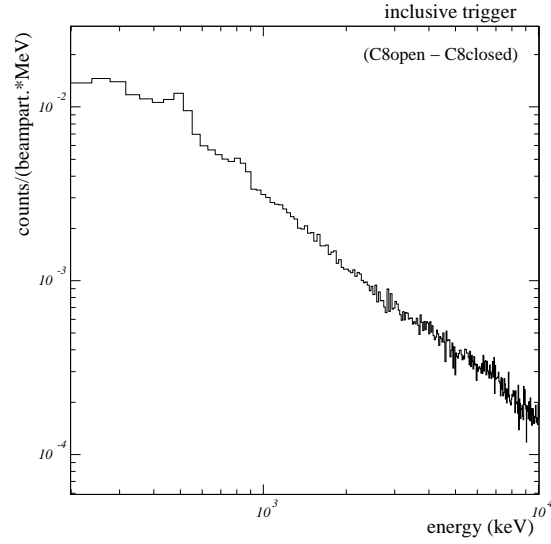


Figure 8.2: Spectrum induced by the beam particles ($C8\uparrow - C8\downarrow$).

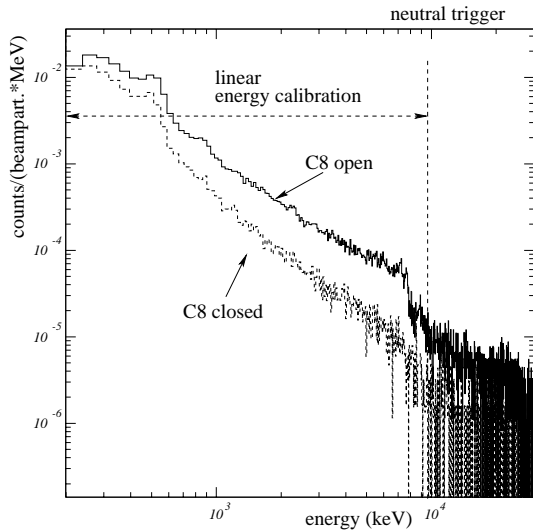


Figure 8.3: Spectra for C8 open and C8 closed behind 240 cm iron, on beam-axis, $p_{beam} = 120 \text{ GeV}/c$, recorded with the neutral trigger.

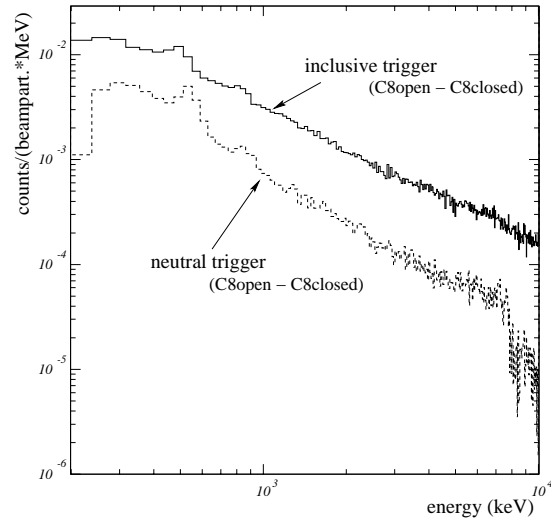


Figure 8.4: Comparison of the two spectra, taken with the inclusive trigger and neutral trigger.

Figure 8.3 shows the spectra taken with the *neutral trigger*. Muons and charged particles are vetoed but also the photons that are accompanied with a particle inducing a veto signal in one of the scintillators.

The big step at $E \approx 7.6$ MeV shows a photo peak and its single escape peak at ≈ 7.1 MeV originating from two typical (n, γ) reaction of thermal neutrons in iron already described in section 6.2.1. Similar reactions producing higher γ energies rarely appear in iron.

In Figure 8.4 the comparison of the final spectra recorded with the two different trigger conditions are shown. The difference between the spectra is large due to the high multi-event contributions which mask the photo peak at ≈ 7.6 MeV.

8.3 Off Beam-Axis

8.3.1 Raw Data

Table 8.2 summarises the data of the measurements with 240 cm iron absorber and with $p_{beam} = 40$ GeV/c. The BGO is ≈ 58 cm *off beam-axis*.

This measurement position is easier to analyse than the one *on beam-axis* since most of the photons are produced via (n, γ) or $(n, n' \gamma)$ interactions and there are rarely multi-events. Only ≈ 21 % of the photons originate from π^0 decays (as evaluated by the simulations).

Table 8.2: Typical rates for measurements behind 240 cm iron, *off beam-axis* and $p_{beam} = 40$ GeV/c.

240 cm iron, 40 GeV/c beam, <i>off beam-axis</i>					
collimator C8	counts/s				
	<i>B1B2</i>	<i>inclusive trigger</i>	<i>neutral trigger</i>	<i>high-charged trigger</i>	<i>low-charged trigger</i>
low beam intensity					
open \uparrow	1063000	830	580	168	25
closed \downarrow	8416	461	267	158	12
high beam intensity					
open \uparrow	2200000	1125	836	163	36
closed \downarrow	14770	448	249	161	12

From the measurements we find that:

- The rates in the BGO are typically at the level of 10^{-3} per beam particle.
- For the C8 open measurements the *high-charged trigger* rate does not change with different beam intensities. This can be explained by the fact that in this position

the multi-events are rare and hence random coincidences between multi-events do not fulfil the trigger-requirements for muons and high-energetic charged particles. In addition high energy charged particles and muons from the shower processes are also infrequent.

- The photons are rarely accompanied by charged particles which would result in photon vetoes.
- The *low-charged trigger* rate is very low.
- The data indicate that some of the shower particles from the closed collimator C8 can reach the iron absorber but that they are all absorbed in iron. This is demonstrated by the fact that the B1B2 counts are nearly linear with the beam intensity, whereas the BGO detector counts the same number of events.

8.3.2 Spectra

Figure 8.5 shows the spectrum measured with the *inclusive trigger* and the BGO detector *off beam-axis*, behind 240 cm iron, low intensity beam and $p_{beam} = 40 \text{ GeV}/c$. Overlaid is the spectrum measured with the collimator C8 closed.

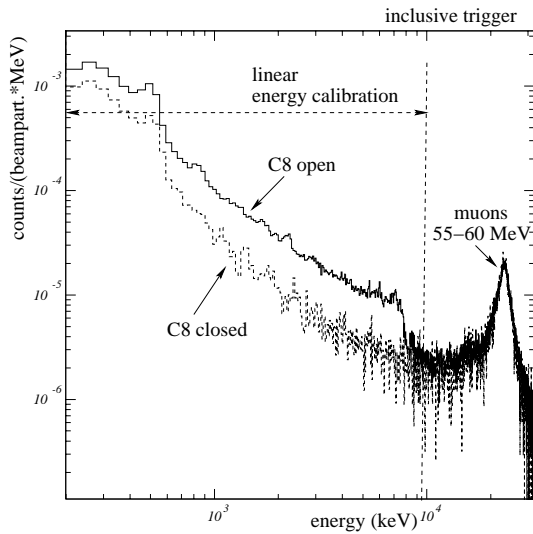


Figure 8.5: *Inclusive spectra for C8 open and C8 closed behind 240 cm iron, off beam-axis, $p_{beam} = 40 \text{ GeV}/c$.*

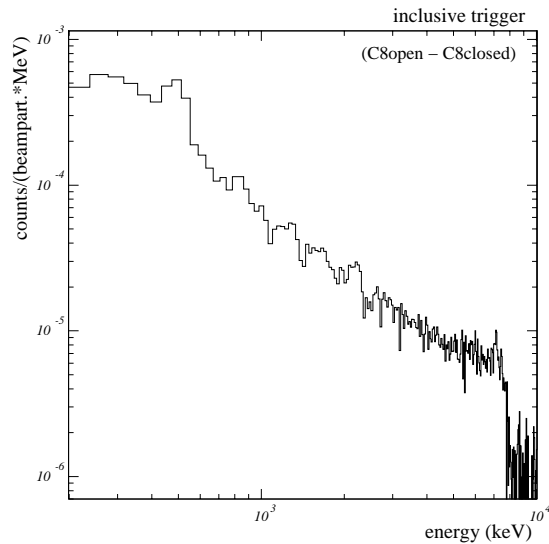


Figure 8.6: *Beam induced (C8↑-C8↓) inclusive spectrum.*

We see that the muon peaks coincide for both C8 settings. This indicates that all high energy charged particles hitting the BGO detector are halo muons (also see the *high-charged*

trigger rates in Table 8.2).

The energy loss of muons with a momentum between 20 GeV/c and 40 GeV/c is ≈ 50 -60 MeV which is about a factor 1.5 lower than for the measurements *on beam-axis* shown in Figure 8.1. However, the muon peak is at the same ADC bin position as expected due to the saturation of the photo-multiplier.

Subtracting the C8 closed spectrum from the C8 open spectrum yields the beam particle induced spectrum shown in Figure 8.6. Since at this measurement position the multi-event signals do not contribute significantly, the 7.6 MeV photo peak is seen very clearly.

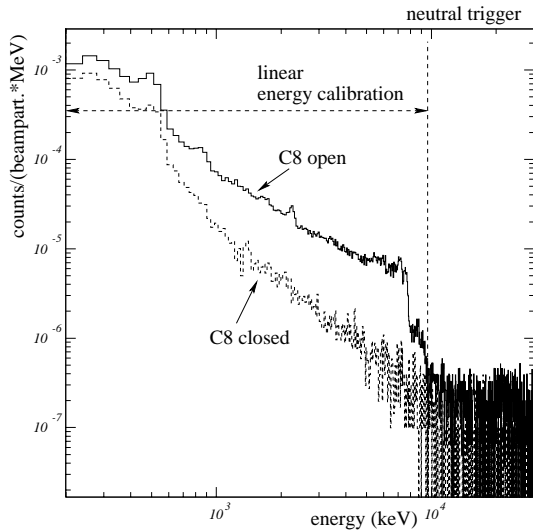


Figure 8.7: Spectra for C8 open and C8 closed behind 240 cm iron, off beam-axis, $p_{beam} = 40$ GeV/c, recorded with the neutral trigger.

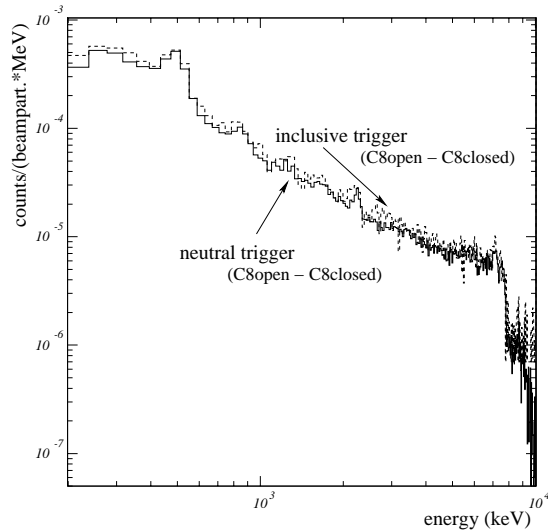


Figure 8.8: Comparison of the final spectra with the two trigger conditions.

Figure 8.7 shows the spectra of the measurements with the *neutral trigger*. All detected muons are vetoed.

In Figure 8.8 we compare the two spectra taken with the two different trigger conditions. The shape as well as the absolute yield of the spectra are very similar.

This indicates that at this measurement position we mostly observe photons and neutrons emanating from the final stages of the hadronic shower in the iron absorber, almost free of multi-events.

8.4 Summary

The two measurement positions *on beam-axis* and *off beam-axis* have very different characteristics.

At *on beam-axis* there are still electromagnetic shower processes close to the end of the iron absorber, which contribute to the high multi-event rate. While triggering on neutral particles underestimates the real photon and neutron rate, the measurements with the *inclusive trigger* show neutral particles piled-up with other particles entering at the same time the detector.

Nevertheless, it is possible to extract rates and spectra which are amenable to comparison with Monte Carlo estimates.

The measurement position *off beam-axis* provides a very clean experimental environment in terms of single neutral particle events. However, from the simulations we will learn that the neutron fluence contribution is about a factor 2 higher than the emanating photons which results in difficulties to extract the measured photon spectra *off beam-axis* (see section 11.4).

Chapter 9

Results of the Measurements

In this chapter a summary of the measured rates and spectra taken with the various measurement set-ups is given. In addition the different uncertainty contributions of the measurements are discussed.

9.1 Summary of the Measured Signal Rates

Table 9.1 provides a summary of all measurements recorded with the *neutral trigger*. The signal rates $R_{C8\uparrow}$ and $R_{C8\downarrow}$ normalised to the incident beam particles are calculated and corrected according to equations (7.19) and (7.20), respectively. The last columns show the final signal rates $R_{BP} = R_{C8\uparrow} - R_{C8\downarrow}$ and the rate $\langle R_{BP} \rangle$ which is the average between the two intensity results. The uncertainties are determined according to procedure explained in section 9.1.1.

Table 9.2 shows the results of the measurements taken with the *inclusive trigger*.

It is important to notice that the normalised signal rates for the different beam intensities are mostly within 1σ . This shows that all effects from residual activities, dead-time corrections and other effects of the set-up are understood and well under control.

Comparing the same measurement positions in the two tables shows that the *off beam-axis* results depend due to the low multi-event rate only marginally on the trigger conditions (as explained in the previous chapter).

Table 9.1: Summary of the normalised signal rates of the low and high intensity measurements recorded with the neutral trigger (see Figure 4.8).

measurement set-up	B1B2 beam intensity	signal rates $\times 10^{-4}$ ($0.35 \text{ MeV} < E < 9 \text{ MeV}$)			
		$R_{C8\uparrow}$	$R_{C8\downarrow}$	R_{BP}	$\langle R_{BP} \rangle$
$p_{beam} = 40 \text{ GeV}/c$					
200 cm <i>on beam-axis</i>	139 kHz	24.46 ± 0.19	6.99 ± 0.60	17.47 ± 0.63	16.80 ± 0.35
	419 kHz	18.90 ± 0.16	2.78 ± 0.24	16.12 ± 0.29	
200 cm <i>off beam-axis</i>	611 kHz	7.60 ± 0.08	1.96 ± 0.16	5.64 ± 0.18	5.71 ± 0.17
	2297 kHz	6.31 ± 0.30	0.54 ± 0.05	5.77 ± 0.30	
240 cm <i>on beam-axis</i>	238 kHz	10.10 ± 0.09	3.87 ± 0.38	6.23 ± 0.39	6.09 ± 0.22
	495 kHz	7.97 ± 0.08	2.03 ± 0.16	5.94 ± 0.18	
240 cm <i>off beam-axis</i>	1063 kHz	3.24 ± 0.06	1.10 ± 0.11	2.14 ± 0.13	2.08 ± 0.08
	2200 kHz	2.56 ± 0.07	0.55 ± 0.06	2.01 ± 0.09	
$p_{beam} = 120 \text{ GeV}/c$					
200 cm <i>off beam-axis</i>	326 kHz	25.19 ± 0.13	3.85 ± 0.27	21.34 ± 0.30	21.73 ± 0.26
	1066 kHz	23.34 ± 0.41	1.33 ± 0.09	22.12 ± 0.42	
240 cm <i>on beam-axis</i>	53 kHz	41.32 ± 0.34	19.21 ± 1.34	22.11 ± 1.38	21.66 ± 0.80
	112 kHz	32.40 ± 0.19	11.20 ± 0.80	21.20 ± 0.82	
240 cm <i>off beam-axis</i>	375 kHz	11.59 ± 0.08	3.29 ± 0.22	8.30 ± 0.23	8.35 ± 0.16
	1285 kHz	9.39 ± 0.20	0.99 ± 0.07	8.40 ± 0.21	

Table 9.2: Summary of the measurements taken with the inclusive trigger.

measurement set-up	B1B2 beam intensity	signal rates $\times 10^{-4}$ ($0.35 \text{ MeV} < E < 9 \text{ MeV}$)			
		$R_{C8\uparrow}$	$R_{C8\downarrow}$	R_{BP}	$\langle R_{BP} \rangle$
$p_{beam} = 40 \text{ GeV}/c$					
200 cm <i>on beam-axis</i>	139 kHz	93.27 ± 0.31	16.01 ± 0.11	77.26 ± 0.33	76.25 ± 0.40
	419 kHz	82.30 ± 0.52	7.07 ± 0.51	75.23 ± 0.73	
200 cm <i>off beam-axis</i>	611 kHz	9.57 ± 0.09	2.72 ± 0.24	6.85 ± 0.26	6.79 ± 0.21
	2297 kHz	7.56 ± 0.32	0.84 ± 0.09	6.72 ± 0.33	
240 cm <i>on beam-axis</i>	238 kHz	33.48 ± 0.14	10.50 ± 0.75	22.98 ± 0.76	23.00 ± 0.44
	495 kHz	28.84 ± 0.22	5.82 ± 0.39	23.02 ± 0.45	
240 cm <i>off beam-axis</i>	1063 kHz	4.02 ± 0.07	1.76 ± 0.16	2.26 ± 0.17	2.30 ± 0.11
	2200 kHz	3.20 ± 0.12	0.86 ± 0.09	2.34 ± 0.15	
$p_{beam} = 120 \text{ GeV}/c$					
200 cm <i>off beam-axis</i>	326 kHz	32.62 ± 0.17	6.32 ± 0.38	26.30 ± 0.42	26.30 ± 0.42
	1066 kHz	-	-	-	
240 cm <i>on beam-axis</i>	53 kHz	144.62 ± 0.53	51.68 ± 2.96	92.94 ± 3.00	93.48 ± 1.73
	112 kHz	124.89 ± 0.32	30.87 ± 1.68	94.02 ± 1.71	
240 cm <i>off beam-axis</i>	375 kHz	15.09 ± 0.95	5.25 ± 0.32	9.84 ± 1.00	9.86 ± 0.56
	1285 kHz	11.42 ± 0.25	1.54 ± 0.11	9.88 ± 0.27	

9.1.1 Contributions to the Uncertainty of the Measurements

9.1.1.1 Statistical Uncertainties

During each run we took data for more than 100 spills. This yields a statistical uncertainty of less than 0.2% for the measurements with the collimator C8 open. For the runs with C8 closed the uncertainty is less than 0.6%.

9.1.1.2 Systematic Uncertainties

The various factors in equations (7.19) and (7.20) contribute differently to the systematic uncertainty of the signal rate R_{BP}^{Ecut} . Since several uncertainty are correlated, a Monte Carlo program was developed in order to correctly consider the effects of these uncertainties. In this program each factor from equations (7.19) and (7.20) is drawn from a Gaussian distribution with a corresponding width (σ) representing the uncertainty of this parameter.

This method yields a distribution for the rates $R_{C8\uparrow}^{Ecut}$ and $R_{C8\downarrow}^{Ecut}$, their widths are taken as their systematic uncertainties.

We consider six main sources for the systematic uncertainties of the rate $RATE_{Ecut}$:

1. Energy Calibration

The energy calibration can cause uncertainties when the ADC has drifted or the BGO detector reacts to temperature-effects during a run. The calibration curve influences the number of events within a certain energy interval (see equation (7.15)).

In section 6.2.1 we compared the calibration curves that differ most and we have shown that the relative uncertainty between them is less than 3%. In addition we have seen that the rate difference is less than 0.01%.

We can hence neglect the contribution of the energy calibration curve to the uncertainty of the final rate.

2. Dead-Time Corrections

As described in sections 7.2.1 and 7.2.2 dead-time corrections have to be applied for the scaler readouts of the beam counters $B1B2$ and $Tr4$, all BGO counts and the veto signals. Although the widths of the discriminated signals were measured with the oscilloscope there are still uncertainties due to e.g. delays of the scaler etc.

We consider the following uncertainties for the dead-times:

$$\begin{aligned}\tau_{B1B2} &= 75 \text{ ns} \pm 15 \text{ ns} \\ \tau_{T4} &= 65 \text{ ns} \pm 5 \text{ ns} \\ \tau_{veto} &= 350 \text{ ns} \pm 70 \text{ ns} \\ \tau_{BGO} &= 1500 \text{ ns} \pm 50 \text{ ns}\end{aligned}$$

The dead-time corrections of the scintillator readouts $Tr4$ and $B1B2$ contribute most to the systematic uncertainty of the final background rate.

Figure 9.1 shows the distribution of the triggered BGO counts EV^{in} which are calculated according to the equations in section 7.2.1. We see that the width of the distribution is very small and hence the contribution to the uncertainty of the rate is estimated to be 0.2%.

3. Variations in the Natural Background

Repeated measurements at the same position show that the BGO counts during *outspill* vary within 4%.

Whereas we have for the *inspill* BGO data EV^{in} uncertainties caused by the dead-time corrections of the BGO signal and the veto signal, we need to add an uncertainty of 4% for the *outspill* BGO data EV^{out} .

Figure 9.2 shows the distribution for EV^{out} that corresponds to the *inspill* data in Figure 9.1. We see that the *outspill* signal rate is about 13% of the *inspill* data.

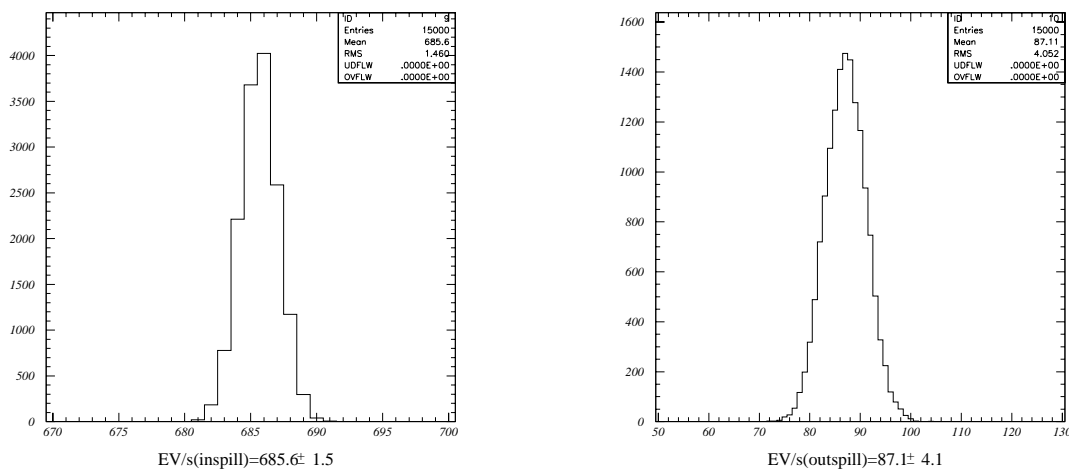


Figure 9.1: Monte Carlo estimation of the error of the BGO events EV^{in} .

Figure 9.2: Monte Carlo distribution of dead-time corrected BGO events EV^{out} . The width corresponds to the uncertainty. The natural background variation uncertainty of 4% is included.

4. Beam Counter Offset Values

In equations (7.16) and (7.17) we see that the offset values $\langle Tr4offset \rangle$ and $\langle B1B2offset \rangle$ have to be subtracted from the readings of the beam scintillators $Tr4$ and $B1B2$, respectively. These offset values are together with its uncertainties summarised in Table 6.3.

5. Normalisation Factor

For the measurement runs with the closed collimator C8 we have to consider the uncertainty of the normalisation factor $f_{Tr4toB1B2}$. The factor as well as the uncertainties are shown in Table 6.4.

6. Uncertainty of the Muon Induced Signals

As discussed in section 6.1 the muon induced signals $EV_{\mu_{ind}}$ are measured with the collimator C8 closed. With this method the beam is already absorbed in C8 and only the muons can pass through and induce signals in the BGO detector behind the iron absorber.

Nevertheless, it is important to find out whether the particles originating from the shower process in the collimator C8 can still reach the iron absorber, shower again and induce signals in the BGO detector. This would result in the fact that we have additional signals not even existing when we subtract the C8 closed measurements from the C8 open measurements ($R_{BP} = R_{C8\uparrow} - R_{C8\downarrow}$).

We therefore compared the C8 closed measurements of the same conditions (see measurement overview in section 6.1) but with different beam intensities. In addition we compared these measurements with the runs where the H6 magnets were switched off that means we have only particles from the neighbouring beam lines and from the Be-target T4.

We found that the counting rate of the scintillators B1B2 has an offset when the beam is switched off (see Table 6.3) and increases linearly with the beam intensity. This means that there are particles that reach the iron absorber (see also Tables 8.1 and 8.2).

However, the counting rate of the BGO detector stays constant within 5% for the different intensities and even when the beam is switched off. It indicates that firstly the C8 closed events are mainly induced by the halo particles we even see when the H6 magnets are switched off and secondly that the remaining shower particles from C8 are all absorbed in the iron block with an energy too low to induce signals in the BGO.

Hence within an uncertainty of 5% the BGO events $EV_{\mu_{ind}}$ are induced by the halo muons only.

9.1.1.3 Total Uncertainty

Figure 9.3 shows the Monte Carlo distribution of the signal rate $R_{C8\uparrow}^{Ecut}$ for the high intensity measurement run behind 240 cm iron, *on beam-axis*, with $p_{beam} = 40$ GeV/c beam momentum and triggering on photons and neutrons. The width of the distribution illustrates the uncertainty of the measured rate. Thus, we get $R_{C8\uparrow}^{Ecut} = (7.97 \pm 0.08) 10^{-4}$ cts/beam-particle.

In Figure 9.4 we see the results for the corresponding measurements with the collimator C8 closed. The signal rate is $R_{C8\downarrow}^{Ecut} = (2.03 \pm 0.16) 10^{-4}$ cts/beam-particle.

The final signal rate is then

$$R_{BP}^{Ecut} = R_{C8\uparrow}^{Ecut} - R_{C8\downarrow}^{Ecut} = (5.94 \pm 0.18) 10^{-4} \text{ cts/beam-particle.} \quad (9.1)$$

We find that the uncertainty for the C8 open measurements is for all different measurements between 0.3% and 5%. The uncertainty is dominated by the B1B2 dead-time correction.

For the C8 closed measurements the uncertainty is higher; It is between 5% and 11%. The uncertainty is mainly determined by the uncertainty in the muon induced signals and the normalisation factor for the scintillator Tr4.

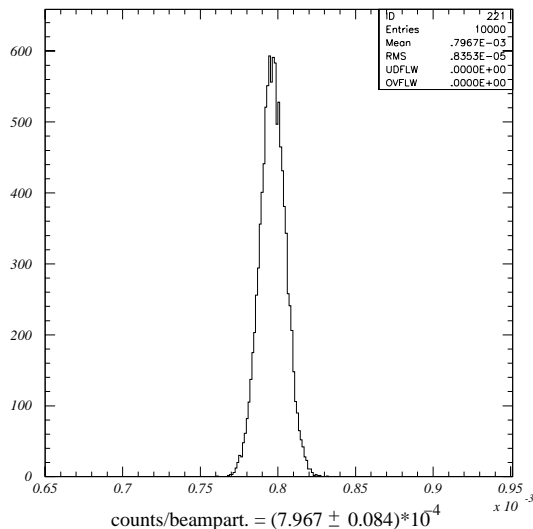


Figure 9.3: Monte Carlo distribution of $R_{C8\uparrow}^{Ecut}$ for the high intensity run behind 240 cm iron, on beam-axis, $p_{beam} = 40$ GeV/c and recorded with the neutral trigger.

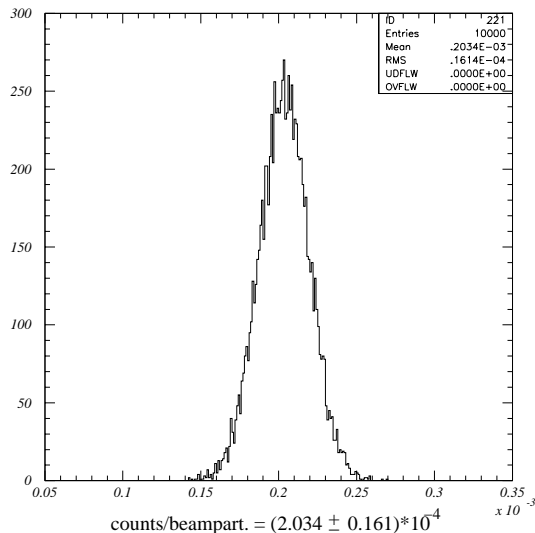


Figure 9.4: Monte Carlo distribution of the rate $R_{C8\downarrow}^{Ecut}$ for the corresponding measurement run where the collimator C8 is closed.

9.2 Summary of the Measured Spectra

In Figures 9.5 to 9.11 the spectral distribution of all different measurements are shown. In each Figure we see the spectra where the triggers are provided either by the BGO or only by neutral particles.

As already explained in section 8.2 the *on beam-axis* measurements have a large multi-event contribution. The probability that one of the multi-events induces a veto signal in the scintillators, although only photons enter the BGO, is very high. Therefore applying the

neutral trigger does not only veto muons and charged particles but also photons. When the *inclusive trigger* is taken there are also multi-event signals in the spectrum where neutral particles are piled-up with neutral and charged particles.

At *off beam-axis* the multi-event situation is much better and hence the data sets taken under different trigger conditions give nearly the same results.

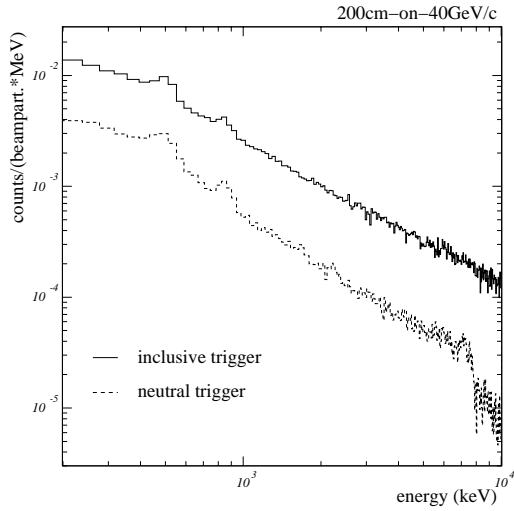


Figure 9.5: Final spectra behind 200 cm iron absorber, on beam-axis, $p_{beam} = 40 \text{ GeV}/c$.

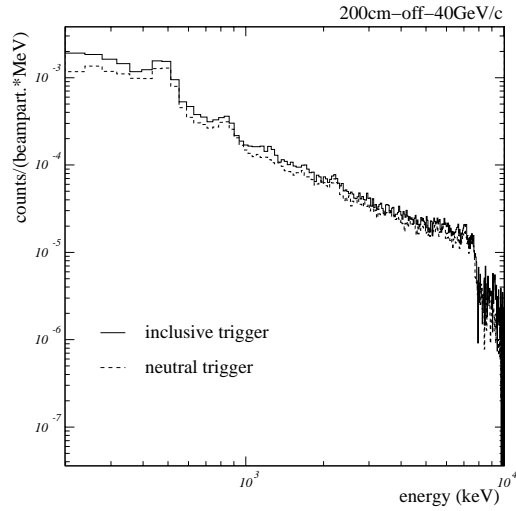


Figure 9.6: Final spectra behind 200 cm iron absorber, off beam-axis, $p_{beam} = 40 \text{ GeV}/c$.

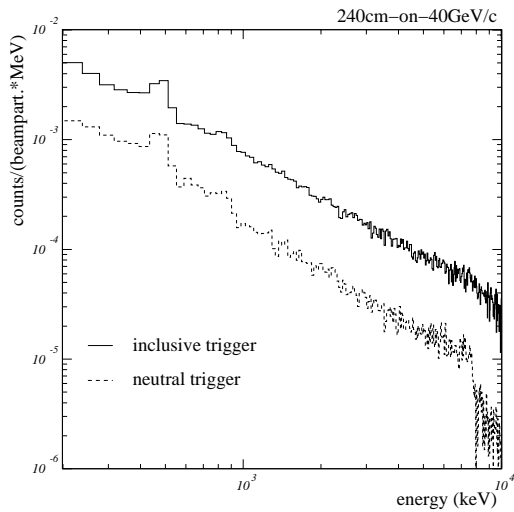


Figure 9.7: Final spectra behind 240 cm iron absorber, on beam-axis, $p_{beam} = 40 \text{ GeV}/c$.

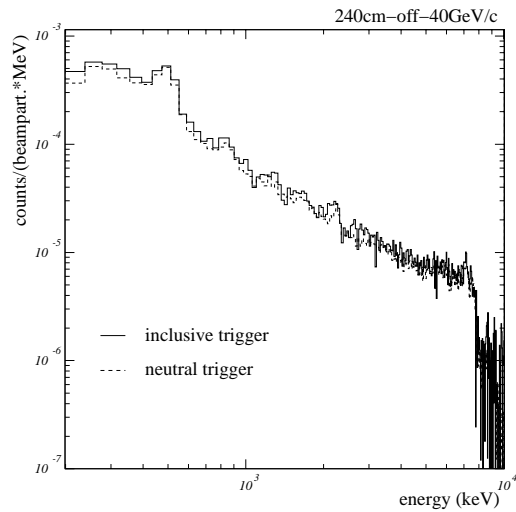


Figure 9.8: Final spectra behind 240 cm iron absorber, off beam-axis, $p_{beam} = 40 \text{ GeV}/c$.

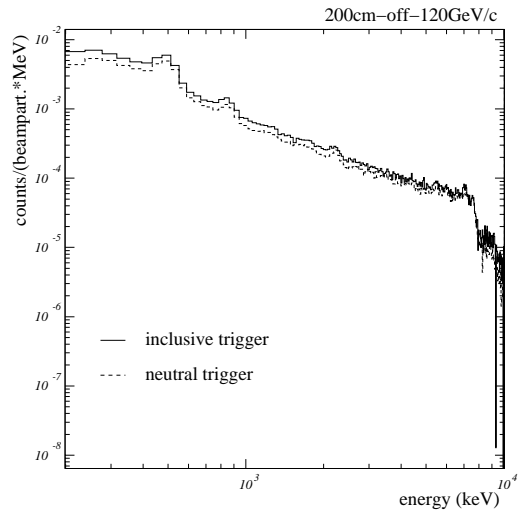


Figure 9.9: Final spectra behind 200 cm iron, off beam-axis, $p_{beam} = 120 \text{ GeV}/c$.

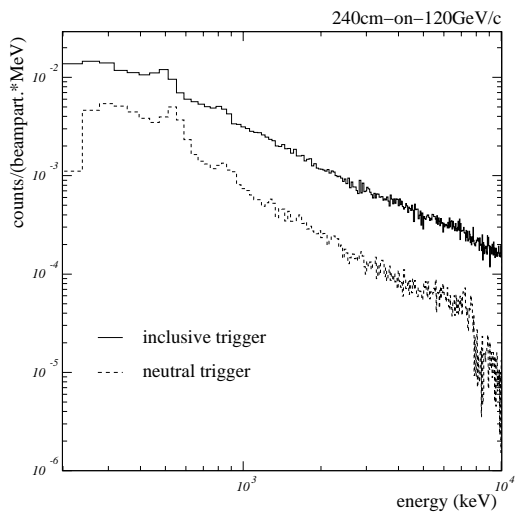


Figure 9.10: Final spectra behind 240 cm iron absorber, on beam-axis, $p_{beam} = 120 \text{ GeV}/c$.

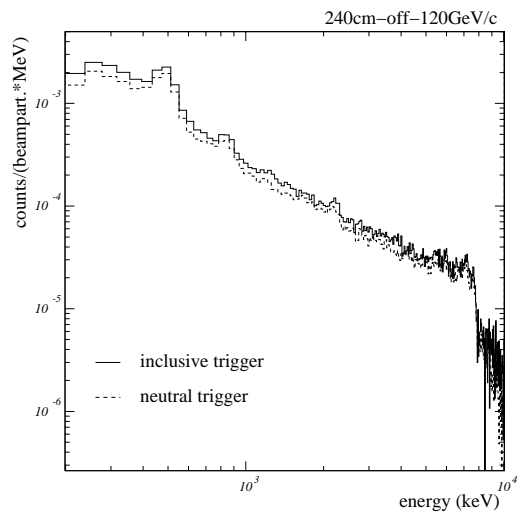


Figure 9.11: Final spectra behind 240 cm iron absorber, off beam-axis, $p_{beam} = 120 \text{ GeV}/c$.

Chapter 10

Simulation of the Background Benchmarking

10.1 Overview of the Simulation Procedure

In the simulation the geometry of the set-up consisting of the detectors and the iron absorber as well as the detector supports and the shielding materials around the beam line were considered very accurately. The geometry is already shown in Figure 4.2.

The simulated beam particles are described in Table 1. The shape of the beam was taken from the measurements shown in Figure 6.6. The vertical beam distribution is $\sigma=2.83$ mm and the horizontal distribution is $\sigma=3.67$ mm.

The simulation is performed in three steps:

1. The shower processes induced by the beam particles are simulated. Information about particles hitting the BGO are written to a file. This file contains details concerning position, flight direction, energy, statistical weight and informations concerning the origin of the single particle.
2. These data files are taken as input for the simulation of the energy deposition processes in the BGO detector.
3. The obtained BGO energy deposition spectrum is converted into a real BGO spectrum by smearing it with the energy resolution of the BGO response.

In the following these steps are explained in more detail.

Shower Processes in the Iron Absorber

The shower processes can be simulated with two different methods:

- **'analog'** simulation method:

This procedure is a full simulation where every particle is tracked through the entire iron absorber. With this method all particles originating from the same beam particle are simulated in a way that correlations between the particles can be taken into account.

- **'biased'** simulation method:

In order to speed up the calculations and obtain enough statistics, regions can be defined with different statistical importances. The particles entering these regions are treated according to the region importance.

For the H6 simulations a cone inside the absorber was implemented. The tip is at the side where the beam enters the iron and the axis is drawn from the tip up to the position of the BGO. The cone is cut in several slices where each slice has a different biasing importance. The importance increases the closer the slices are to the BGO. In order to prevent weight fluctuations of the particles that will enter the BGO, 'weight windows'¹ are implemented at necessary positions.

The biasing method, however, loses the information about the correlations between the produced particles and hence e.g. each particle of the multi-events induces separate signals.

On Beam-Axis

On beam-axis analog simulation runs were performed in order to yield the particles entering the BGO detector.

The reason is that very close to the beam-axis late hadronic shower processes occur that produce among other particles also π^0 's. These π^0 's decay instantly into two high energetic γ 's that induce an electromagnetic shower in the iron. In order to calculate the energy deposition in the detector correctly all shower particles originating from the same beam particle hitting the BGO have to be simulated at the same time.

Figure 10.1 shows an example of a late electromagnetic shower induced by a π^0 decay *on beam-axis*.

Off Beam-Axis

Off beam-axis analog runs were also performed. However, we saw already in the measurement results when comparing the results with different trigger conditions (see Figure 8.8)

¹Region, energy and particle dependent weight windows are used to control the particle statistical weight at collision sites in order to accelerate convergence of the results [Fas99].

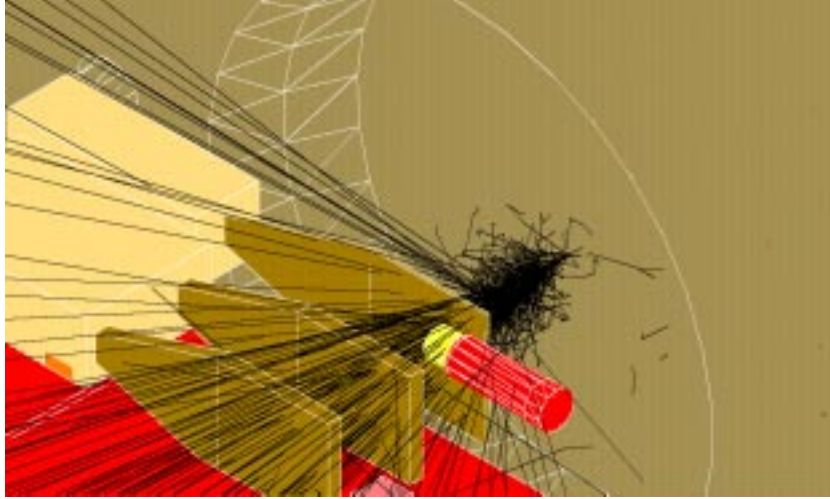


Figure 10.1: *Electromagnetic shower induced by a hadronic interaction with a following π^0 decay. 20 cm of the iron wall are removed to show the beginning of the shower.*

that the multi-event rate is very low. In addition the counting rate in the BGO detector at the *off beam-axis* position is very small and it is difficult to obtain enough statistics for a proper spectrum. Hence also biased runs with sophisticated biasing techniques were carried out.

Energy Deposition in the BGO

The output of the first simulation step is used in the second step. It simulates the energy deposition in the BGO. We have to distinguish between the particles produced with an analog run and particles originating from a biased simulation run:

- In case the first simulation run was an analog one, particles originating from the same beam particle have to be considered together for the next simulation run. This procedure guarantees that all particles originating from the same beam particle produce only one entry in the spectrum.
- In case of a biased first run the different statistical weights of the particles have to be considered. A particle with a certain weight has to be converted into a corresponding number of particles of weight 1.0 in order to perform the second run in a fully analog mode. The final rate per beam particle is then the induced count rate divided by the number of beam particles and by the factor obtained from the particle weight conversion.

Folding the BGO Energy Deposition with the BGO response

The energy deposition obtained in the second run corresponds to a measured spectrum with infinitively good energy resolution. In order to adapt the results to the real BGO detector with its electronic instrumentation the energy deposition is convoluted with the BGO response. The procedure is explained in detail in section 5.2.4.1.

10.2 Characterisation of the Experimental Set-Up

Fluences behind the Iron Shielding

Figure 10.2 shows the results of the simulation of the different particle fluences behind 240 cm iron induced by a beam with a momentum $p_{beam} = 40 \text{ GeV}/c$. Close to the beam-axis the photon fluence is much higher than the neutron fluence. With increasing distance from the beam-axis the neutron fluence decreases very slowly. *Off beam-axis* (distance $\approx 58 \text{ cm}$) the neutron fluence is ≈ 2 times higher than the photon fluence, while at *on beam-axis* the ratio is $\approx 1/2$.

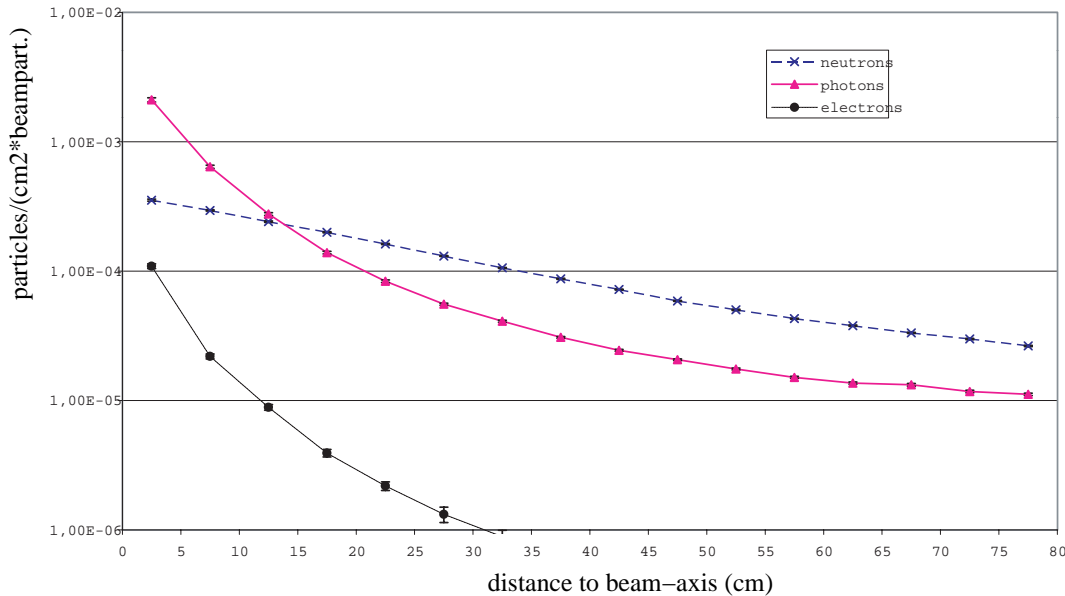


Figure 10.2: Particle fluences behind 240 cm iron and with $p_{beam} = 40 \text{ GeV}/c$.

The high photon fluence close to the beam-axis is due to the high energy particle collisions where π^0 's are produced that decay into two γ 's. These γ 's initiate an electromagnetic shower.

Since the high energetic particles are mainly produced *on beam-axis*, the π^0 production decreases with increasing distance from the beam-axis.

Origin of the Emanating Particles

Table 10.2 shows the hadronic origin of the photons entering the BGO behind 240 cm iron induced by a beam with $p_{beam} = 40 \text{ GeV}/c$.

Table 10.1: *Hadronic origin of the photons behind 200 cm and with $p_{beam} = 40 \text{ GeV}/c$.*

mother particle	<i>on beam-axis</i> [%]	<i>off beam-axis</i> [%]
n	12.2	72.0
π^0	68.6	21.3
π^+	5.0	1.8
π^-	3.4	0.9
p	0.8	0.3
μ^+	8.3	2.1
K^+	0.5	0.3
others	1.2	1.3

We see that at *on beam-axis* $\approx 70\%$ of the photons originate from π^0 decays. The remaining $\approx 30\%$ are produced via (n, γ) reactions or other inelastic hadronic interactions.

Off beam-axis most of the photons are produced via (n, γ) or $(n, n' \gamma)$ reactions. Only 21% of the photons come from π^0 decays. In addition this measurement position is quite far from the beam-axis so that only one photon produced by this electromagnetic shower reaches the BGO.

The hadronic origin of neutrons is similar in both situations. Neutrons behind the iron absorber are mainly produced by other neutrons.

Classification of the Events

Events originating from the same beam particle enter the BGO detector at the same time. The number of particles entering the BGO per beam particle behind 240 cm iron and $p_{beam} = 40 \text{ GeV}/c$ are shown in Figures 10.3 and 10.4.

On beam-axis only 64.8% of the events are single particles. The average number of particles hitting the BGO detector per beam particle is 2.6.

The situation *off beam-axis* is simpler. There are mainly single particle events (95%). The average number of particles entering the BGO per event is 1.05. This fact and the low reaction probability of the particles in the BGO justifies a biased shower calculation at the *off beam-axis* position.

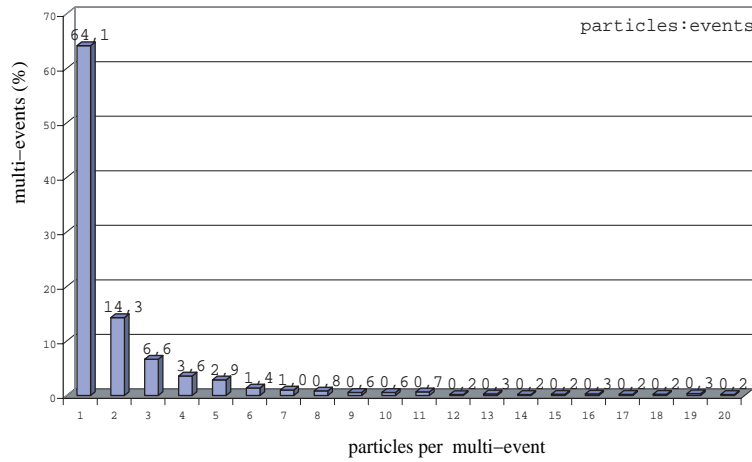


Figure 10.3: Classification of the multi-events behind 240 cm iron, on beam-axis and with $p_{beam} = 40$ GeV/c.

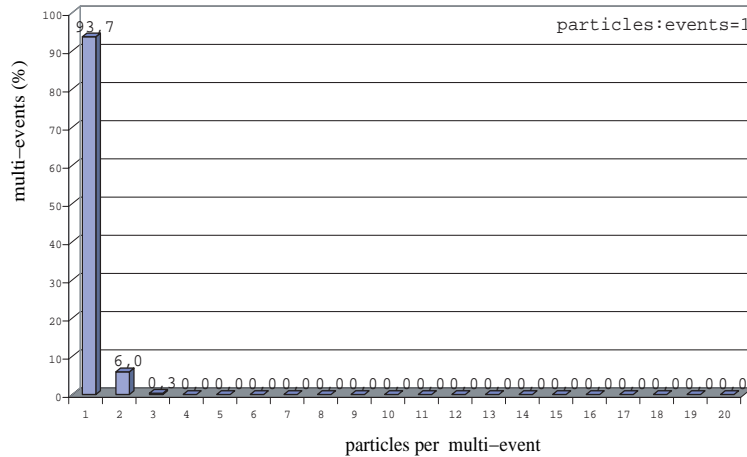


Figure 10.4: Multi-events off beam-axis behind 240 cm iron and with $p_{beam} = 40$ GeV/c.

10.3 Results

The simulated signal rates and spectra will be shown in the next chapter where we compare the measurements with the simulations.

Uncertainties associated with the Simulation

The statistical uncertainty in the simulations *off beam-axis* is between 4% and 11%. *On beam-axis* the statistics is better and hence we have an uncertainty between 1.5% and 3%. The uncertainties of the total rate, evaluated with the simulations, consist of the following contributions:

- The distance between the beam-axis and the BGO detector is known with an uncertainty of 1 cm. Depending on the BGO position this yields an uncertainty of $\sim 2.4\%$ (*off beam-axis*) to $\sim 17\%$ (*on beam-axis*).
- The carbon content in the iron absorber is about 5 weight-%. However, this is variable within one weight-% and gives an uncertainty contribution between 1% to 14%.
- The ratio between $\frac{K^+}{p}$ and $\frac{\pi^+}{p}$ in the hadron beam is known within 3%. This results in an uncertainty contribution of 0.3%.
- Uncertainties in the size of the BGO detector ($38\text{ mm} \pm 0.1\text{ mm}$) result in an uncertainty contribution of 0.8%.
- The uncertainty in the measurements of the thickness of the iron absorber ($1\sigma = 3\text{ mm}$) can be estimated to contribute with 1.1%.
- The absorber density can vary within $(7.2 \pm 0.036)\text{ g/cm}^3$. This adds an uncertainty of up to 5% to the rate.
- The distance from the BGO to the iron absorber is known within 1 mm. This uncertainty contributes with 2.2% to the final uncertainty.

A detailed description of the uncertainty contributions can be found in [Vin00b].

Chapter 11

Comparison of the Measurements with the Simulations

11.1 Introduction

As shown in chapter 8 we used different trigger conditions in the measurements in order to distinguish between charged and neutral particles. Since the trigger scintillators were read out with an ADC, it is also possible to apply these trigger-logics afterwards in the analysis.

Using these triggers to distinguish particles is however not easy, since there are many multi-events where one of these multi-events can initiate a veto in the scintillators although only photons enter the BGO detector. This results in recording less photons than there actually are.

In order to compare the simulations with the measurements where only neutral particles have provided the trigger (*neutral trigger*), one also has to simulate the charge deposit of the vetoing particles in the scintillators and calibrate the simulated threshold of the scintillators in the measurements. Although this procedure was used for cross-checks, this method adds a lot of uncertainties.

Hence it was found to be much more useful to simulate all particles entering the BGO detector and compare it to the runs where the *inclusive trigger* was taken. The measured photon rates and spectra can then be evaluated by subtracting the simulated neutron and multi-event results from the total measured one.

In the following sections the comparison between the total rates is shown. Subsequently, the results for the simulated and measured spectra will be displayed. Finally the method to yield the photon rates and spectra as well as their level of agreement will be shown.

11.2 Measured and Simulated Signal Rates

Table 11.1 shows the summary of the total measured and simulated signal rates in the energy interval $0.35 \text{ MeV} < E < 9 \text{ MeV}$ and normalised to the incident beam particles.

The measured rates are the averages of the two intensity runs per measurement position (see also Table 9.2). The uncertainty is calculated according to section 9.1.1.

All simulations for the rate were performed in the analog mode. The simulated uncertainties include the statistical one as well as the uncertainties described in section 10.3.

An illustration of the results is shown in Figure 11.1.

Table 11.1: Summary of measured and simulated signal rates in the energy interval $0.35 \text{ MeV} < E < 9 \text{ MeV}$ normalised to the incident beam particles.

measurement set-up	signal rate $\times 10^{-4}$		ratio
	measured	simulated	meas/sim
$p_{\text{beam}} = 40 \text{ GeV}/c$			
200 cm <i>on beam-axis</i>	76.2 ± 0.4	$71.8^{+6.7}_{-14.9}$	$1.06^{+0.10}_{-0.22}$
200 cm <i>off beam-axis</i>	6.8 ± 0.2	$6.1^{+0.8}_{-0.7}$	$1.12^{+0.14}_{-0.13}$
240 cm <i>on beam-axis</i>	23.0 ± 0.4	$15.8^{+2.7}_{-3.6}$	$1.46^{+0.25}_{-0.33}$
240 cm <i>off beam-axis</i>	2.3 ± 0.1	$1.9^{+0.3}_{-0.2}$	$1.24^{+0.19}_{-0.15}$
$p_{\text{beam}} = 120 \text{ GeV}/c$			
200 cm <i>off beam-axis</i>	26.3 ± 0.4	$26.0^{+3.0}_{-2.9}$	$1.01^{+0.12}_{-0.12}$
240 cm <i>on beam-axis</i>	93.5 ± 1.7	$78.6^{+9.6}_{-11.1}$	$1.19^{+0.15}_{-0.17}$
240 cm <i>off beam-axis</i>	9.7 ± 0.6	$7.8^{+1.4}_{-1.3}$	$1.24^{+0.24}_{-0.21}$
weighted average			1.13 ± 0.06

From the comparison we can conclude:

- The measurements and the simulations agree very well. We see that most of the rates agree at a 20% level. The weighted average yields a ratio of 1.13 ± 0.06 .
- For the results behind 200 cm iron all simulations are within 1σ of the measurements. Behind 240 cm the simulations are within 2σ .
- The largest uncertainties are due to the imperfect knowledge of the BGO position and the carbon content in iron.
- The asymmetry in the uncertainties is mainly due to the uncertainties in the BGO position.
- The uncertainties for the large absorber (240 cm) are worse due to less statistics in the simulations.

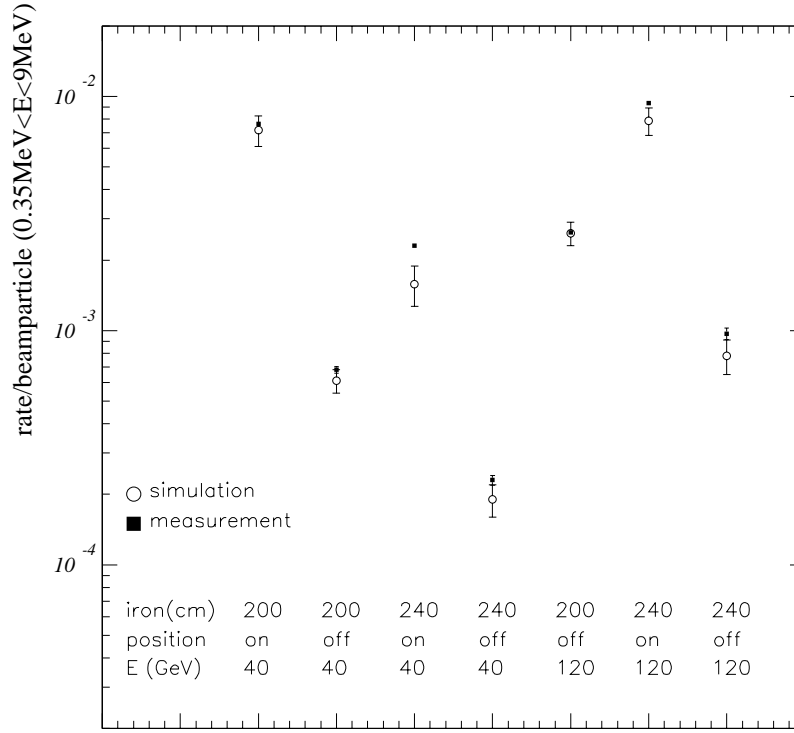


Figure 11.1: Measured and simulated signal rates in the energy interval $0.35 \text{ MeV} < E < 9 \text{ MeV}$.

11.3 Measured and Simulated Spectra

After comparing the absolute signal rates in the energy interval from $0.35 \text{ MeV} < E < 9 \text{ MeV}$ we want to compare the measured and simulated spectra. In the following sections the spectra for all different measurement conditions are shown.

In order to determine the spectra also quantitatively we calculate the average energy deposition $\langle E_{dep} \rangle$ in this energy range with

$$\langle E_{dep} \rangle = \frac{\sum_{i=Ebin_{min}}^{Ebin_{max}} R_i \cdot E_i}{\sum_{i=Ebin_{min}}^{Ebin_{max}} R_i} \quad \text{and} \quad R = \sum_{i=Ebin_{min}}^{Ebin_{max}} R_i \quad (11.1)$$

where R_i is the normalised signal rate in the energy bin i , E_i is the energy of the bin i and R is the total rate in the energy interval (see Table 11.1).

The uncertainty on the energy deposition is smaller than the uncertainty on the rate since

systematic uncertainties from dead-time corrections, imperfect BGO position knowledge etc. have no influence on the shape of the spectra.

Therefore we use only the rate uncertainty $\Delta R'$ that influence the shape of the spectra. Since they are mainly of statistical nature we distribute them to the individual bins as Poisson errors and find for the uncertainty on the average energy deposition

$$\Delta\langle E_{dep} \rangle = \frac{\Delta R'}{R} \cdot \sqrt{R \cdot (\langle E_{dep}^2 \rangle - \langle E_{dep} \rangle^2)} \quad (11.2)$$

where $\frac{\Delta R'}{R}$ is $\approx 1\%$ for the measurements and $\approx 10\%$ for the simulations.

11.3.1 On Beam-Axis

Figure 11.2 shows the simulation of the different contributions to the total spectrum behind 200 cm iron, *on beam-axis* and with $p_{beam} = 40$ GeV/c.

The different contributions are the counts of pure γ events (including γ multi-events), events induced only by neutrons and mixed multi-events¹. We see that the strongest influence on the counting rate is caused by the γ events followed by the mixed multi-events. In the mixed multi-events photons are very often accompanied by neutrons. Since the probability that neutrons interact with the BGO detector is about four times lower than for photons (see efficiency calculations for photons and neutrons in sections 5.2.3.2 and 5.3.3.4), the counts induced by mixed multi-events are dominated by photon interactions. We can find that also in the similarities of the multi-event and photon spectra shape.

In addition the photon fluence is more than 2 times higher than the neutron fluence at the measurement position *on beam-axis* (see Figure 10.2) resulting in a pure neutron contribution of $\approx 10\%$ to the total counting rate.

The neutron induced counts add strong peaks to the entire spectrum in the simulation. However, these peaks are not of physical nature, but FLUKA specific, since the simulated energy deposition of a neutron is the average of all possible energy depositions in the BGO.

Figure 11.3 shows the comparison between the measured and simulated spectra at this position. The peak at 511 keV originating from a pair-production close to the BGO, where one annihilating photon enters the BGO, is reproduced correctly. The peak at e.g. ≈ 800 keV in the measurements coming from a $(n, n'\gamma)$ interaction in the BGO is not simulated.

Nevertheless, the average energy deposition is for both spectra the same.

In Figure 11.4 we see the comparison for the position behind 240 cm iron and with $p_{beam} = 40$ GeV/c. The simulated spectrum is uniformly lower than the measured one resulting also in energy depositions with 5% difference.

Figure 11.5 shows the comparison for the measurement position behind 240 cm iron and with $p_{beam} = 120$ GeV/c. Also in this position the averaged energy deposition is the same for both spectra.

¹The mixed multi-events exclude the multi-events with only photons and the multi-events consisting of only neutrons.

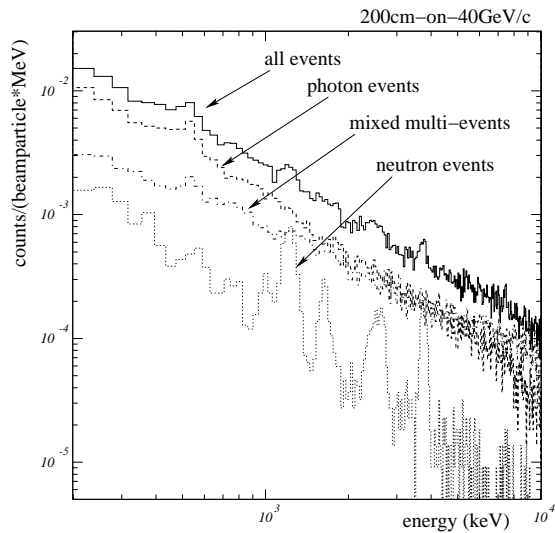


Figure 11.2: Different particle contributions in the simulation at the position behind 200 cm iron, on beam-axis and $p_{beam} = 40 \text{ GeV}/c$.

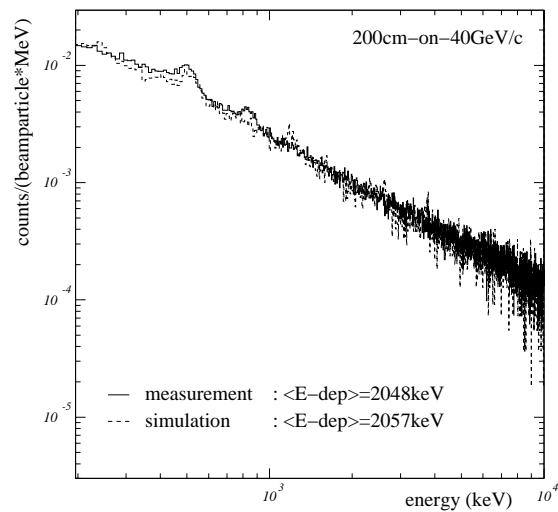


Figure 11.3: Measured and simulated total spectra behind 200 cm iron, on beam-axis and $p_{beam} = 40 \text{ GeV}/c$.

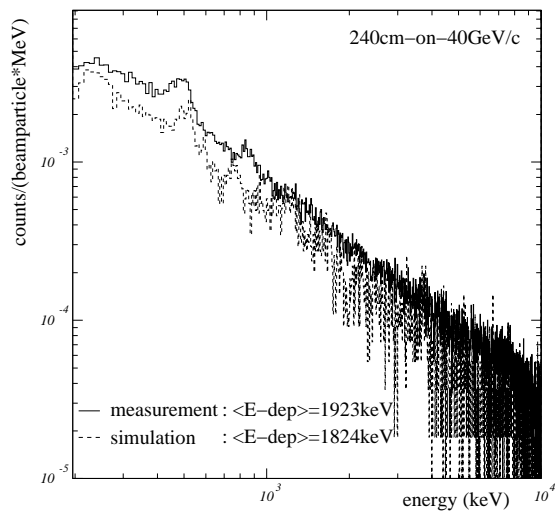


Figure 11.4: Measured and simulated total spectra behind 240 cm iron, on beam-axis and $p_{beam} = 40 \text{ GeV}/c$.

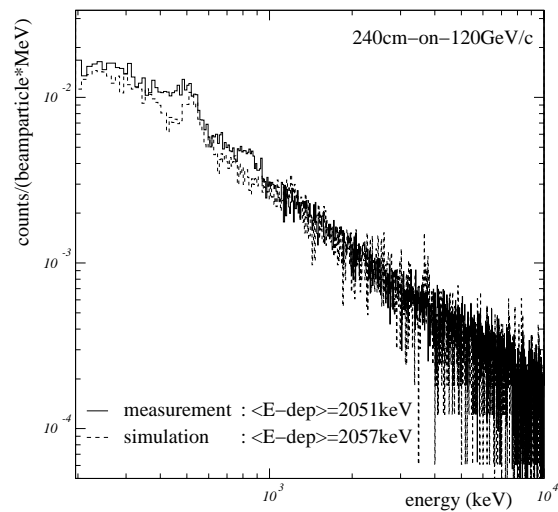


Figure 11.5: Measured and simulated total spectra behind 240 cm iron, on beam-axis and $p_{beam} = 120 \text{ GeV}/c$.

We can conclude that for all different positions the absolute rates as well as the shape agree very well. The average energy deposition shown in Table 11.2 is for all different situations better than 5%. This shows that the complicated particle situation *on beam-axis* with all the multi-events is very well understood.

Table 11.2: Summary of the averaged measured and simulated energy deposition *on beam-axis* in the energy interval $0.35 \text{ MeV} < E < 9 \text{ MeV}$.

measurement set-up	$\langle E\text{-deposition} \rangle$ [MeV]		ratio meas/sim
	measured	simulated	
$p_{beam} = 40 \text{ GeV}/c$			
200 cm <i>on beam-axis</i>	2.045 ± 0.018	2.057 ± 0.174	0.996 ± 0.085
240 cm <i>on beam-axis</i>	1.923 ± 0.009	1.824 ± 0.073	1.055 ± 0.042
$p_{beam} = 120 \text{ GeV}/c$			
240 cm <i>on beam-axis</i>	2.051 ± 0.020	2.058 ± 0.183	0.997 ± 0.089

11.3.2 Off Beam-Axis

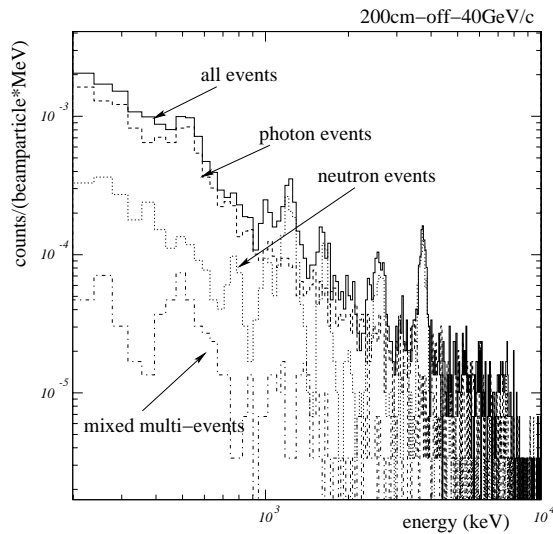


Figure 11.6: Simulated particle contributions behind 200 cm iron, *off beam-axis* and $p_{beam} = 40 \text{ GeV}/c$.

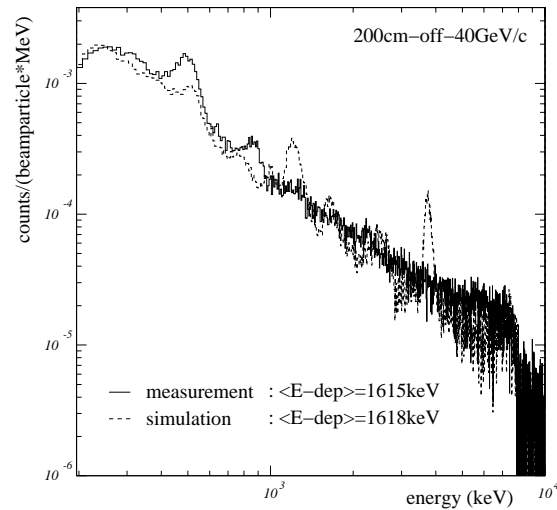


Figure 11.7: Measured and simulated total spectra behind 200 cm iron, *off beam-axis* and $p_{beam} = 40 \text{ GeV}/c$.

Figure 11.6 shows the simulated spectrum behind 200 cm iron, *off beam-axis* induced by $p_{beam} = 40 \text{ GeV}/c$. Overlaid are the different contributions to the spectrum. About 2 times more neutrons than photons enter the BGO detector which results in a

much higher neutron contribution to the total spectrum. Around 30% of the counts are caused by pure neutron events. Hence the FLUKA specific neutron induced peaks are very dominant in this situation.

From Figure 10.4 we know that the average number of particles entering the BGO per event is only 1.05. Due to this fact the multi-event contribution is very low.

Figure 11.7 shows the comparison between the measured and simulated spectra at this position.

Figures 11.8 and 11.9 show the results for the measurement positions behind 240 cm iron and a beam momentum of $p_{beam} = 40 \text{ GeV}/c$ and $p_{beam} = 120 \text{ GeV}/c$, respectively.

In Figure 11.10 we see the results behind 200 cm iron and with $p_{beam} = 120 \text{ GeV}/c$.

The (n,γ) reactions at $\approx 7.6 \text{ MeV}$ are reproduced very well in the simulations resulting in the same 'edge'-behaviour at $E > 7.6 \text{ MeV}$.

Since the neutron contribution is very high *off beam-axis*, the simulated neutron peaks are very dominant in all spectra. These FLUKA specific neutron peaks are of course not seen in the measurements. Nevertheless, the average energy deposition agrees around 10% for the different set-ups *off beam-axis* (see Table 11.3) what is expected, given that FLUKA simulates neutrons on average correctly. This and the fact that the integrated rates agree very well shows that the number of interactions in the BGO is simulated correctly.

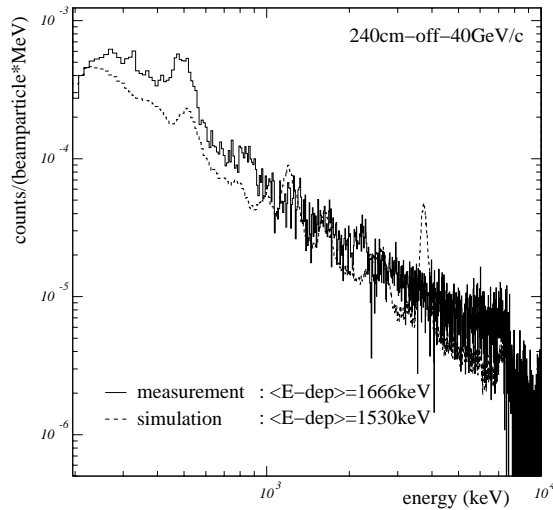


Figure 11.8: Measured and simulated total spectra behind 240 cm iron, *off beam-axis* and $p_{beam} = 40 \text{ GeV}/c$.

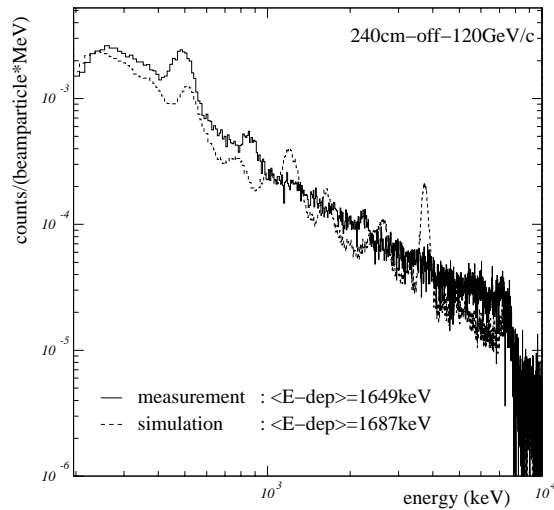


Figure 11.9: Measured and simulated total spectra behind 240 cm iron, *off beam-axis* and $p_{beam} = 120 \text{ GeV}/c$.

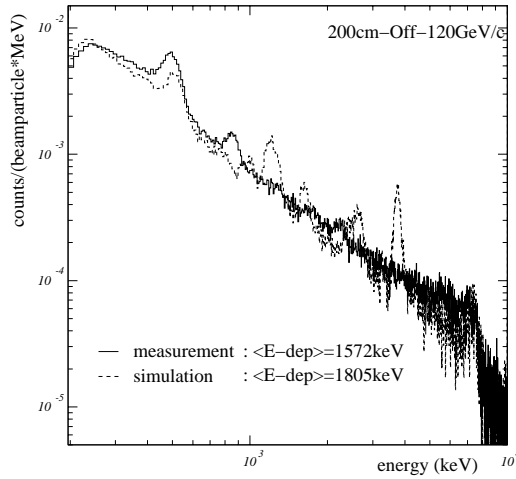


Figure 11.10: Measured and simulated total spectra behind 200 cm iron, off beam-axis and $p_{beam} = 120 \text{ GeV}/c$.

Table 11.3: Summary of the averaged measured and simulated energy deposition off beam-axis in the energy interval $0.35 \text{ MeV} < E < 9 \text{ MeV}$.

measurement set-up	$\langle E\text{-deposition} \rangle$ [MeV]		ratio meas/sim
	measured	simulated	
$p_{beam} = 40 \text{ GeV}/c$			
200 cm <i>off beam-axis</i>	1.615 ± 0.004	1.618 ± 0.041	0.997 ± 0.025
240 cm <i>off beam-axis</i>	1.666 ± 0.003	1.530 ± 0.021	1.089 ± 0.015
$p_{beam} = 120 \text{ GeV}/c$			
200 cm <i>off beam-axis</i>	1.572 ± 0.009	1.805 ± 0.091	0.871 ± 0.044
240 cm <i>off beam-axis</i>	1.649 ± 0.006	1.687 ± 0.051	0.978 ± 0.030

11.4 Evaluation of the Measured Photon Rates and Spectra

In section 11.2 we have shown that the comparison between the measured and simulated signal rates agree on average at the 20% level. We have also illustrated the comparison of the spectra in section 11.3 and shown that the general shape of the spectra as well as the average energy deposition agrees very well.

These results allow us to evaluate the measured photon rates and spectra by subtracting the simulated neutron and multi-event contributions.

Although we know that the simulation of the neutron energy deposition in the BGO de-

ector is only done in an averaged way we can estimate the uncertainty of the simulated neutron and multi-event contributions using the information of the Am-Be measurements (see section 5.3).

11.4.1 Photon Rates

In Table 5.5 we have shown that the measured and simulated Am-Be neutron rates agree within less than 30 % for an energy cut above 400 keV.

Hence we conservatively assume an uncertainty of 30 % for the simulated neutron rate:

$$\sigma_n = \text{neutron-error} \times \text{neutron-rate} \quad \text{with} \quad \text{neutron-error} = 0.3. \quad (11.3)$$

where σ_n is the uncertainty of the neutron contribution (not to mix with the neutron cross-section). The uncertainty of the multi-event contribution can be calculated as follows [Gsc00c]: The probability for photons to interact in the BGO is at least four times higher than for neutrons. In addition we know from the simulations that in the *on beam-axis* position only ≈ 75 % of the mixed multi-events contain neutrons. In the *off beam-axis* position we conservatively assume that 90 % of the mixed multi-events have neutrons.

Hence the uncertainty contribution of the neutrons in the mixed multi-events depends on the neutron uncertainty, the contents of neutrons in the mixed multi-events and the ratio of the interacting probabilities of photons and neutrons. With this method we get with *neutron-error* = 0.3 for the multi-event error *on beam-axis*

$$\sigma_{\text{multievents}}^{\text{on}} = \text{neutron-error} \times 0.75 \times 0.25 \times \text{multi-event-rate}. \quad (11.4)$$

For the *off beam-axis* measurements we get

$$\sigma_{\text{multievents}}^{\text{off}} = \text{neutron-error} \times 0.90 \times 0.25 \times \text{multi-event-rate}. \quad (11.5)$$

Table 11.4 shows the measured and simulated photon signal rates normalised to the incident beam particles. In order to be consistent with the neutron rate uncertainty estimations of the Am-Be-source, the rate is calculated between the energy interval $0.4 \text{ MeV} < E < 9 \text{ MeV}$.

The uncertainty of the simulated photon rate includes the statistical one as well as the uncertainties described in section 10.3.

The measured photon rate is the total measured rate minus the simulated neutron and multi-event contributions. The uncertainties of the neutron and multi-events are hence considered in the measured uncertainty. This is also the reason for the the asymmetry of the uncertainties.

We see that the measured and simulated photon rates agree very well. The weighted average gives a ratio of 1.25 ± 0.10 . Except for the measurement *on beam-axis*, behind 240 cm iron with $p_{\text{beam}} = 40 \text{ GeV}/c$, all simulations are within 2σ of the measurements.

Table 11.4: Summary of measured and simulated photon signal rates in energy interval $0.4 \text{ MeV} < E < 9 \text{ MeV}$ and normalised to the incident beam particles.

measurement set-up	γ -signal rate $\times 10^{-4}$		ratio
	measured	simulated	meas/sim
$p_{beam} = 40 \text{ GeV}/c$			
200 cm <i>on beam-axis</i>	$41.1^{+3.6}_{-6.7}$	$35.9^{+3.3}_{-7.5}$	$1.15^{+0.15}_{-0.30}$
200 cm <i>off beam-axis</i>	$4.1^{+0.6}_{-0.6}$	$3.5^{+0.4}_{-0.4}$	$1.17^{+0.23}_{-0.21}$
240 cm <i>on beam-axis</i>	$15.8^{+1.2}_{-1.4}$	$8.0^{+1.4}_{-1.8}$	$1.96^{+0.36}_{-0.48}$
240 cm <i>off beam-axis</i>	$1.4^{+0.2}_{-0.2}$	$1.0^{+0.2}_{-0.1}$	$1.40^{+0.30}_{-0.26}$
$p_{beam} = 120 \text{ GeV}/c$			
200 cm <i>off beam-axis</i>	$14.33^{+2.6}_{-2.6}$	$13.9^{+1.6}_{-1.6}$	$1.03^{+0.22}_{-0.22}$
240 cm <i>on beam-axis</i>	$48.3^{+5.8}_{-6.5}$	$35.1^{+4.3}_{-4.9}$	$1.38^{+0.24}_{-0.27}$
240 cm <i>off beam-axis</i>	$6.1^{+1.2}_{-1.1}$	$5.0^{+0.9}_{-0.8}$	$1.22^{+0.32}_{-0.30}$
weighted average			1.25 ± 0.10

11.4.2 Photon Spectra

We have estimated the uncertainty of the simulated neutron spectrum by comparing the measured and simulated Am-Be spectra. Figure 5.16 shows the uncertainty where we calculated an average uncertainty of $\sigma = 52.5\%$ in the energy range $400 \text{ keV} < E < 1000 \text{ keV}$. The average uncertainty for $1000 \text{ keV} < E < 3500 \text{ keV}$ is $\sigma = 18\%$ which we conservatively extend for energies up to 9 MeV.

Hence the uncertainties for the simulated neutrons and multi-event spectra are calculated according to equations (11.3), (11.4) and (11.5), respectively, with *neutron-error*=52.5% for energies up to 1000 keV and with *neutron-error*=18% for energies higher than 1000 keV.

The results for the situations behind 200 cm iron and $p_{beam} = 40 \text{ GeV}/c$ are shown, since only there the statistic is good enough to subtract the different contributions.

Figure 11.11 shows the total measured spectrum and overlaid the simulated neutron and multi-event spectra in the *on beam-axis* position. We see that compared to the multi-event contribution the neutron contribution is very low.

In Figure 11.12 we find the resulting measured and simulated photon spectra.

The peak in the measured spectrum at $\approx 800 \text{ keV}$ originates from $(n, n'\gamma)$ reactions not reproduced in the simulations. The 'negative' peak at $\approx 1050 \text{ keV}$ originates from a simulated averaged neutron peak. The annihilation peak at 511 keV is higher in the measurements.

However, we see that the average energy deposition for the measurements $\langle E\text{-dep} \rangle_{meas} = (1.77 \pm 0.13) \text{ MeV}$ and for the simulation $\langle E\text{-dep} \rangle_{sim} = (1.72 \pm 0.11) \text{ MeV}$ agree very well. The calculated uncertainty of the measured photon counts at the position $E \approx 511 \text{ keV}$ as well as at $E \approx 1100 \text{ keV}$ is shown with the two horizontal error bars that define the $\pm 1\sigma$ uncertainty region.

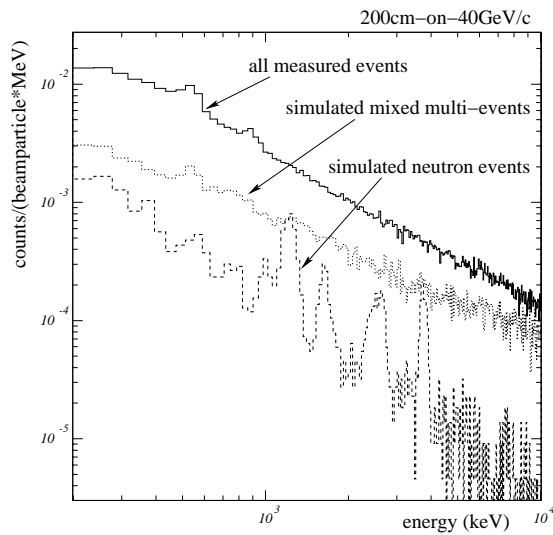


Figure 11.11: Total measured spectrum and simulated neutron and multi-event spectra behind 200 cm iron, on beam-axis and $p_{beam} = 40$ GeV/c.

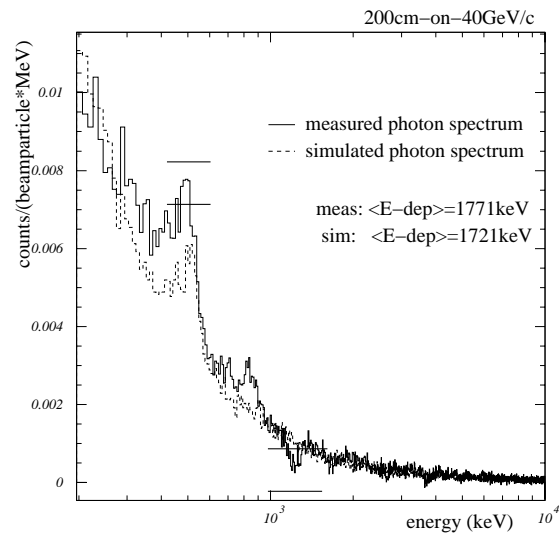


Figure 11.12: Measured and simulated photon spectra behind 200 cm iron, on beam-axis and $p_{beam} = 40$ GeV/c. The simulated neutron and multi-event contribution is subtracted from the total measured spectrum.

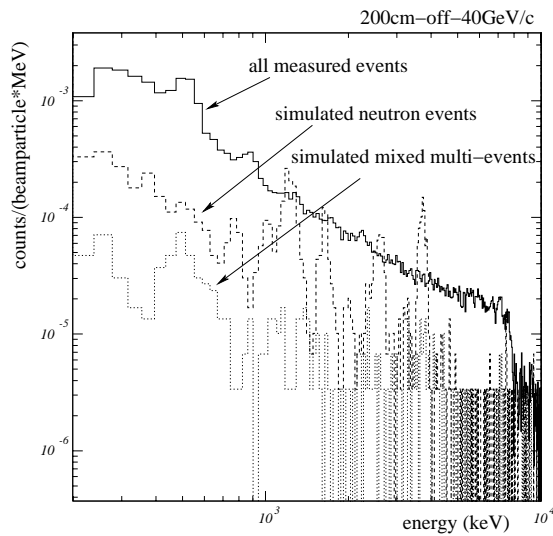


Figure 11.13: Total measured spectrum and simulated neutron and multi-event spectra behind 200 cm iron, off beam-axis and $p_{beam} = 40$ GeV/c.

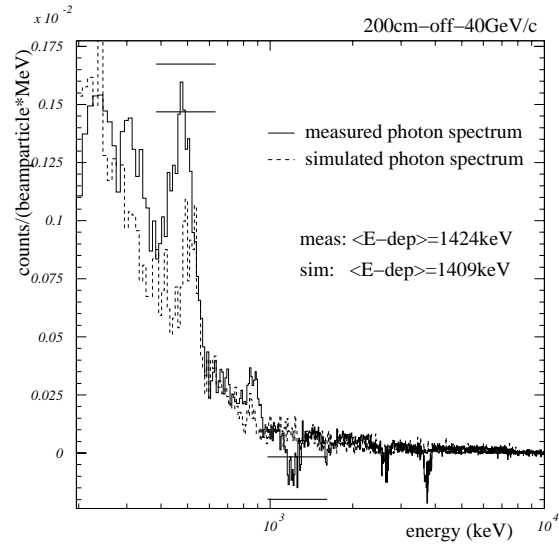


Figure 11.14: Measured and simulated photon spectra behind 200 cm iron, off beam-axis and $p_{beam} = 40$ GeV/c.

The neutron contribution at the *off beam-axis* position is very high. This is illustrated in Figure 11.13 where the total measured spectrum as well as the simulated neutron and multi-event spectra are shown. The multi-event contribution is nearly negligible.

The high neutron contribution results in strong 'negative' peaks in the final measured photon spectrum shown in Figure 11.14. Nevertheless, the average energy depositions of the measured spectrum is $\langle E\text{-dep} \rangle_{meas} = (1.42 \pm 0.03) \text{ MeV}$. The simulated photon spectrum has an average energy deposition of $\langle E\text{-dep} \rangle_{sim} = (1.41 \pm 0.02) \text{ MeV}$!

Also here the calculated uncertainty of the measured photon counts at the position $E \approx 511 \text{ keV}$ and at $E \approx 1100 \text{ keV}$ is shown with the two horizontal error bars.

11.5 Summary

The total measured and simulated normalised signal rates show very good agreement at the level of 20 % for most of the measurement positions. The weighted average yields a ratio between the measured and simulated signal rate, which is normalised to the incident beam particles, of

$$\frac{\text{signal rate}|_{meas}}{\text{signal rate}|_{sim}} = 1.13 \pm 0.06. \quad (11.6)$$

In the comparison between the total measured and simulated spectra *on beam-axis* we see that the shape agree very well. In addition the average energy deposition show an agreement better than 5 %. Hence we can conclude that the complicated particle situation *on beam-axis* with all the multi-events is well understood.

Due to the fact that *off beam-axis* the neutron contribution is very high and that the simulation of the neutron energy deposition is only done in an averaged way, the simulated total spectra have FLUKA specific peaks not seen in the measurements. However, the fact that for both the simulations and the measurements the average energy deposition agrees better than 10 % shows that the number of interactions in the BGO is simulated correctly.

In order to evaluate the measured photon rates and spectra the simulated neutron and multi-event contributions are subtracted from the total measured results. The induced uncertainties are estimated with the information of the Am-Be measurements in section 5.3.

We see that the measured and simulated photon rates agree very well. The weighted average gives a ratio of 1.25 ± 0.10 .

Although the subtraction of the simulated neutron spectra introduces local 'negative' peaks in the measured photon spectra, the average energy deposition agrees at the 2 % level.

Chapter 12

Relating the H6 Experimental Set-Up to the ATLAS Shielding

In this thesis we have shown that the simulation of the background behind the absorber of up to 14λ thickness agrees very well with the measurements. This experimental set-up approximates closely the ATLAS situation.

We can further substantiate the similarities between ATLAS and H6 by estimating the ATLAS background with the results of the measurements. Therefore a very simple model was developed to calculate the ATLAS photon background at a pseudorapidity¹ of $\eta = 2.7$.

12.1 ATLAS Photon Background Predicted with the H6 Results

Figure 12.1 shows a sketch of this model. The average transverse momentum of charged particles in minimum bias events at $\sqrt{s} = 14$ TeV is estimated to be $\langle p_T \rangle = 0.46$ GeV/c [Atc96] and hence at $\eta = 2.7$ we have on average a momentum of $p = 3.4$ GeV/c.

From the benchmarking measurements with $p_{beam} = 40$ GeV/c and $p_{beam} = 120$ GeV/c beam momenta we have shown that the measured and simulated results agree very well. We can therefore assume that the simulated fluences behind 14λ of iron absorber and induced by particles with $p_{beam} = 5, 10, 20$ GeV/c, respectively agree with the measurements, too.

Figure 12.2 shows the radial distribution of the photon fluences/particle induced by $p_{beam} = 5$ GeV/c.

We can calculate now for all different momenta the radii from the beam-axis containing 90 %

¹The pseudorapidity η relates to the polar angle (θ) with $\eta = -\ln(\tan \theta)$ where θ is the angle from the z -direction (along the beam line).

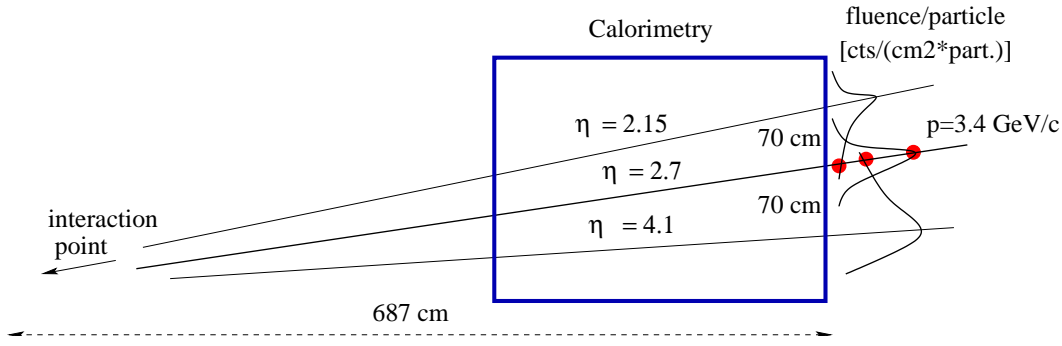


Figure 12.1: Sketch of the background estimation for ATLAS using the results of H6.

of the photons. Extrapolating these results to $p = 3.4 \text{ GeV}/c$ yields the radius $r = 70 \text{ cm}$. Hence in order to calculate the rate at $\eta = 2.7$ we take all contributions in a circle with radius $r = 70 \text{ cm}$ into account. This circle defines a region between $2.15 < \eta < 4.1$.

All particles that enter the absorber under the rapidity $2.15 < \eta < 4.1$ induce a fluence/particle at $\eta = 2.7$. A certain η corresponds to a certain momentum p . Hence we have to calculate for each momentum the radial distribution and find the induced fluence/particle at $\eta = 2.7$. We assume that in this small η -range the shape of the radial distribution does not vary and is similar to the curve for $p = 5 \text{ GeV}/c$.

Figure 12.3 shows this fluence/particle. Due to the fact that the momentum increases with higher η , the contributions are not symmetric around $\eta = 2.7$ but they are higher for the particles hitting the absorber at $\eta > 2.7$.

To yield the fluence rate at $\eta = 2.7$ the fluence/particle has to be multiplied with the number of particles/s.

The average charged particle multiplicity for simulated minimum bias events per unit of rapidity [Atc96] is

$$\frac{dN}{d\eta} = 7.47. \quad (12.1)$$

In order to consider also the neutral particles such as K^0 's and neutrons the multiplicity 7.47 was multiplied with 1.15. The inelastic proton-proton cross-section is assumed to be 80 mb and hence we have $8 \cdot 10^8$ inelastic p-p collisions/s. Therefore the particles rate per unit of rapidity is $7.47 \times 1.15 \times 8 \cdot 10^8 \text{ s}^{-1}$.

With this information and considering a geometry factor $F_{geometry}$, representing the area $dA/d\eta$ in the circle with $r = 70 \text{ cm}$, we can finally calculate the photon fluence rate γ -fluence-rate_{ATLAS} at $\eta = 2.7$ with

$$\int_{\eta=2.15}^{\eta=4.1} \frac{dN}{d\eta} \cdot 1.15 \cdot 8 \cdot 10^8 \cdot F_{geometry} \cdot fluence(\eta)_{\eta_0=2.7} \cdot F_{threshold} \cdot d\eta = 7.3 \text{ kHz}/\text{cm}^2 \quad (12.2)$$

with $F_{threshold} = 1.1$, a factor to consider the different thresholds in H6 (100 keV) and ATLAS (30 keV).

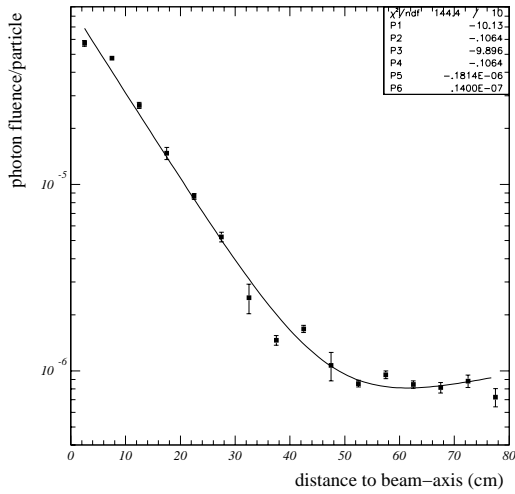


Figure 12.2: Simulated radial distribution of the photon fluence/particle behind 14λ and induced by $p = 5 \text{ GeV}/c$.

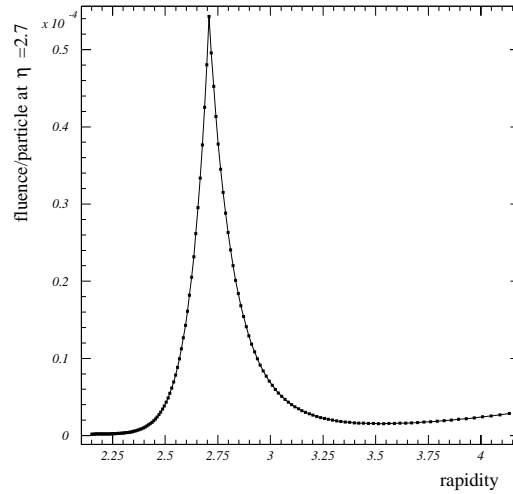


Figure 12.3: Fluence/particle at $\eta = 2.7$ induced by the particles entering the absorber in the region between $2.15 < \eta < 4.1$.

12.2 Comparison with ATLAS Calculations

In the background calculations for ATLAS done with FLUKA, the entire geometry as well as the particle variety were considered [Bat94a]. These complete calculations give a MDT counting rate of $0.21 \text{ kHz}/\text{cm}^2$ at $\eta = 2.7$. In order to get the photon fluence rate we have to consider the MDT γ -sensitivity $8 \cdot 10^{-3}$ (see Table 2.1) yielding a rate of $26.3 \text{ kHz}/\text{cm}^2$ at $\eta = 2.7$.

However, this rate can not be directly compared with the photon fluence rate calculated with the H6 results, since several effects add to the rate in ATLAS not considered in the simple H6 model [Fer00]:

- 25% of the calculated ATLAS rate originates from (n, γ) reactions in the ATLAS-hall wall not taken into account in the H6 model.
- In Figure 12.4 we see that behind the calorimeter there is heavy 'streaming' from the beam-pipe. From the colour code we find that this streaming increases the photon rate by 2-3 intervals corresponding to a factor of $\approx 3-6$.
- In ATLAS the material in front of the muon system at $\eta = 2.7$ is 14.5λ . In H6 the absorber thickness is 14λ . The differences in the absorber thicknesses introduces a rate difference of 22%.

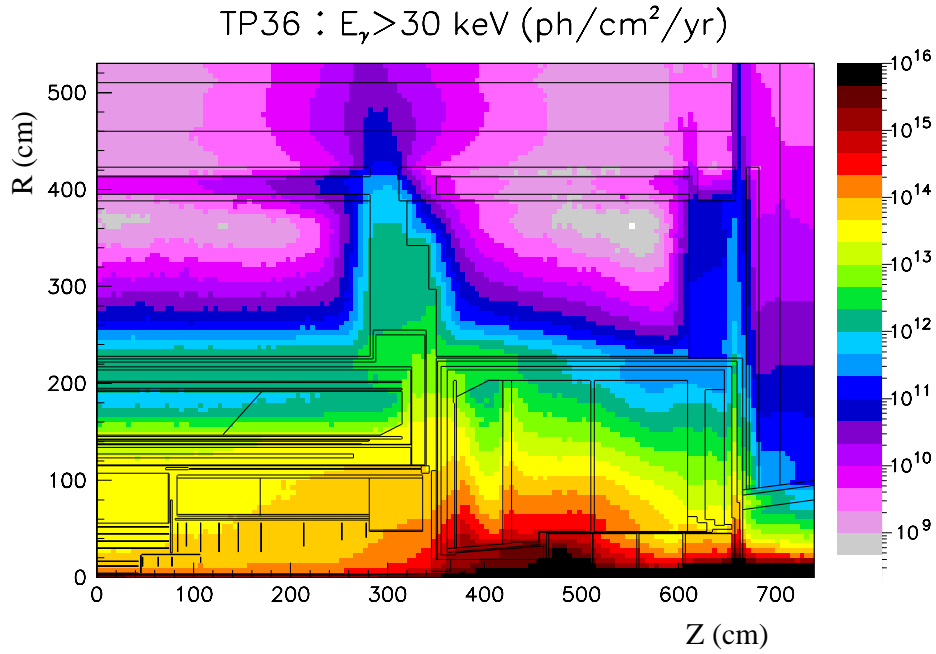


Figure 12.4: Calculated ATLAS photon fluence rate for estimating the 'streaming' contribution from the beam-pipe at $Z \approx 680$ cm [Fer00].

Considering all these effects reduces the calculated ATLAS rate of photons, directly emerging from the calorimeter, to

$$\gamma\text{-fluence-rate}_{ATLAS} = 4\text{-}8 \text{ kHz/cm}^2, \quad (12.3)$$

which is compared to the

$$\gamma\text{-fluence-rate}_{H6} = 7.3 \text{ kHz/cm}^2 \quad (12.4)$$

obtained with the simple H6 model.

Conclusion and Outlook

Background benchmarking measurements were performed in order to check the low energy streaming processes, which contribute via (n,γ) reactions to the radiation background in the LHC experiments. These processes were never checked before and therefore a large uncertainty of a factor 2.5 was attached to the Monte Carlo estimates.

For the experimental benchmark we used a mixed pion, proton and kaon beam at the relevant momenta of $p_{beam} = 40 \text{ GeV}/c$ and $p_{beam} = 120 \text{ GeV}/c$ hitting an iron absorber with a thickness of 11 to 14 absorption lengths λ . This experimental arrangement approaches rather closely the situation in the forward part (rapidity $\eta > 2$) of the ATLAS experiment. Behind the absorber the absolute yield and energy of the particles, mainly photons and neutrons, emanating from the final stages of the shower processes in the absorber was measured with a $\text{Bi}_4\text{Ge}_3\text{O}_{12}$ detector (BGO).

In the course of this work the following results have been obtained:

- BGO response calibration measurements and simulations with well known radioactive sources were performed in order to give a first order benchmark.

The response measurements of three different γ -sources (^{137}Cs , ^{54}Mn , ^{60}Co) show both in terms of rates and spectra excellent agreement with the simulations on the 2% level. The efficiency for ^{137}Cs is $\epsilon_\gamma = 72\%$ for $E > 400 \text{ keV}$.

Neutron response measurements with an ^{241}Am -Be-source show that the neutron efficiency is $\epsilon_n = 15.4\%$ for $0.4 < E < 6.5 \text{ MeV}$. The comparison with the simulations shows that the neutron rates agree within 30%.

- For the benchmarking measurements we carried out measurements with different beam intensities (\approx factor 2-3) and beam momenta ($p_{beam} = 40 \text{ GeV}/c$ and $p_{beam} = 120 \text{ GeV}/c$), different trigger conditions, different measurement positions (*on beam-axis* and *off beam-axis*) and absorber thicknesses (11λ and 14λ).

These studies show that the particle fluences at the *on beam-axis* and *off beam-axis* measurements are very different. *On beam-axis* particles are dominated by shower processes close to the BGO resulting in a high multi-event rate. *Off beam-axis* data in contrast are single term neutral particles, dominated by photons produced via (n,γ) and $(n,n'\gamma)$ interactions.

We find that the measured particle rates, normalised to the incident beam particles agree at a 1σ level for the different intensity runs. We therefore conclude that the effects from residual activities, dead-time corrections and other experimental effects are well understood.

For the different measurements the uncertainties to the signal rates are within 6% and are dominated by the beam counter dead-time correction.

- A detailed simulation of the experimental set-up was performed.

The comparison with the measurements shows that the normalised total signal rates agree at a 20 % level (see Table 12.1). The weighted average yields a ratio between the measured and simulated total signal rates normalised to the incident beam particles of

$$\frac{\text{signal rate}|_{meas}}{\text{signal rate}|_{sim}} = 1.13 \pm 0.06. \quad (12.5)$$

The comparison between the spectra shows that the average energy depositions agree to better than 10 %. Furthermore, good agreement is found for the spectral shapes. This indicates that the complicated particle situations *on beam-axis* and *off beam-axis* are well understood.

The measured photon rates and spectra were evaluated by subtracting the simulated neutron and multi-event contributions from the total measured results. The induced uncertainties are estimated with the information of the neutron response calibration measurements. The measured and simulated photon rates agree very well. The weighted average gives a ratio of 1.25 ± 0.10 . Also the average energy depositions in the spectra agree extremely well.

Table 12.1: Summary of measured and simulated total signal rates normalised to the incident beam particles and the averaged energy depositions in the energy interval $0.35 \text{ MeV} < E < 9 \text{ MeV}$.

measurement set-up	signal rate $\times 10^{-4}$		$\langle E\text{-deposition} \rangle$ [MeV]	
	measured	simulated	measured	simulated
$p_{beam} = 40 \text{ GeV}/c$				
200 cm <i>on beam-axis</i>	76.2 ± 0.4	$71.8^{+6.7}_{-14.9}$	2.045 ± 0.018	2.057 ± 0.174
200 cm <i>off beam-axis</i>	6.8 ± 0.2	$6.1^{+0.8}_{-0.7}$	1.615 ± 0.004	1.618 ± 0.041
240 cm <i>on beam-axis</i>	23.0 ± 0.4	$15.8^{+2.7}_{-3.6}$	1.923 ± 0.009	1.824 ± 0.073
240 cm <i>off beam-axis</i>	2.3 ± 0.1	$1.9^{+0.3}_{-0.2}$	1.666 ± 0.003	1.530 ± 0.021
$p_{beam} = 120 \text{ GeV}/c$				
200 cm <i>off beam-axis</i>	26.3 ± 0.4	$26.0^{+3.0}_{-2.9}$	1.572 ± 0.009	1.805 ± 0.091
240 cm <i>on beam-axis</i>	93.5 ± 1.7	$78.6^{+9.6}_{-11.1}$	2.051 ± 0.020	2.058 ± 0.183
240 cm <i>off beam-axis</i>	9.7 ± 0.6	$7.8^{+1.4}_{-1.3}$	1.649 ± 0.006	1.687 ± 0.051

- In a simple model a quantitative comparison between the ATLAS shielding set-up and the experimental set-up for the benchmarking measurements was established.

Summarising, up to now the contribution to the background uncertainties due to the limited knowledge of the shower processes in the absorber and of the (n,γ) cross-sections was estimated to be at the **2.5 level**.

This work has shown that the background benchmarking measurements in a set-up similar to the ATLAS shielding agree with the simulations within better than 20 %. We can hence reduce the uncertainty from the shower processes to a **1.2 level**.

Appendix A

A.1 Photon Detection with the BGO

A.1.1 Photon Interaction in Matter

When photons interact with matter, they are either completely absorbed (photo-electric effect, pair production) or scattered (Compton-effect) [Gru93]. In matter gamma-rays are attenuated exponentially with

$$I = I_0 e^{-\mu x} \quad (6)$$

with μ the attenuation coefficient.

μ includes the cross-sections for all interaction processes i :

$$\mu = \rho \frac{N_A}{A} \sum_i \sigma_i \quad (7)$$

where A is the atomic number of the medium and N_A Avogadro's number and ρ the density of the material.

Depending on the photon energy and the atomic number of the absorber different photon interactions dominate. Figure 5 shows these regions.

A.1.1.1 Photo-Electric Effect

Photo-electric absorption is an interaction in which the incident gamma-ray photon completely disappears. In its place, a photo-electron is produced from one of the electron shells of the absorber atom with a kinetic energy E_{e^-} given by the incident photon energy $h\nu$ minus the binding energy of the electron E_b in its original shell. The probability of absorption of the photon is highest for K-shell electrons due to their proximity to the nucleus. The vacancy that is created in the electron shell due to the ejection of the photo-electron is quickly filled by electron rearrangement [Kno79]. In this process, the binding energy is liberated either in form of a characteristic X-ray or an Auger-electron. While the Auger-electron travels only a short distance due to its low energy, the X-ray can have quite a long range before being re-absorbed again through photo-electric interactions. The escape

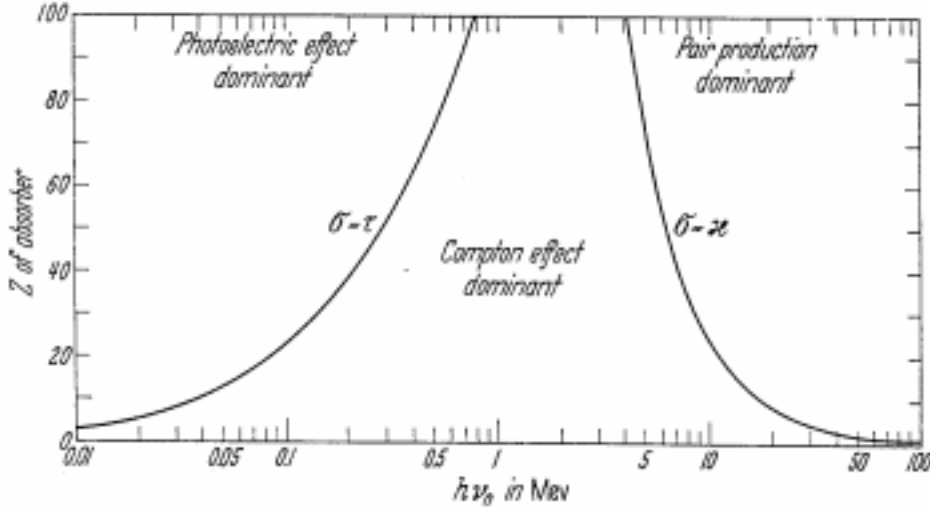


Figure 5: Regions where the photo-effect, Compton-effect and pair production dominate.

of these X-rays can be significant. However, if nothing escapes from the detector, the sum of the kinetic energies of the electrons that are created correspond to the original energy of the gamma-ray photon.

Therefore the photo-electric effect is an ideal process for measuring the energy of the original gamma-ray.

The cross-section in the non-relativistic range for the photo-electric effect is

$$\sigma_{photo}^K = \sqrt{32} \left(\frac{m_e c^2}{E_\gamma} \right)^{7/2} \alpha^4 Z^5 \sigma_{Th}^e \quad [\text{cm}^2/\text{atom}], \quad (8)$$

where $\sigma_{Th}^e = \frac{8}{3} \pi r_e^2 = 6.65 \cdot 10^{-25} \text{cm}^2$ is the Thomson cross-section for the elastic scattering of photons with electrons [Gru93]. For high energies ($E_\gamma/m_e c^2 \gg 1$) the cross-section becomes

$$\sigma_{photo}^K = 4\pi r_e^2 Z^5 \alpha^4 \frac{m_e c^2}{E_\gamma}. \quad (9)$$

A.1.1.2 Compton-Effect

The result of the Compton-effect is the creation of a recoil electron and the scattered gamma-ray photon. The energy of the scattered gamma-ray $h\nu'$ is given by

$$h\nu' = \frac{h\nu}{1 + \epsilon(1 - \cos \theta)} \quad (10)$$

with $\epsilon = h\nu/m_e c^2$ and θ the scattering angle. The kinetic energy of the recoil electron is hence

$$E_{e^-} = h\nu - h\nu' = h\nu \left[\frac{\epsilon(1 - \cos \theta)}{1 + \epsilon(1 - \cos \theta)} \right]. \quad (11)$$

When $\theta \approx 0$ we get $h\nu \approx h\nu'$ and thus $E_{e^-} \approx 0$. In this situation the recoil Compton-electron has very little energy and the energy of the scattered gamma-ray corresponds nearly to the energy of the incident photon. There is another extreme when $\theta = \pi$; The incident gamma-ray is backscattered towards its direction of origin and the electron recoils along the direction of incidence. In this situation the Compton-electron gets most of the energy transferred.

Normally all scattering angles will occur in the detector. Hence a continuum of energies can be transferred to the electron, ranging from zero up to the maximum energy

$$E_{e^-} |_{\theta=\pi} = h\nu \left[\frac{2\epsilon}{1 + 2\epsilon} \right] \quad (12)$$

which results in the so called Compton edge.

The total cross-section for scattering photons with electrons is

$$\sigma_c^e = 2\pi r_e^2 \left[\left(\frac{1 + \epsilon}{\epsilon^2} \right) \left\{ \frac{2(1 + \epsilon)}{1 + 2\epsilon} - \frac{1}{\epsilon} \ln(1 + 2\epsilon) \right\} + \frac{1}{2\epsilon} \ln(1 + 2\epsilon) - \frac{1 + 3\epsilon}{(1 + 2\epsilon)^2} \right] \quad [\text{cm}^2/\text{e}^-]. \quad (13)$$

For high energies the compton cross-section becomes

$$\sigma_c^e \sim \frac{\ln \epsilon}{\epsilon}. \quad (14)$$

The compton cross-section for photons with an atom with Z electrons is then

$$\sigma_c^{\text{atomic}} = Z \cdot \sigma_c^e. \quad (15)$$

A.1.1.3 Pair Production

The pair production process corresponds to the creation of an electron-positron pair in the field of a nucleus of the absorbing material provided that the photon-energy is higher than $2m_0c^2$ to make the process energetically possible. If the incident photon exceeds this value, the excess energy appears in form of kinetic energy shared by the electron-positron pair. We hence have

$$E_{e^-} + E_{e^+} = h\nu - 2m_0c^2. \quad (16)$$

For typical energies both the electron and positron travel a few millimetre at most before losing all their kinetic energy to the absorbing medium. Once the kinetic energy of the positron becomes very low, the positron will annihilate into two photons of energy m_0c^2 each. If one of these photons escapes the detector, in total the energy $h\nu - m_0c^2$ will be deposited corresponding to the so called *single escape peak*. If both photons escape the detector, the total energy will be $h\nu - 2m_0c^2$ matching the so called *double escape peak*.

When the nucleus is completely shielded by the electrons ($\epsilon \gg \frac{1}{Z^{1/3}}$), the pair-production cross-section is

$$\sigma_{pair} = 4\alpha r_e^2 Z^2 \left[\frac{7}{9} \ln \frac{183}{Z^{1/3}} - \frac{1}{54} \right] \quad [\text{cm}^2/\text{atom}]. \quad (17)$$

A.1.2 Predicted Response Function for Photon Detectors

Whereas the charged particle energy (photo-electron, Compton-electron, pair-electron and positron) is completely absorbed in the detector volume, the mean free path of the secondary gamma radiations produced in interactions of the original gamma-ray is of the order of several centimetres. Hence the response function depends beside the shape and composition of the detector also on the detector size.

If the detector is large enough, all secondary radiations, including Compton scattered gamma rays and annihilation photons also interact within the detector volume and none escapes from the surface. These conditions translate into detector dimensions on the order of many tens of centimetres [Kno79]. The detector response is then the same as if the original gamma-ray photon had undergone a simple photo-electric absorption in a single step.

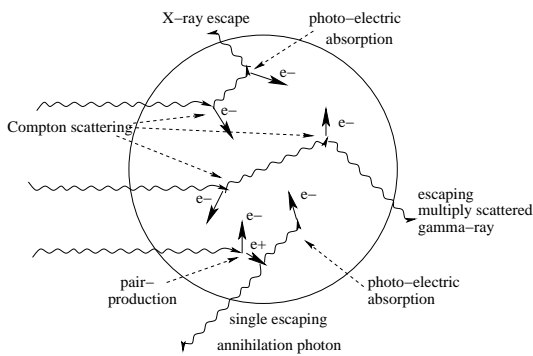


Figure 6: Representative histories of photon interactions in the detector.

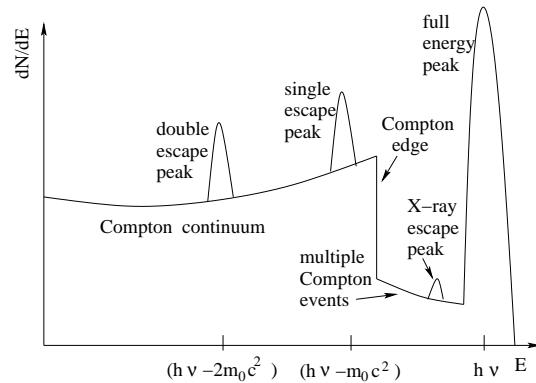


Figure 7: Photon interaction signatures in the spectrum of a detector of intermediate size.

The used BGO detector is not large enough to fulfil these requirements. Hence we do not have only the full-energy peak in the spectral distribution of the detector but in addition we find several photon interaction signatures. Figure 6 shows some representative histories. In Figure 7 a typical spectrum is illustrated. Beside the continuum from single Compton scattering there is also the influence of multiple Compton events followed by photon escape. The full-energy peak also contains some histories that began with Compton scattering. The single (double) escape peak corresponds to initial pair production where one (two) annihilating photon(s) leaves the detector. At high gamma-ray energies, the single and double escape peaks are quite prominent parts of the response function (see e.g. ^{241}Am -Be spectrum in Figure 5.13).

The X-ray escape peak originates from a photo-electric absorption of the incident gamma-ray, where the binding energy due to the electron rearrangement is liberated in form of X-rays that escape the detector. The materials that surround the detector are also potential sources of secondary radiations that can be produced by interactions of the primary photon emitted by the source. Figure 8 shows a sketch of the possible interactions. If the secondary radiations reach the detector, they can influence the shape of the spectrum. Figure 9 shows these features in the response function.

The peak at 511 keV originates from a pair-production in the BGO surrounding with a following annihilation into two γ 's where one enters the BGO detector. In all H6 spectra this peak is very strong.

The X-ray escape peak comes from a characteristic X-ray due to photo-electric absorption in the surrounding material.

The backscatter peak at around ≈ 0.25 MeV is caused by gamma-rays from the source that have first interacted by Compton scattering in the surrounding material. The energy of the backscatter peak corresponds to the energy in equation (10) with $\theta = \pi$. For high incident photon energies this energy is

$$h\nu' |_{\theta=\pi} \approx \frac{m_0c^2}{2} \approx 0.25 \text{ MeV}. \quad (18)$$

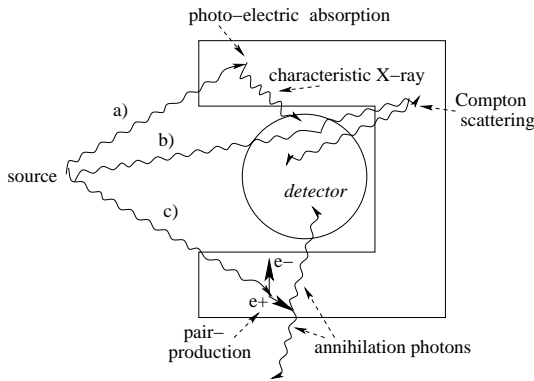


Figure 8: Influence of surrounding material to the detector response.

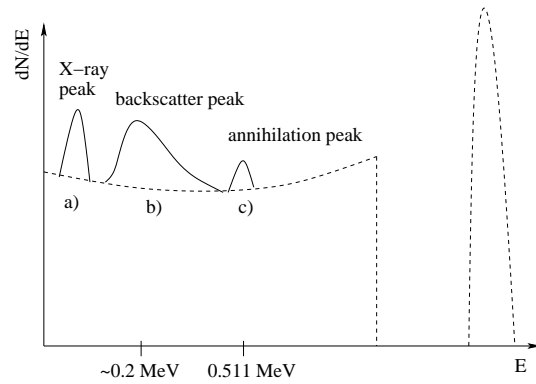


Figure 9: Additionally to the expected spectrum (dashed lines) the features due to the surrounding material are illustrated.

A.2 BGO Characteristics

Bismuth Germanate of the composition $\text{Bi}_4\text{Ge}_3\text{O}_{12}$ (BGO) is a high Z, high density scintillation material. Due to the high atomic number of bismuth ($Z=83$) and its high density of 7.13 g/cm^3 , BGO is a very efficient γ -ray absorber resulting in a very good photo peak to Compton ratio. Thanks to the high density, the material is used where high stopping power is required [Cri92].

The scintillation emission maximum of BGO is situated at 480 nm. The scintillation light can be detected with standard photo-multiplier tubes. The light yield (photons/MeV γ) is about 20-25 % of NaI(Tl) but since the emission is partly in the area above 500 nm where PM tubes are less sensitive, the relative photo-electron yield compared to NaI(Tl) amounts to 10-15 % [Sak87, Hol88].

The decay time of BGO is about 300 ns at room temperature, which is comparable to that of NaI(Tl). The afterglow is about 0.005 % after 3 ms.

The scintillation intensity of BGO is a strong function of the temperature. At room temperature, the gradient is approximately $1 \% \text{ K}^{-1}$ [Kes86, Zuc89].

BGO scintillation crystals are susceptible to radiation damage starting at radiation doses between 1 and 10 Gray. The effect is largely reversible. Since the radiation damage to BGO crystals depends on the presence of sub ppm impurities, large differences between individual crystals can occur.

BGO is a relatively hard, rugged, non-hygroscopic crystal which does not cleave. The material does not show any significant self absorption of the scintillation light. No hermetic air-tight sealing is required. BGO can be machined to various shapes and geometries. Table 2 gives a summary of the characteristics.

Table 2: *Characteristics of the BGO.*

Density [g/cm^3]	7.13
Melting point [K]	1323
Thermal expansion coefficient [K^{-1}]	$7 \cdot 10^{-6}$
Cleavage plane	none
Hardness (Mho)	no
Wavelength of emission maximum [nm]	480
Lower wavelength cutoff [nm]	320
Refractive index at emission maximum	2.15
Primary decay time [ns]	300
Afterglow (after 3 ms) [%]	0.005
Light yield [photons/MeV γ]	$8 \cdot 10 \cdot 10^3$
Photo-electron yield [% of NaI(Tl)] (for γ -rays)	15-20

A.3 FLUKA

FLUKA is a 3-dimensional Monte Carlo Particle transport program that simulates particle histories in a user defined surrounding. In these histories all particles shown in Table 3 can be produced and transported. Except for neutrinos, interactions with matter are simulated in all details.

In comparison to many other particle transport programs, FLUKA simulates the histories of the particles over a wide range of energy shown in Table 4.

Table 3: *Particles simulated in FLUKA.*

γ	$e^-, e^+, \nu_e, \bar{\nu}_e$ $\mu^-, \mu^+, \nu_\mu, \bar{\nu}_{mu}$ $\tau^-, \tau^+, \nu_\tau, \bar{\nu}_{tau}$
pos. hadrons	$p, \bar{\Sigma}^+, K^+, \Omega^+, \pi^+, \Sigma^+, \Xi^+$
neg. hadrons	$\bar{p}, \bar{\Sigma}^-, K^-, \Omega^-, \pi^-, \Sigma^-, \Xi^-$
neutral hadrons	$\bar{K}^0, \bar{\Sigma}^0, \bar{\Xi}^0, K^0, \pi^0, \Sigma^0, \Xi^0$ $n, \Lambda, \bar{\Lambda}, \bar{n}, K_L^0, K_S^0$

Table 4: *Particle dependent energy ranges used in FLUKA.*

	transport limits	limits for primary particles
charged hadrons	1 keV-20 TeV	100 keV-20 TeV
neutrons	thermal-20 TeV	thermal-20 TeV
anti-neutrons	50 MeV-20 TeV	100 MeV-20 TeV
muons	1 keV-1000 TeV	100 keV-1000 TeV
electrons (for high Z)	1 keV-1000 TeV	150 keV-1000 TeV
electrons (for low Z)	1 keV-1000 TeV	70 keV-1000 TeV
photons	1 keV-1000 TeV	7 keV-1000 TeV

The used geometry description in FLUKA is a kind of 'combinatorial geometry', which covers a specific number of three dimensional basic bodies. These bodies can be combined with boolean operators in order to set up more complicated constructions in so called 'regions'. The entire FLUKA geometry consists of a certain number of regions. To each region a material is assigned, which has to be defined by the user.

The particle transport simulation in FLUKA is similar to real life experiments. The path of the particles through the geometry is simulated according to the cross-sections, which are

submitted with the region material composition. In case of inelastic reactions or decays, new particles can be produced where the history of these particles is simulated as well. In general, the simulation of a particle ends if the particle either escapes from the simulated regions or if the energy is lower than a set threshold.

In order to 'measure' the conditions of the simulated particle histories, one has to define kind of detectors that yield quantities evaluated by the simulation procedure. The most important 'detectors' measure:

- particle fluences and currents
- induced track length of particle in defined volumes
- number of inelastic reactions in defined volumes
- amount of energy deposition in a specified volume (per primary particle or in average)
- produced residual nuclei
- production yield of produced particles.

Except for full simulations, FLUKA can be also run in a mode that increases the statistics in regions hardly reached by the particles. In this method regions are defined with different statistical importances. Particles entering these regions are then treated according to region importance. Using these biasing [Fas97] methods one can decrease significantly the necessary CPU time consumption of the simulations.

Appendix B

Glossary

Uncertainty vs. Error

According to the *Guide to the Expression of Uncertainties in Measurements (GUM)*, ISO, Geneva, 1995, one has to distinguish between the terms **uncertainty** and **error**:

- **Uncertainty**

The uncertainty of a measurement is a parameter, associated with the results of a measurement, that characterises the dispersion of the values that could reasonably be attributed to the measurand².

It is understood that the result of the measurement is the best estimate of the value of the measurand, and that all components of uncertainty, including those arising from systematic effects, such as components associated with corrections and reference standards, contribute to the dispersion.

- **Error**

The error is the result of a measurement minus a true value of the measurand.

Note: The true value can not be determined.

Due to these definitions the term **error** is not used in this thesis but instead we use the term **uncertainty**.

²Measurand is a particular quantity subject to measurement.

Fluence vs. Current

Results about radiation fields are normally presented using two quantities, **fluence** and **current**[Fer95]. The distinction between the two is the following:

- **Fluence**

dN/dA_{perp} : The number of particles crossing a surface element divided by the projection of that element perpendicular to the particle direction.

Hence fluence does not depend on the specific surface element used for the 'measurement', but it is only a function of the radiation field at the given point. All physical effects of the radiation field, energy deposition (dose), interaction rate, activation, damage, etc. are all proportional to the fluence.

- **Current**

dN/dA : The number of particles crossing a given surface element, divided by that element irrespective of the mutual orientation of the normal to the surface and the particle direction.

Current is the quantity of interest every time one would like just to 'count' the number of particles through a specific surface, regardless of the physical effects they will induce. (However, this quantity has no 'official' name issued by ICRU.)

When we talk of the term 'fluence' in this thesis we mean the fluence behind the absorber normalised to the incident beam particle. Only in chapter 12 the terms are exactly defined where 'fluence rate' is the fluence per second and 'fluence/particle' is the fluence behind the absorber per incident particle.

Acknowledgements

First of all I want to thank Chris Fabjan who contributed most to my scientific development. He accompanied and guided me in the last 4 years with continuous support and immense competence. I really appreciate his enthusiasm, power and drive. I am also very thankful for his many efforts to make students comfortable in his group like, in my case, organising offices, cars, skiing trips and ball-tickets.

Special thanks go to Thomas Otto from whom I learned most things that I know about radiation issues. He showed a lot of interest in our project, he always found time for discussions and often helped out with advice and practical support.

It was a real pleasure to work so closely with Helmut Vincke who did the FLUKA simulations. Since he did the counterpart to my work I am really grateful that his straightforward and unconventional character made it so easy for me to collaborate without any problems. Special thanks also for proof-reading this thesis even in the fitness-centre.

I had a very successful and interesting time during the test-beam periods thanks to the contribution of many people. I am very thankful to Sven Kircher for sharing with me the first test-beam period. The many discussions and the close team-work helped me a lot in the start-up phase. Many thanks go to Nigel Hessey for helping with all DAQ problems and for taking over a lot of shifts. I could always rely on Konrad Elsener for answering the many questions I had concerning the beam. I also had a good time with Angela Mitaroff and Luisa Ulrici in the test-beam (and certainly in Pisa). I am grateful to Heinz Vincke for taking over many shifts. I address many thanks to Julien Barbier who gave me a lot of support with hardware issues. Thanks go to Konrad Bussmann and Giovanni Di Tore for the help in all matters of engineering and electronics. I am very grateful to Jean Bourges, especially for bearing the noise of the DAQ set-up. Guy Roubaud was very helpful in all radioactive source issues.

I am very grateful to Martin Aleksa for sharing the daily ups and downs during the work. His positive attitude very often jumped over to me. From the time when Christoph Posch joined the same office, the level of goofing around increased dramatically ('richtig!'). I also profited very much of his excellent PC knowledge. Special thanks go to Vinnie Polychronakos for letting me use his computer in one of the nicest offices at CERN. Thanks also go to Frank Linde, Jörg Wotschack, Francois Rohrbach for their support and help.

There are many friends who contributed a lot to my well-being in Geneva. Special thanks go to Sophie and Martin who are always there for spending the time together after work. I really enjoyed the cosy evenings with them at their house. I also had a great time with Hemma. With her I could be sure that she would join the many adventures that were on my mind. I also shared a lot of exciting activities and experiences together with Sandra and Alex. I had a great time at hundreds of parties, barbecues, festivals and trips to Barcelona, Berlin etc. thanks to Uli, Adrian, Simi, Axl, Thomas, Karsten, Cathi, Michi, Ingrid, Marko, Bettina, Petra, Barbara, Peter and many others. Thanks go especially to Hansi and Susi in Austria. I very much enjoyed the short but great moments with each of them.

I am grateful to the Austrian Ministry for Science for the financial support, which made my stay at CERN possible.

My biggest gratitude belongs to my family. I received steady encouragement from my parents and they always supported me with unconditional confidence. I especially thank them for giving me a real home where I can always go to. I owe a lot to my brothers for always listening to me and keeping the balance of my priorities. I am also sure that my grandmother would be very proud of me. I am deeply indebted to Werner. Although he spent a lot of his time in Boston during my thesis work, he was always by my side. I thank him for all contributions to my life and especially for giving me the feeling that I can absolutely rely on him.

Bibliography

- [Ale99] M. Aleksa: *Performance of the ATLAS Muon Spectrometer*, PhD thesis, CERN (1999).
- [Ali95] ALICE Collaboration: *ALICE Technical Proposal*, CERN/LHCC/95-71 (1995).
- [Amb99] G. Ambrosini et al.: *Measurement of Charged Particle Production from 450 GeV/c Protons on Beryllium*, submitted to the European Physical Journal C, CERN-EP/99-19, CERN (1999).
- [Atb97] ATLAS Collaboration: *ATLAS Barrel Toroid Technical Design Report*, CERN/LHCC/97-19 (1997).
- [Atc96] ATLAS Collaboration: *ATLAS Calorimeter Performance Technical Design Reports*, CERN/LHCC 96-40 (1996).
- [Atc97] ATLAS Collaboration: *ATLAS Central Solenoid Technical Design Report*, CERN/LHCC/97-21 (1997).
- [Ate97] ATLAS Collaboration: *ATLAS End-Cap Toroids Technical Design Report*, CERN/LHCC/97-20 (1997).
- [Ati97] ATLAS Collaboration: *ATLAS Inner Detector Technical Design Report*, CERN/LHCC 97-16 and 97-17 (1997).
- [Atl94] ATLAS Collaboration: *ATLAS Technical Proposal*, CERN/LHCC/94-43 (1994).
- [Atl96] ATLAS Liquid Argon Collaboration: *ATLAS Liquid Argon Calorimeter Technical Design Report*, CERN/LHCC/96-41 (1996).
- [Atm97a] ATLAS Collaboration: *ATLAS Muon Spectrometer Technical Design Report*, CERN/LHCC 97-22 (1997), available on the WWW-page:
<http://atlasinfo.cern.ch/Atlas/GROUPS/MUON/TDR/Web/TDR.html>
- [Atm97b] ATLAS Collaboration: *ATLAS Magnet System Technical Design Report*, CERN/LHCC/97-18 (1997).
- [Atp98] ATLAS Collaboration: *ATLAS Pixel Detector Technical Design Report*, CERN/LHCC/98-13 (1998).

- [Atp99] ATLAS Collaboration: *ATLAS Detector and Physics Performance Technical Design Report*, CERN/LHCC 99-14 and 99-15 (1999).
- [Att96] ATLAS Collaboration: *ATLAS Tile Calorimeter Technical Design Report*, CERN/LHCC/96-42 (1996).
- [Bar94] S.A. Baranov et al.: *Gamma Sensitivities of Pressurised Drift Tubes*, ATLAS Internal Note MUON-NO-36, CERN (1994).
- [Bat94a] G. Battistoni et al.: *Background Calculations for the ATLAS Detector and Hall*, ATLAS Internal Note GEN-NO-010, CERN (1994).
- [Bat94b] G. Battistoni et al.: *Muon Chamber Sensitivity to Neutron and Photon Background in the ATLAS Hall*, ATLAS Internal Note MUON-NO-52, CERN (1994).
- [Bir98] C. Birrati et al.: *Recent Results at the CERN-EC High Energy Reference Field Facility.*, in Proceedings of the Third Specialist Meeting on Shielding Aspects of Accelerators, Targets and Irradiation Facilities (SATIF-3) at Tohoku University, Sendai, Japan, ed. by OECD, 1998, 219-234 (1998).
- [Che93] G.A. Chelkov et al.: *Investigation of Spectral Efficiency of Pressurised Drift Tubes for Detection of Neutrons in the Energy Range between 5 eV and 200 keV*, ATLAS Internal Note MUON-NO-31, CERN (1993).
- [Chu70] K.C. Chung et al.: Phys. Rev. **C2** 139 (1970).
- [Cms94] CMS Collaboration: *CMS Technical Proposal*, CERN/LHCC/94-38 (1994).
- [Cri92] Crismatec: *Scintillator Detectors*, catalogue, The Netherlands (1992).
- [Den90] D. Denegri: *Standard Model Physics at the LHC (pp Collisions)*, published in [Jar90], Vol.I, 56-117 (1990).
- [Den94] A.S. Denisov et al.: *Differential Sensitivity of Cathode Strip Chambers to Neutrons and Photons*, ATLAS Internal Note MUON-NO-33, CERN (1994).
- [Eer92] P. Eerola: *Measurement of CP-Violation in B-Decays with the ATLAS Experiment*, ATLAS Internal Note PHYS-NO-009 (1992).
- [EGG95] EG&G Berthold: Rem-counter LB 6411 Operational Manual, Wildbad (1995).
- [Fas97] A. Fasso et al.: *New Developments in FLUKA Modelling Hadronic and EM Interactions*, Proc. 3rd Workshop on Simulating Accelerator Radiation Environments, KEK, Tsukuba, Japan 7-9 May 1997, Ed. H. Hirayama, KEK Proceedings 97-5, 32-43 (1997).
- [Fas99] A. Fasso et al.: *FLUKA 99: Particle Transport Code*, version 1999, write-up, <http://b.home.cern.ch/b/bnv/www/fluka> (1999).
- [Fer95] A. Ferrari, P. Sala: *Background Rates in the Muon System: Recent Results and the Effect of the Tungsten Plug*, ATLAS Internal Note MUON-NO-90, CERN (1995).

- [Fer97] A. Ferrari, P. Sala: *Shielding Modifications and their Influence on the Background Values*, ATLAS Muon Internal Note MUON-NO-162, CERN (1997).
- [Fer00] A. Ferrari: Private Communication (2000).
- [Gru93] C. Grupen: *Teilchendetektoren*, BI-Wiss.-Verl., Germany (1993).
- [Gsc97] E. Gschwendtner: *X-Ray Tomography for High-Precision Particle Detectors*, Diploma thesis, CERN (1997).
- [Gsc98] E. Gschwendtner et al.: *High-Precision X-Ray Tomograph for Quality Control of the ATLAS Muon Monitored Drift Tubes*, Nucl. Instrum. Methods **A419** 342-350 (1998).
- [Gsc00a] E. Gschwendtner, A. Mitaroff, T. Otto: *Performance Tests of the CERF Beam Monitor*, TIS-RP/TM/2000-07, CERN (2000).
- [Gsc00b] E. Gschwendtner, A. Mitaroff, L. Ulrici: *A New Calibration of the PIC Monitor in H6*, TIS-RP/IR/2000-09, CERN (2000).
- [Gsc00c] E. Gschwendtner, H. Vincke et al.: *Measuring the Photon Background in the LHC-Experimental Environment*, Proceedings of the International Workshop on Neutron Field Spectrometry in Science, Technology and Radiation Protection, submitted to NIM, Pisa, Italy (2000).
- [Hae83] O. Haeusser et al.: *The Prompt Response of Bismuth Germanate and NaI(Tl) Scintillation Detectors to Fast Neutrons*, Nucl. Instrum. Methods **213** 301-309 (1983).
- [Hig64] P.W. Higgs: *Broken Symmetries, Massless Particles and Gauge Fields*, Phys. Lett. **12**, 132-133 (1964).
- [Hol88] I. Holl, E. Lorenz, G. Mageras: IEEE Trans. Nucl. Sci. Vol.35, No 1, 380 (1988).
- [Int00] International Organization for Standardization, ISO 8529-1: *Reference Neutron Radiation Part 1: Characteristics and Methods of Production*, Geneva (2000).
- [Jar90] G. Jarlskog and D. Rein (editors): *Proceeding of the Large Hadron Collider Workshop*, CERN/90-10 (1990).
- [Kes86] M. Kesselberg: Nucl. Instrum. Methods **A243** 578 (1986).
- [Kin84] K.J. King, T.L. Johnson: *A High Energy Gamma Ray Calibration Source*, Nucl. Instrum. Methods, **227** 257-258 (1984).
- [Kno79] F.G. Knoll: *Radiation Detection and Measurement*, John Wiley&Sons, New York, USA (1979).
- [Leo87] W.R. Leo: *Techniques for Nuclear and Particle Physics Experiments*, Springer-Verlag, Germany (1987).
- [Lep00] LEPC meeting, August 2000, CERN (2000).

- [Lhc98] LHCb Collaboration: *LHCb Technical Proposal*, CERN/LHCC 98-4 (1998).
- [Loh85] W. Lohmann, R. Kopp, R. Voss: *Energy Loss of Muons in the Range 1-10000 GeV*, CERN-EP/85-03, CERN (1985).
- [Ott98] T. Otto: *Application of International Standard 10647 to CERN's Neutron Calibration Field*, TIS-RP/TM/98-19, CERN (1998).
- [Sak87] E. Sakai: IEEE Trans. Nucl. Sci. Vol. NS-34, No.1, 418 (1987).
- [Spe97] M. Spiegel: *On the Lifetime of Proportional Counters*, PhD thesis, CERN (1997).
- [Rie97] W. Riegler: *Limits to Drift Chamber Resolution*, PhD thesis, CERN (1997).
- [Vie96] G. Viehhauser: *Detector Physics of the ATLAS Precision Muon Chambers*, PhD thesis, CERN (1996).
- [Vin99] H. Vincke, E. Gschwendtner, C.W. Fabjan, T. Otto: *Simulation des Teilchenuntergrundes für LHC Experimente*, Österreichische Physikalische Gesellschaft, Fachauschusstagung für Kern- und Teilchenphysik, Ischgl, Austria (1999).
- [Vin00a] H. Vincke, E. Gschwendtner et al.: *Benchmarking of the Simulation of the ATLAS Hall Background*, Proceedings of the International Workshop on Particle Transport Simulation, submitted to NIM, Paris, France (2000).
- [Vin00b] H. Vincke: *Benchmarking of the ATLAS Hall Background Simulation*, PhD thesis, CERN (2000).
- [Vin00c] H. Vincke: *FLUKACAD/PIPSICAD: 3-Dimensional Interfaces between FLUKA and AUTOCAD*, Proceedings of the International Workshop on Particle Transport Simulation, submitted to NIM, Paris, France (2000).
- [Zuc89] A. Zucciatti et al.: Nucl. Instrum. Methods **A281** 341(1989).

Curriculum Vitae

- Name: Edda Gschwendtner
 Date of Birth: 02.02.1972, Salzburg
 Nationality: Austria
- 02/98 – 10/00 Ph.D. Thesis in Physics,
 Doctoral Thesis: *Benchmarking the Particle Background in the LHC Experiments* within the Austrian Doctoral Student Program at CERN, CERN and Vienna University of Technology (Technische Universität Wien).
- 10/91 – 10/97 Dipl. Ing. (M.S.) Degree in Physics at the Vienna University of Technology with highest honours (22.10.1997).
 Diploma Thesis: *X-Ray Tomography for High-Precision Particle Detectors* within the Technical Student Program at CERN and the Kurt-Goedel scholarship for computer sciences, Vienna (Kurt-Gödel-Auslandsstipendium für Computerwissenschaften).
- 09/82 – 06/90 High School (Bundesgymnasium Tamsweg), all certificates with distinction, emphasis on physics and mathematics.
 language education: English (8 years), Latin (6 years).
- summer 1995 Summer Student at CERN.
- 10/94 – 01/96 Teaching Assistant (Vienna University of Technology) for undergraduate students for the courses 'Mathematical Methods in Theoretical Physics' and 'Quantum Theory'.
- 1997 – present Several French courses at CERN.
- summer 1994 Spanish course in Malaga, Spain, with the aid of a scholarship from the 'Austrian Ministry for Science' for learning foreign languages.

List of Publications

1. E. Gschwendtner, H. Vincke, C.W. Fabjan, N. Hessey, T. Otto.: *Measuring the Photon Background in the LHC-Experimental Environment*, Proceedings of the International Workshop on Neutron Field Spectrometry in Science, Technology and Radiation Protection, submitted to NIM, Pisa, Italy (2000).
2. H. Vincke, E. Gschwendtner, C.W. Fabjan, T. Otto: *Benchmarking of the Simulation of the ATLAS Hall Background*, Proceedings of the International Workshop on Particle Transport Simulation, submitted to NIM, Paris, France (2000).
3. E. Gschwendtner, A. Mitaroff, L. Ulrici: *A New Calibration of the PIC Monitor in H6*, TIS-RP/IR/2000-09, CERN (2000).
4. E. Gschwendtner, A. Mitaroff, T. Otto: *Performance Tests of the CERF Beam Monitor*, TIS-RP/TM/2000-07, CERN (2000).
5. E. Gschwendtner et al.: *High-Precision X-Ray Tomograph for Quality Control of the ATLAS Muon Monitored Drift Tubes*, Nucl. Instrum. Methods **A 419** 342-350 (1998).
6. E. Gschwendtner: *X-Ray Tomography for High-Precision Particle Detectors*, Diploma thesis, CERN (1997).
7. E. Gschwendtner, F. Rohrbach, Y. Sedykh: *Analysis of the X-Tomograph Scan Data for MDT Chamber Prototypes*, ATLAS Internal Note MUON-NO-175, CERN (1998).
8. D. Drakoulakos, E. Gschwendtner, J.M. Maugain, F. Rohrbach, Y. Sedykh: *The High-Precision X-Ray Tomograph for Quality Control of the ATLAS MDT Muon Spectrometer*, CERN-OPEN-97-023, CERN (1997).
9. J. Berbier et al.: *X-Ray Tomograph Prototype for MDT Quality Control*, ATLAS Internal Note MUON-NO-174, CERN (1997).

I only quoted those publications to which I made a major contribution.

Lebenslauf

- Name: Edda Gschwendtner
Geburtstag: 02.02.1972, Salzburg
Nationalität: Österreich
- 02/98 – 10/00 Dissertation in Physik,
Doktorarbeit: *Bestimmung des Teilchenuntergrundes in LHC Experimenten* (verfasst in englischer Sprache) im Rahmen des Österreichischen Doktorandenprogrammes am CERN, CERN und Technische Universität Wien.
- 10/91 – 10/97 Dipl. Ing. der Technischen Physik an der Technischen Universität Wien mit Auszeichnung (22.10.1997).
Diplomarbeit: *Ein Röntgentomograph für Hochpräzisionsteilchendetektoren* (verfasst in englischer Sprache) im Rahmen des Technischen Studentenprogrammes am CERN und des Kurt-Gödel-Auslandsstipendiums für Computerwissenschaften, Wien.
- 09/82 – 06/90 Bundesgymnasium Tamsweg, alle Zeugnisse mit Auszeichnung,
Schwerpunkt Physik und Mathematik.
Sprachen: Englisch (8 Jahre), Latein (6 Jahre).
- Sommer 1995 Sommerstudentin am CERN.
- 10/94 – 01/96 Tutorin an der Technischen Universität Wien für “Mathematische Methoden der Theoretischen Physik” und “Quantenmechanik”.
- 1997 – jetzt Französischkurse am CERN.
- Sommer 1994 Spanischkurs in Malaga, Spanien, mit Unterstützung eines Stipendiums des Österreichischen Wissenschaftsministeriums.

Wenn ich groß bin, male ich
die ganze Welt, wasche ich
mich nie, wünsche mir eine Atom=
bombe, krieche ich den ganzen
Tag im Markt herum. Wenn ich
groß bin möchte ich auf
dem Mond.

Edla des. 1980